

# UC Berkeley

## UC Berkeley Electronic Theses and Dissertations

### Title

Biomolecular Plasmonics: Fundamentals and Applications

### Permalink

<https://escholarship.org/uc/item/27c2z2f1>

### Author

Hong, Soon Gweon

### Publication Date

2012

Peer reviewed|Thesis/dissertation

# **Biomolecular Plasmonics: Fundamentals and Applications**

By

Soon Gweon Hong

A dissertation submitted in partial satisfaction of the

Requirements for the degree of

Doctor of Philosophy

in

Engineering - Mechanical Engineering

in the

Graduate Division

of the

University of California, Berkeley

Committee in charge:

Professor Luke P. Lee, Co-chair

Professor Liwei Lin, Co-chair

Professor Dorian Liepmann

Professor Ming Wu

Spring 2012

Copyright 2012

By

SoonGweon Hong, Ph.D

Abstract

## **Biomolecular Plasmonics: Fundamentals and Applications**

by

Soon Gweon Hong

Doctor of Philosophy in Mechanical Engineering

University of California, Berkeley

Professor Luke P. Lee, Co-chair

Professor Liwei Lin, Co-chair

Decades of extensive research into metallic nanostructures have deepened our understanding of plasmonic phenomena. In turn, plasmonics have been utilized in various applications in a broad range of research fields. Plasmonic-aided biomolecular detection is highlighted due to its ability to obtain biomolecular fingerprint information in a non-invasive, in-situ, and single molecule resolution manner. However, its applicability to various fields still faces practical limitations such as reliable plasmonic structure fabrication, signal instability (or blinking), and signal variation amongst different plasmonic structures for the same molecule. In this respect, this thesis discusses the fundamentals of plasmonic phenomena and molecular interaction with excited plasmonic structures.

Here we demonstrate the designs of plasmonic structures: eagle-beak nanoantenna, gold nanoflake on photonic crystal, and gold viruses. The first two are for large-area uniform substrates that enable single-molecule sensitivity. The last one is a mobile nanoparticle that continuously interacts with a cellular system with multiple functions including molecular imaging, targeting, and drug delivery. We also suggest preconcentration-based non-blinking single-molecule detection. Electric and temperature fields were considered in moving molecules towards excited nanostructures. By using an eagle-beak nanoantenna, we demonstrate single-molecule, non-blinking surface-enhance Raman scattering. Furthermore, variation of molecular scattering from a curved Poynting vector and depolarized scattering from nonparallel electron motion to incident light are discussed as a new molecular detection scheme. Lastly, we provide a design concept that utilizes temperature and a thermal gradient to activate carrier molecules on nanoparticles, in particular for extrinsic gene delivery. By varying the thermal profile around plasmonic structures, diverse gene activation schemes are available for biological experiments.

When the electric and thermal fields around excited plasmonic structures are considered in terms of gradients and vectors, we can enhance detection capabilities while conferring multiple functionalities to structures. We believe this series of new approaches to plasmonic-aided molecular detection can elevate molecular imaging potential in real fields, and further expand to other types of applications such as plasmonic energy harvest, optical communication and biomedical applications.



*To my loving parents and family, without your support none of this would have been possible*

## Table of Contents

Table of Contents .....	ii
Lists of Figures .....	iv
Acknowledgements .....	xiii
Chapter 1 Introduction to Molecular Plasmonics.....	1
1.1 Fundamentals of Plasmonics .....	1
1.2 Physical Expression from Nanoplasmonics .....	2
1.3 Current Researches of Plasmonic Molecular Detection .....	4
1.4 Outline of Thesis .....	5
Chapter 2 Eagle-beak Nanoantenna for Nonblinking Single-Molecule SERS via Preconcentration .....	8
2.1 Introduction .....	8
2.2 Design Factors of ‘Eagle-beak’ .....	9
2.3 Function of ‘Eagle-beak’ .....	10
2.3.1 Local Field Amplification of <i>Eagle-beak</i> .....	10
2.3.2 Preconcentration around <i>Eagle-beak</i> .....	12
2.4 Fabrication of Nano Eagle-beak .....	14
2.5 Surface-enhanced Raman Scattering Measurement .....	15
2.5.1 Highly Enhanced Raman Signal via <i>Eagle-beak</i> .....	15
2.5.2 Temporal Stability of SERS via <i>Eagle-beak</i> .....	15
2.6 Conclusion .....	17
Chapter 3 Photothermal Physics for Optical Gene Regulation.....	19
3.1 Introduction .....	19
3.2 Advantages of Gold Nanoparticle based Gene Delivery .....	20
3.3 Photothermal Heat from an Excited Nanorod .....	21
3.4 Gene Activation by Photothermal Physics .....	23
3.5 Conclusion .....	27
Chapter 4 Depolarization of Plasmonic Scattering.....	30
4.1 Introduction .....	30
4.2 Molecular Spectrum Variation around Excited Plasmonics .....	32
4.2.1 Spatial Pattern of Molecular Scattering Spectrum .....	32
4.2.2 Plasmonic-induced Variation of Molecular Scattering Spectrum.....	33

4.2.3 Emitting Pattern Change around Nanoparticle .....	35
4.3 Confinement of Depolarized Scattering and its Applications .....	36
4.3.1 Depolarization Scattering from 2-dimensional Metallic Nanostructure .....	37
4.3.2 Suppressed Depolarized Scattering via Nanostructure Array .....	39
4.3.3 Localized Depolarized Scattering for Molecular Imaging .....	42
4.4 Conclusion .....	43
 Chapter 5 Tunable Sensitivity of Plasmonic Nanoflake on Photonic Crystal .....	45
5.1 Introduction .....	45
5.2 Design of Nanoflake on Photonic Crystal .....	47
5.3 Single-molecule Level Detection via Nanoflake .....	51
5.4 Conclusion .....	53
 Chapter 6 Gold eu-Virus for Molecular Imaging .....	56
6.1 Introduction .....	56
6.2 Viral capsid as plasmonic nanoparticles .....	58
6.3 Mathematical model of viral capsid and electromagnetic simulation .....	58
6.4 Demonstration of Gold virus .....	60
6.5 Far-field Characterization .....	61
6.6 Molecular Imaging via Gold virus: PRET & SERS .....	63
6.7 Conclusion .....	65
 Chapter 7 Conclusion .....	69
 Appendix .....	72

## List of Figures

**Figure 1.1.** A metallic nanostructure whose size is similar to or smaller than optical wavelength generates a group oscillation of free electron and consequently expresses two physical forms to a surrounding medium: electromagnetic scattering and heat dissipation. Also, the difference of electric and thermal conductivity in the interface of nanostructure causes strong gradient formation of electric and temperature around the nanostructure. .... 2

**Figure 1.2.** Outline of this thesis. Improved molecular detection schemes will be discussed by using various aspects of plasmonic expressions. In addition of strongly amplified optical field, the gradients of electric and thermal field will be studied for molecular preconcentration in the hot spots, and also depolarization induced by electron motion nonparallel to incident light will be studied for molecular detection by a polarization contrast or spectral variation. .... 5

**Table 1.1.** Physical expressions from excited plasmonic structures. In addition to optical field amplification, many interesting physical points are found from the physical expressions which can be useful for various applications as listed. .... 3

**Figure 2.1.** Schematic diagrams for highly enhanced stable SERS signal via eagle-beak nanoantenna. (A) The eagle-beak nanoantenna concentrates target molecules to the nearby volume around the nanoantenna during plasmonic excitation. More molecules concentrated around the SERS-enable volume generate higher and more stable SERS signal. (B) SEM images of fabricated eagle-beak nanoantenna structures which consist of a bent polymer pillar and asymmetric tapered gold layer. (C) A strong hot-spot is generated around the edge at the side wall and the tip. Electromagnetic energy ( ) harmonically propagates along the structure and is focused at the tip. (D) Asymmetric bent metal layer dissipates heat to surrounding media, making asymmetric thermal gradient. Thermal diffusion along thermal gradient concentrates molecules around the bottom of the eagle-beak with fluidic motion induced by thermal buoyant force. (E) The focused E-field decreases exponentially in the media, and its gradient amplitude can overcome the lower limits of possible particle size set by conventional optical trapping. Tip-based eagle-beak nanoantenna can trap nanometer-sized molecules to the strong hot-spot with this mechanism. .... 9

**Figure 2.2.** Optical response of eagle-beak nanoantenna. (A) Schematic diagram of electromagnetic (EM) power flow along the tapered metal layer. This power propagation results in the strongest hot-spot at the tip and weaker hot-spots along the two long edges. The geometric dimensions (the length: 550 nm, the diameter: 120 nm) were decided by fabrication constraints and tuning the plasmonic resonance to visible light (B) Simulated electric-field distribution around optically resonated eagle-beak nanoantenna. E-field enhancement reaches three orders of magnitude at the tip. (C) Simulated E-field intensity at the tip of the designed eagle-beak versus excitation wavelength. Bottom-to-top incidence (black line) focuses more EM power to the tip than top-to-bottom incidence (red line), both

have a polarization parallel to AA' line in (A). Perpendicular polarization doesn't form strong enhancement at the tip (blue line). (D & E) SEM images of fabricated eagle-beak nanoantenna. The scale bar in the image is 500 nm. Oblique deposition of gold on laser interference pillar substrate (annotated arrow) fabricated eagle-beak structure forms an asymmetric nanoantenna. In the top view e, parallel polarization ( $\parallel$ ) to the eagle-beak tip is shown as blue line, and perpendicular polarization in red. Due to the asymmetry, eagle-beak nanoantenna array has a strong polarizability in the optical response as shown in simulation results. (F) Measured extinction spectra on eagle-beak array by varying polarization angle of incident light. The contour map shows strong resonance of the array to parallel polarization incidence ( $\parallel$ ), while perpendicular polarization incidence ( $\perp$ ) doesn't generate clear resonance in the wavelength range. (G) Measured extinction spectra for parallel, perpendicular and random polarizations. The random polarization results in the exact average of the ones of parallel and perpendicular polarizations. .... 00

**Figure 2.3.** Proposed mechanism of preconcentration. (A) Schematic diagram of thermal diffusion based preconcentration. Thermal gradient generated by hot bent eagle-beak and cold substrate gathers target molecules nearby the eagle-beak. (B) Free convection flow around the eagle-beak. Convective flux of target molecules is  $1e-6$  m/sec around the top of eagle-beak. (C) Thermal diffusion caused by photothermal effect on the substrate. Its flux reaches -1 to -2 orders of magnitude for nanometer-sized molecule (DT:  $10^{-10}$ ~ $10^{-9}$  ( $m^2/sec/K$ )), which is much higher than convective flux. (D) Schematic diagram of plasmonic trapping. A defined volume has a positive trapping force where (Thermal diffusion force) < (Plasmonic trapping force). (E) Normalized flux comparison from thermal diffusion and plasmonic trapping. In the tip-based hot-spot, the electric-field gradient has potential to generate strong plasmonic trapping forces which overcome thermal diffusion. .... 11

**Figure 2.4.** Eagle-beak SERS response to polarized laser and high-sensitivity SERS results. (A) Experimental scheme of SERS polarizability. The used 785nm CW diode laser has inherent 10:1 polarization ratio. A Benzenethiol (BT) coated eagle-beak substrate was put on a rotation stage of an inverted microscope, and was rotated in XY plane. (B) Measured BT SERS spectra in the experiment described in (A). 1mW laser power and 1sec integration were used. Parallel polarization (defined in Fig. 2.2) generated the strongest SERS signal, while perpendicular one did not show a clear Raman spectrum. (C) Peak intensities at  $1584cm^{-1}$  in b agree well with a sinusoidal curve having  $180^\circ$  period. The results in b & c, along with the polarization-dependent optical response in Fig. 2.2, suggest that the fabricated eagle-beak substrate is well matched to the design and that hot-spots are located in the designed areas. (D) For a test of sensitivity or detection limit, methanol-based 1,2-Bis(4-pyridyl)ethylene (BPE) solution was measured on the eagle-beak substrate. 1mW laser power, 10sec integration, the optimal sample angle to the laser polarization were used. 1fM~10pM concentrations were prepared and measured. The SERS signals linearly increased according to the concentration. The detection limit of MeOH-BPE reached 1fM with a good signal-to-noise ratio. For a comparison, 0.5M MeOH-BPE were measured in the same conditions but without the eagle-beak substrate. (E) Analytically calculated SERS

enhancement factors by the definition shown in the plot. The average enhancement factor in femto-mol concentrations reaches to the factor of 14..... 13

**Figure 2.5.** Temporal stability of SERS signal. (A) Time-resolved spectra of 1fM MeOH-BPE. The same experimental conditions were used. Subsequent spectra show a continuous increase of SERS signal and stabilization in a few seconds upon 785nm laser excitation. (B) Repeatable signal increase/saturation of SERS signal by laser excitation. Repeating open and close laser shutter showed the same repeating of signal increase and saturation. The target molecule is considered to gather during the laser excitation and scatter after the excitation in the solution. (C) Experimental scheme for analyzing concentration distribution change by eagle-beak substrate excitation of 785nm laser. Two opposing 20x objectives were used to focus 785nm and 532nm lasers. Center to center distance of the laser spots was changed to 0, 28, and 110  $\mu\text{m}$  (three true color images taken through a CCD camera connected to bottom objective display three different laser locations). (D) Local concentration increase by 785nm laser excitation. Fluorescence signal excited by 532 nm laser (3-sec integration) was used to determine BPE concentration. Inset plot shows a BPE fluorescence spectrum. 785nm laser was shined for 10 sec and off before 532nm excitation. The intensity of fluorescence was attained by integrating the spectrum in 540 to 620nm. Three independent experiments on different spots on the substrate showed the repeatable increase of concentration at the 785nm laser focus spot. The area apart from the 785nm excitation did not show any increase of fluorescence intensity. .... 16

**Figure 3.1.** Scheme of molecular optogenetics and its relevant thermal profiles around excited nanorod. (A & B) internalized genes on nanorod is not activated before its detachment, but light excitation to nanorod release/activate genes to regulate gene expression. This method by light excitation attains on-demand activation with high spatial and temporal resolution. (C & D) the combination of temperature and thermal gradient makes various gene activation scenarios by critical conditions of melting temperature and molecular binding force to nanorod. .... 20

**Figure 3.2.** Thermal profiles of optically excited nanorod from multiphysics simulations. (A) A polarized incident light parallel to nanorod major axis can induce surface plasmon effectively and its resonant wavelength can be tunable depending on nanorod's aspect ratio. (B, C & D) Plasmonic excitation generates resistive heat inside nanorod, especially in the middle part, and makes a localized high temperature region near the nanorod, and therefore a big magnitude of thermal gradients. This result is from 20mW 785nm CW laser focused on a 5 $\mu\text{m}$  diameter spot. The nanorod dimension is (a,b)=(86nm, 25nm) which is commonly available for 780~785nm excitation. (E & F) Spatial and temporal profile of temperature and thermal gradient on the nanorod. .... 22

**Figure 3.3.** Modulation of thermal profiles from nanorod excitation. (A & B) Temperature and thermal gradient change linear to laser power. Temperature is superposed to ambient temperature with laser excitation but thermal gradient is not. For comparison, a

melting temperature of two-order base-pair dsDNA and required thermal gradient to match gold-thiol binding force are shown in plots. (C & D) The change of nanorod size even with the same amount resistive heat generation results in a variety of thermal profiles. Smaller size can make higher temperature and bigger gradient. 1x indicates a nanorod size of (86nm, 25nm). ..... 23

**Figure 3.4.** Equivalent thermo-circuit model and its analytical calculations. (A) By defining an effective radius of sphere for the nanorod, thermal response of temperature and its gradient can be simplified as an equivalent circuit and be calculated as shown eq. 5. The effective radius is an average of major and minor axis of nanorod. (B) Two conditions of  $T=T_m$  and  $\Delta T=\Delta T_{bind}$  can guide to find required size of nanorod and resistive heat. Here,  $T_m=80\text{ }^{\circ}\text{C}$  and  $\Delta T_{bind}=3\times 10^{10}\text{ }^{\circ}\text{C/m}$ . (C) For the scenarios shown in Fig. 1c, resistive heat and equivalent radius are summarized from the eq. 5 calculation. Here electrostatic binding force is assumed 4 order smaller than gold-thiol binding force..... 26

**Figure 4.1.** Angle-dependent molecular scattering and effects of plasmonic phenomenon. (A) Under a polarized excitation, molecular scattering can be various in terms of intensity and spectral profile along the angle of observation. (B) Angle-dependent spectral variation can be mimicked by the position of molecules regarding excited plasmonic structures. .... 31

**Figure 4.2.** Simulation of gold nanosphere for depolarized scattering. (A) A defined optical geometry and 50-nm gold nanosphere. (B) Electric-field spectr show similar magnitude of depolarized fields. (C) Dipole-like scattering of  $E_x$  and quadrupole-like scattering of  $E_y$  and  $E_z$  are observed around the resonated gold nanosphere. .... 33

**Figure 4.3.** Measurement of angle-dependent scattering and GNP-induced spectral variation (A) The experimental setup. By using two gratings, input and output wavelengths were characterized. (B & C) Angle-dependent scattering change. The blue line is a normal direction scattering, the red line is oblique angle scattering ( $70\sim 80^{\circ}$ ), and the black line is normalized oblique angle scattering to normal direction scattering. (D & E) GNP influence in molecular scattering. The blue line is without-GNP, the red line is with-GNP and the black is normalized with-GNP scattering to without-GNP. These measurements were normal excitation and normal detection..... 34

**Figure 4.4.** Scattering spatial pattern change near gold nanosphere. (A) A defined emitter scattering shows main scattering happens normal to dipole direction. (B) A single dipole-like emitter near to gold nanosphere change its scattering patterns with function of position. (C) Quadrupole-like positioning four emitters bring the scattering patterns to parallel to dipole direction. .... 35

**Figure 4.5.** Depolarized scattering from various nanostructures. (A) A random geometry can induce a large depolarization ratio; (B) while 2-dimensional symmetric nanodisk suppresses the depolarization scattering. (C) An array of nanodisk can only transfer the same polarization scattering to a far field by completely suppressing the depolarization scattering. (D) The physical reason of depolarization scattering is electron oscillation happens at a similar range to nanostructure dimension under optical field excitation. (E) In case of nanodisk array, the orthogonal electric field is confined around array plane like evanescent wave of total internal reflection. .... 37

**Figure 4.6.** Depolarized scattering from a single nanodisk. The studied nanodisk is 100-nm diameter and 20-nm thickness, and its material is supposed as gold. (A) A polarized electric field excitation causes dipole-like parallel electron motion and quadrupole-like orthogonal electron motion in the disk. Even with quadrupole-like oscillation, the distance between each pole cannot suppress depolarized scattering to far field completely. (B) Parallel electric field forms as dipole pattern around the nanodisk, while (C) orthogonal electric field forms as a quadrupole of  $\pi$ -phase shift between each pole. (D) Generated photothermal heat is calculated separately regarding parallel electron motion and orthogonal electron motion. (E)  $E_{\parallel}$  shows propagation like typical dipole scattering of plasmonic structure, while (F)  $E_{\perp}$  cannot be suppressed completely due to the distance between each pole of  $E_{\perp}$  quadrupole. (G) The field intensity of  $E_{\parallel}$  and  $E_{\perp}$  is compared by integration of each electric field over a 10 times bigger area along normal direction of nanodisk plane. The color maps of (B) and (C) are as linear, and one of (E) and (F) are plotted as log scale. .... 38

**Figure 4.7.** Depolarized scattering from a nanodisk array. (A) A schematic diagram shows how to complete suppression of  $E_{\perp}$  can be involved in an array form. (B) The calculated field intensity of  $E_{\perp}$  along a normal direction of plane, showing exponential decay like evanescent wave. The presented results in Fig. 5.3 are from a rectangular array of 100-nm diameter nanodisk and 400-nm periodicity, if not indicated further. (C) A color map of  $E_{\perp}$  about wavelength and z-axis distance. The wavelength spectrum of  $E_{\perp}$  is identical to  $E_{\parallel}$  around the nanodisk plane, but  $E_{\perp}$  propagates to far field by having the same decay constant along z axis (inset color map) independently to wavelength. (D) The decay profile is determined only by the periodicity of nanodisk array, and a linear relation exists between the periodicity and decay constant. The curves from left to right indicate the cases of 300, 400, 500, 600, 700, 800 nm periodicity, respectively. (E) A color map of  $E_{\perp}$  about wavelength and z-axis distance shows a dark scattering existence at the resonance excitation. (F) Induced electric field phase at the center of nanodisk. The  $\pi/2$  phase retardation can be related to the resonance of  $E_{\perp}$  and dark field scattering of  $E_{\parallel}$  ..... 40

**Figure 4.8.** Localized depolarization application for molecular imaging. (A) A polarized light input can generate a confined depolarized scattering around the nanodisk array. By



using two linear polarizers, the parallel polarization can be screened out, but only molecular scattering excited by depolarized field can be imaged. (B) and (C) are expected molecular imaging results by setting an analyzer parallel and cross to a polarizer. Images of (C) will be able to image molecules only nanoscale-distant from nanodisk array or furthermore calculate the distance of molecules from nanodisk array ..... 42

**Figure 5.1.** Design of nanoflake on photonic crystal. A combination of gold and AAO complex ( $\text{Al}_2\text{O}_3$  and aluminum) is useful to tune optical properties by changing the thickness of  $\text{Al}_2\text{O}_3$  and maintaining gold layer thickness. For enhanced optical hot-spot formation, a flake-like structure can be formed on the top of AAO complex, but the high dielectric property of AAO can maintain the overall optical properties (i.e., extinction) with the same thickness of smooth gold AAO. .... 47

**Figure 5.2.** Simulated optical property (or extinction) of gold-coated AAO. (A) Configuration of the simulation structure. The gold-AAO consists of 15-nm gold layer thickness, thick aluminum supports, and various thicknesses of alumina layer. The periodicity of AAO is fixed to 100 nm since an adopted electrochemical process determines the periodicity regardless of AAO thickness. (B to F) AAO and gold-coated AAO optical properties for various gold thicknesses as noted in plots. The original optical property of AAO is shown to strongly affect the optical properties of gold-AAO. .... 48

**Figure 5.3.** Comparison of smooth gold-AAO and nanoflake-AAO complex. (A & B) Scanning electron micrographs for the two cases of gold AAO. (C) The two cases of gold AAO shows identical optical extinction regardless of the gold layer morphology. Insets are naked-eye color taken by a general digital camera. (D & E) Simulation comparison for the two cases. Overall optical properties such as reflection and absorption show identical spectra, while strong optical hot-spots can be formed around nanogaps in the nanoflake layer. .... 49

**Figure 5.4.** Optical properties of a fabricated nanoflake set. (A) SEMs and naked-eye colors for various thicknesses of AAO. The same morphology of gold layer was formed regardless of thickness of AAO. The same thickness and morphology of gold layer and different thickness of AAO produce a dynamic color change over visible light. (B) Extinction spectra of the four nanoflake samples. The extinction was measured based on reflection due to AAO's opacity. (C) A plot for simulated 1st to 3rd peaks change along various thickness of AAO. The vertical dot lines indicate 65, 135, 195 and 275 nm, and crossed points from 1st, 2nd and 3rd peak accord with the measured extinction resonances. .... 51

**Figure 5.5.** SERS measurement on the four different nanoflake samples. (A & B) high-resolution SEM images and expected hot-spot position. The morphology of nanoflake is expected to generate strong hot-spots uniformly over the gold surface. (C & D) The measured extinction shows 135, 65, 235 and 195nm sequence in extinction intensity at 785-

nm wavelength, and 785-nm SERS measurement also shows the identical sequence of signal intensity. Conditions of SERS measurement were 1mW 785nm CW laser, 10 sec integration, and 1-fM 1,2-bis(4-pyridyl)ethylene MeOH solution. .... 52

**Figure 6.1.** Schematic diagrams of gold viruses for molecular imaging. (A) Representative multifunctions of gold eu-viruses including targeting, delivery, imaging and sensing by sharing viral capsid with optical antenna. The thin gold layer on viral capsid works for optical sensing through molecular spectroscopic methods, and also enhances the other functions by carrying extracellular material including gene, protein, small molecules, fluorescence dyes and so on. (B) Plasmonic selectivity via various viral capsid morphologies. Icosahedral viruses have various 3-D protein structures, as well as diameters ranging from nanometers to micrometers, can be used to attain different plasmonic resonances with metal layer conjugation. (C) Plasmon resonance energy transfer (PRET) and surface-enhanced Raman spectroscopy (SERS) as plasmonic sensor applications for molecular fingerprint spectroscopy. Plasmonic scattering spectrum of metal layers expresses molecular absorbance of nearby target molecules by PRET mechanism. Enhanced local electromagnetic field around the metal layer dramatically increases the molecular Raman scattering which is from molecular vibration. .... 57

**Figure 6.2.** Electromagnetic simulations of gold virus with comparison to a gold conjugation on a similar sized nanosphere. To express an example of viral capsid, a representative equation was taken from the previous literature 24, and (m, p, const) was set to (1, 4, 3.8). Both virus and bead template were scaled to fit to 30-nm diameter. Enhanced electric field is distributed in multiple spots around gold virus, but in a single spot around smooth nanosphere (A & B). Bigger surface-to-volume ratio together with multiple sharp tips induces bigger amount of electromagnetic field scattering to media and less resistive heat inside the metal layer (C & D). These characteristics are beneficial for stable plasmonic optical sensor applications. .... 59

**Figure 6.3.** Gold viral structure and viral activity test. Schematic structure of original virus (A), and its conjugation with gold (D). TEM images were taken before (B) and after metal layer attachment (E). The scale bars in the TEM images are 10 nm. The infectivity of wt-CPMV (C) and gold-CPMV (F) was evaluated by a local lesion assay five days after mechanical inoculation of Cowpea (*Vigna unguiculata*) cv. Chinese x Iron plants. The red arrows indicate the local lesions, which are illustrated at higher resolution in the exploded panels to the right. Taken together, the original structure as well as inherent functions can still be maintained. .... 61

**Figure 6.4.** Characterization of optical properties of various gold viruses. The scattering spectra of 5-nm-gold viruses were measured in 400 to 1100 nm by conventional dark-field spectroscope, (A) belladonna Mottle virus (BdMV) (B) brome mosaic virus (BMV), (C) tomato bush stunt virus (TBMV), and (D) cow pea mosaic virus (CPMV) were conjugated with gold at the same time by metal evaporation. Through further preparation, single

nanoparticles were prepared on a transparent substrate (Supplementary Information). Different sizes and topologies of the viral capsids resulted in variations in the dark-field scattering spectrum. .... 62

**Figure 6.5.** Characterization of optical properties of various gold viruses by change the gold layer thickness. (A to C) The 2, 5, 10nm thickness of gold layer on CPMV virus shows a dramatic change of dark-field scattering. .... 62

**Figure 6.6.** Plasmonic sensing via PRET and SERS for molecular fingerprint information. (A) Schematic illustration of PRET and SERS. Regarding PRET, light scattering of the plasmonic particle is effectively re-absorbed by nearby target molecules, being reshaped with inversely indented absorption spectrum of the molecules. Comparison between before and after molecular presence around a nanoparticle provides the information of molecule's presence and its amount. Regarding SERS, locally-enhanced optical field increases molecular electron vibration, resulting in an increase in Raman scattering which provides molecular structure information. (B) Cytochrome-c PRET experiment results of 5-nm-gold CPMV. Less than 3  $\mu\text{M}$  of cyt-c can be clearly imaged by individual gold CPMVs. This is shown as two dominant dips of 520 and 550 nm in the nanoparticle dark-field scattering that match with cyt-c absorption spectrum. (C) Comparisons of the gold virus PRET with a similar-sized gold-coated nanosphere PRET. (D) SERS spectra of BPE on gold CPMVs and gold-coated nanospheres with a 5-nm gold thickness. Gold CPMV yielded a set of clear fingerprint information at 1200, 1615 and 1635  $\text{cm}^{-1}$  Raman shifts at a pico-mole concentration of BPE, whereas gold-coated nanospheres resulted in a micromole detection. (E) Comparison of Raman scattering intensity in a peak of 1615  $\text{cm}^{-1}$ . The quantitative result shows 6 orders of magnitude greater sensitivity with gold virus. .... 64

**Figure 7.1.** A plasmonic sensor built-in diagnosis chip. A plasmonic sensor array (i.e., eagle-beak nanoantenna) will enable precise detection of molecular fingerprints as well as function as biomolecular separator by using photothermal heat. .... 69

**Figure 7.2.** A microfluidic platform with plasmonic sensors will provide a precise characterization of cellular communication by detecting secretion molecules. .... 70

**Fig. A.1.** Metal deposition process in the eagle-beak fabrication. (A) Schematic diagram of evaporation deposition. By changing the angle of sample to the normal direction of deposition, oblique angle deposition can be applied. (B) Schematic diagram of bending and edge rounding of eagle-beak during the deposition. (C) Scanning electron micrographs of bare laser-interference pillars and eagle-beak structure after deposition, and a wafer-scale eagle-beak substrate ..... 73

<b>Fig. A.2.</b> Process of anodized aluminum oxide. From a 2-mm thickness 99.999% aluminum plate, a series of two step anodization and etching process results in a hexagonally arrayed nanohole structure. The periodicity and depth of hole can be modulated by the condition of anodization. ....	74
<b>Fig. A.3.</b> Au-viruses conjugation processes. (A) After packing viruses on a glass substrate through drop casting method, (B) thin gold layer was deposited on the top by using electron-beam evaporator. The samples in this step were characterized for optical properties and SERS measurement. (C) For single-particle based experiment including PRET characterization, Au-virus particles were monodispersed on a modified glass substrate having thiol exposure. ....	75
<b>Fig. A.4.</b> Electron microscope images of gold virus. (A) SEM image of gold deposited closed packed CPMV on a glass slide. (B) SEM image of monodispersed 5-nm gold CPMV on glass slide. (C) TEM image of 5-nm CPMV showing regular structures. All scale bars are 100 nm; Ones of close-up image in (C) are 20 nm. ....	76
<b>Fig. B.1.</b> Schematic diagram of a setup of Raman spectroscopy built in an inverted microscope. ....	77
<b>Table D.1.</b> Equations involved in molecular movement around eagle-beak. Photothermal heat induces buoyant force (F) in free convection, heat source (Q) in thermal conduction and temperature gradient ( $\nabla T$ ) in the diffusion equation. Plasmonic trapping force which dominantly acts around the hot-spot can be expressed as F with multiplying mobility coefficient ( $\mu$ ) in the diffusion equation. Diffusion coefficient and thermal diffusion coefficient were taken from other references. Other physical factors were followed to general properties of glass, gold and methanol. In those equations, $\rho$ is density of solution, $\eta$ is dynamine viscosity, $C_p$ is heat capacity, $k$ is thermal conductivity and $R$ is reaction rate. ....	78
<b>Table F.1.</b> Thermal gradient ( $^{\circ}\text{C}/\text{m}$ ) comparison between multiphysics simulation and the presented equation. The average of deviations is about 50%. ....	80
<b>Fig. G.1.</b> Optical cross-section comparison between the resonated and non-resonated nanorod. ....	81

## Acknowledgments

First and above all, I give Almighty God the Glory, Honor, Thanks and Praise for providing me this opportunity and granting me the capability to complete my Ph.D. God was a powerful force of encouragement through the journey of my doctoral studies at UC Berkeley and has brought me in contact with the wonderful people who led this study. This dissertation would not have been possible without the guidance and the help of several people who contributed their valuable assistance in the preparation and completion of this study. I would therefore like to offer my sincere appreciation and thanks to all of them.

I would like to express my utmost gratitude to my research advisor Dr. Luke P. Lee, whose guidance, encouragement, understanding, and support helped me to be on the track of the research with strong motivations. His sincere attitude and vision constantly inspired me to grow as what I am now. I appreciate his invaluable instruction and warm supervision. I also gratefully acknowledge the advice and guidance of my dissertation committee, Drs. Liwei Lin, Ming Wu, and Dorian Liepmann.

I want to especially thank all of BioPOETs lab members. Researching in this amazing research group guided me to overcome setbacks and to stay focused on my study. Especially I want to thank to my seniors, Dr. Yeonho Choi, Dr. Taewook Kang, and Dr. Dukhyun Choi for their kind guidance to grow in my early stage of BioPOETs. And I also thank to my fellows Dr. YoungGeun Park, Dr. Seungmin Park, Dr. Jae Young Lee and all of other lab members for their interesting supportive discussions. I also thank to my supportive friends I met during my Ph.D, Dr. Dal Chin, Dr. Qiong Pan, and Paul Kim.

Lastly, but most importantly, I wish to thank my parents, JongMan Hong and MyungJa Kim for the endless support and love they provided me through my entire life and for their prayers; my gratitude to them is beyond any words. I also thank my brother, SoonYong Hong for encouraging me to pursue this degree.

# Chapter 1

## Introduction to Molecular Plasmonics

### 1.1. Fundamentals of Plasmonics

*Plasmonics*, over the last few decades, has been of great interest due to the field's accomplishments and it having provided practical solutions to a variety of long-standing issues not exclusively including nanoscopic imaging [1-4], energy harvesting [5], multiple-harmonic generation [6, 7], optoelectronics [8], plasmonic lithography<sup>9</sup>, and meta-material applications [9, 10]. The framework through which we understand plasmonic phenomena can be interpreted utilizing classical theories (i.e., classical electromagnetism). The fact that a new theoretical perspective need not be developed to understand plasmonic phenomena allowed for their rapid translation to innovative applications. For example, cloaking materials (meta-materials) have long been things of science fiction; fantastic materials that could only exist in our imaginations. However, due to plasmonics and its classically defined theoretical framework, they just might be realized in the near future.

“Plasmon” (or plasma as a plural form) originally indicates a group of ionized gas-like particles which can respond to excitation as a group oscillation to external electric or electromagnetic field. Likewise, metallic nanostructures can hold a group oscillation of free electron under visible light excitation [11]. Consequently, the electron oscillation expresses two different physical forms (similar to gas plasma) of electromagnetic scattering and resistive heat generation (Fig. 1.1). From the Maxwell equations, two energy terms are derived to describe light-and-particle interaction (eq. 1). Here,  $\mathbf{J} \cdot \mathbf{E}$  ( $\mathbf{J}$  and  $\mathbf{E}$  are current density and electric field, respectively) is resistive heat and  $\mathbf{E} \times \mathbf{H}$  ( $\mathbf{H}$  is magnetic field) is electromagnetic scattering.

$$\begin{aligned} P_e &= \int_V \mathbf{E} \cdot \frac{\partial \mathbf{D}}{\partial t} dV = \int_V \mathbf{J} \cdot \mathbf{E} dV \\ P_m &= \int_V \mathbf{H} \cdot \frac{\partial \mathbf{B}}{\partial t} dV = \oint_S (\mathbf{E} \times \mathbf{H}) \cdot \mathbf{n} dS \end{aligned} \quad \text{eq. 1}$$

Equation 1 can be applied to all types of materials including dielectrics. However, unlike other materials, metallic nanostructures can have large magnitudes of  $\mathbf{E}$  and  $\mathbf{H}$  since metallic nanostructure can have a larger optical cross-section than its geometric cross-section. In a

microscopic view, the large optical cross-section is caused by electron oscillation length that is greater than the lattice length, which is different from dielectric materials. Here we will leave other quantitative details such as the electromagnetic field and metallic nanostructure interactions to other literatures but equation 1 contains the necessary information regarding molecular plasmonics fundamentals (or molecular detection via plasmonics), the scope of this thesis.

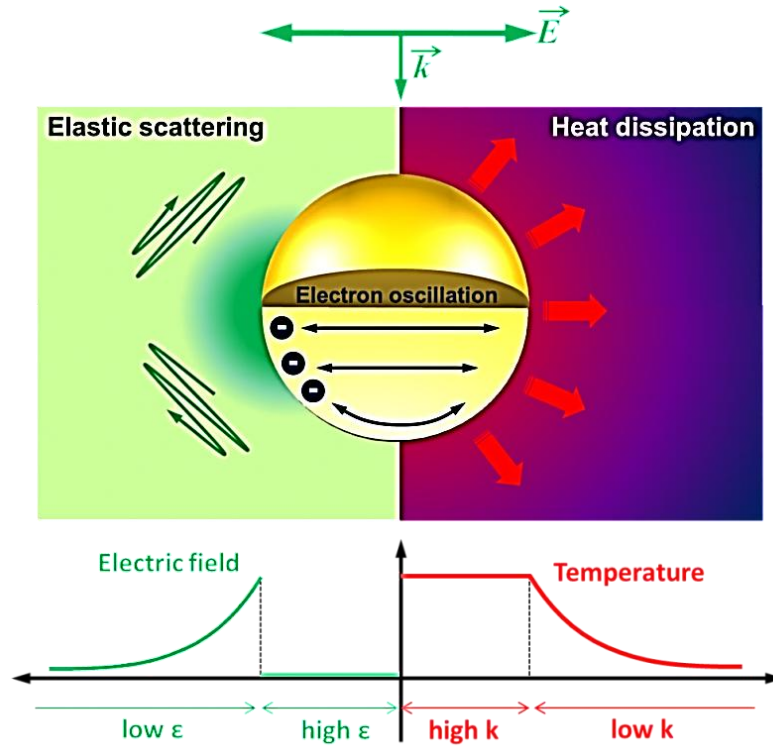


**Figure 1.1.** A metallic nanostructure whose size is similar to or smaller than optical wavelength generates a group oscillation of free electron and consequently expresses two physical forms simultaneously to a surrounding medium: electromagnetic scattering and heat dissipation. Also, the difference of electric and thermal conductivity in the interface of nanostructure causes strong gradient formation of electric and temperature around the nanostructure.

## 1.2. Physical Expressions from Nanoplasmonics

The group oscillation of free electrons in a metallic nanostructure results in a large optical cross-section (up to 10 times larger than the geometrically defined one). Optical energy interacting with the nanostructures is re-radiated to the environment in two forms: an electromagnetic field and photothermal heat. An excited plasmonic structure has been reported to generate amplified electric fields with magnitudes more than 1000 times that of the incident light ( $|E|/|E_0| \sim 10^3$ ) and/or increase temperature by several hundred degrees Celsius. When those fields are re-radiated to a surrounding medium, a plasmonic structure,

due to it being a point source relative to the surrounding medium, generates large gradients in fields by the following equations:

$$\left. \frac{dT_r}{dr} \right|_{r=r_0} = -\frac{Q}{4\pi k r_0^2}$$

$$\left. \frac{dE}{dr} \right|_{r=r_0} = -\frac{q}{2\pi\epsilon_0} \frac{1}{r_0^3}$$

Here,  $Q$  is total resistive heat and  $q$  is local charge. For simplicity, we presently consider the electric field as electrostatic. Since  $r_0$  for nanostructures is small ( $10^{-8} \sim 10^{-6}$  meters), the amplitude of the gradients can be significantly greater than ones for macro-structures and therefore normally ignorable physical phenomena, in order to describe molecular dynamics (such as thermophoresis and optical trapping), cannot be ignored.

Physical expression	Physical factor	Range	Applications
High Electric field	Group oscillation of free electron	$\sim 1000\times$ of incident light	Molecular imaging, multiple harmonic generation
High Temperature	Electron collision with lattice	$\sim 100s$ °C higher	Photothermal therapy Gene delivery
Electric field gradient	Nanometer confinement of high $\epsilon$	$\sim 10^{12}$ V/m <sup>2</sup>	Plasmonic trapping
Temperature Gradient	Nanometer confinement of high $k$	$\sim 10^{10}$ °C/m	Preconcentration
Nonstraight Poynting vector	Large optical cross-section	-	Molecular detection
Depolarized Scattering	Electron motion in scale of boundary	$E_{\perp}/E_{\parallel} \sim 1$	Molecular detection

**Table 1.1.** Physical expressions from excited plasmonic structures. In addition to optical field amplification, many interesting physical points are found from the physical expressions which can be useful for various applications as listed.



The microscopic view of plasmonic phenomena reveals another interesting aspect: depolarized electron motion. Since electron movement in metals is not limited to the lattice, an external electric field induces long-distance electron movement, the path of which is affected by geometry (or boundary), yet the metals are prone to maintain zero electric field. In the case of 2-dimensional and 3-dimensional nanostructures, electron motion cannot be parallel to the external electric field. Since re-emitted optical field stems from the electron oscillation, optical scattering by metallic nanostructures is depolarized compared to incident light. Also, a larger optical cross-section than geometry section implies that electromagnetic field does not propagate as straight around excited plasmonic structures. The bent Poynting vector can also vary a spatial pattern of molecular scattering.

### **1.3. Current Researches of Plasmonic Molecular Detection**

Various molecular detection schemes by using plasmonics have been demonstrated. Here we mainly focus two schemes as they are considered the most promising approaches; these methods are also similar to others in terms of basic mechanism. First, surface-enhanced Raman scattering (SERS) is highlighted along with its research history. Inelastic scattering from molecules contains molecular fingerprint information such as atomic components, bonding types, and vibrational and rotational modes. This concept were found in 1922 by C. V. Raman and named after him. However, the extremely low probability of inelastic scattering versus elastic scattering (i.e., Rayleigh scattering) bottlenecked this technique, but with the discovery of the plasmonic phenomenon, the local enhancement of the optical field at the surface of metallic nanostructures allowed for the facile detection of surface-enhanced Raman scattering in various applications. Due to plasmonic amplification of inelastic scattering events in the time domain, well-designed metallic nanostructures can detect even single molecules with a conventional optical setup [12].

Another interesting plasmonic molecular detection method is plasmon resonance energy transfer (PRET) [13]. While surface-enhanced Raman scattering informs vibrational spectrum, the phenomena of plasmon resonance energy transfer can detect the absorption spectrum of molecules by using a broad wavelength of light. A broad scattering spectrum from a metallic nanostructure encodes the molecular absorption spectrum and propagates to a far-field observer. The decoded absorption spectrum by comparing spectral change can show molecular information in a dynamic in-situ manner [14]. Although successful detection requires several preconditions such as matching of plasmonic scattering spectrum with absorption spectrum of target molecules, the key function of the nanostructures is to amplify the incident electromagnetic field.

From these two representative molecular detection methods, the key function of plasmonic structures is amplification of the incident optical field. The high magnitude of optical field amplification is generally an important characteristic for other plasmonic applications (e.g., multiple harmonic generation and plasmonic energy harvesting). However, to improve plasmonic-aided molecular detection and other applications, the understanding of other aspects of plasmonic characteristics will be helpful.

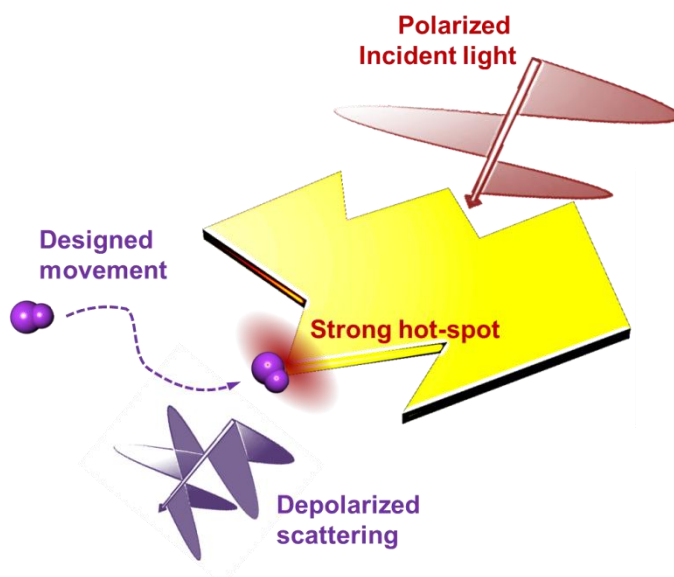


**Figure 1.2.** Outline of this thesis. Improved molecular detection schemes will be discussed by using various aspects of plasmonic expressions. In addition of strongly amplified optical field, the gradients of electric and thermal field will be studied for molecular preconcentration in the hot spots, and also depolarization induced by electron motion nonparallel to incident light will be studied for molecular detection by a polarization contrast or spectral variation.

## 1.4. Outline of Thesis

This thesis will discuss how to utilize physical expressions of optically excited metallic nanostructures to improve molecular detection schemes. Particularly the thesis contains, not in the sequence but contents-wise, four categories of (1) plasmonic structure design and fabrication, (2) preconcentration for temporally stable molecular detection (i.e., non-blinking single-molecule detection), (3) non-straight Poynting vector and depolarization scattering, and (4) photothermal physics for molecular delivery.

The plasmonic designs shown in the following chapters are eagle-beak nanoantenna, nanoflake and gold viruses. The eagle-beak nanoantenna is designed to demonstrate preconcentration-based single-molecule SERS and the gold nanoflake is designed as a practical substrate for frequency selectivity and detection sensitivity. While the former two designs are for a large-area uniform substrate, the gold virus is designed as ideal nanoparticles for sensitive molecular detection and also multi-functions for therapeutic purposes.

We also introduce a concept of molecular preconcentration for temporally stable molecular detection. Since optical amplification is limited to a-few-cubic-nanometers ( $\text{nm}^3$ ) volume around plasmonic structures, the probability of molecular detection is extremely low in single-molecule level concentrations. In chapter 2, the theoretical schemes will be introduced to modulate molecular motion toward plasmonic nanostructures by using electric-

field and thermal gradients; thus molecular signal being stable along a time (i.e., non-blinking).

Also, depolarization and non-straight Poynting vector will be discussed in terms of in-depth understanding of molecular scattering as well as new molecular detection schemes in chapter 4 and 5. In these chapters, optical field will be considered as vectors consisting of a plane of electric and magnetic fields and Poynting vector. We believe that in addition to the amplification of optical field, metallic nanostructures can change spectrum profile or scattering spatial pattern which can enrich molecular fingerprint information as well as function as a new molecular detection methods.

As another interesting application using photothermal heat, extrinsic biomolecule delivery and activation via plasmonic carriers will be discussed in chapter 3. Metallic nanoparticles are used as biomolecular delivery vectors due to various advantages, including remote activation of carried molecules with a high temporal and spatial resolution. This scheme will be discussed in terms of photothermal physics and a design method for heat generation will be suggested to various molecular delivery schemes (specifically for gene delivery).

## Reference

- [1] T. H. Taminiau, *et al.*, "Near-field driving of a optical monopole antenna," *Journal of Optics a-Pure and Applied Optics*, vol. 9, pp. S315-S321, Sep 2007.
- [2] E. Trevisan, *et al.*, "Novel approaches for scanning near-field optical microscopy imaging of oligodendrocytes in culture," *Neuroimage*, vol. 49, pp. 517-524, Jan 1 2010.
- [3] F. De Angelis, *et al.*, "Nanoscale chemical mapping using three-dimensional adiabatic compression of surface plasmon polaritons," *Nature Nanotechnology*, vol. 5, pp. 67-72, Jan 2010.
- [4] H. Eghlidi, *et al.*, "Resolution and Enhancement in Nanoantenna-Based Fluorescence Microscopy," *Nano Letters*, vol. 9, pp. 4007-4011, Dec 2009.
- [5] H. A. Atwater and A. Polman, "Plasmonics for improved photovoltaic devices (vol 9, pg 205, 2010)," *Nature Materials*, vol. 9, pp. 865-865, Oct 2010.
- [6] I. Y. Park, *et al.*, "Plasmonic generation of ultrashort extreme-ultraviolet light pulses," *Nature Photonics*, vol. 5, pp. 678-682, Nov 2011.
- [7] S. Kim, *et al.*, "High-harmonic generation by resonant plasmon field enhancement," *Nature*, vol. 453, pp. 757-760, Jun 5 2008.
- [8] E. Ozbay, "Plasmonics: Merging photonics and electronics at nanoscale dimensions," *Science*, vol. 311, pp. 189-193, Jan 13 2006.
- [9] D. Schurig, *et al.*, "Metamaterial electromagnetic cloak at microwave frequencies," *Science*, vol. 314, pp. 977-980, Nov 10 2006.
- [10] Z. W. Liu, *et al.*, "Far-field optical hyperlens magnifying sub-diffraction-limited objects," *Science*, vol. 315, pp. 1686-1686, Mar 23 2007.
- [11] S. A. Maier, "Localized Surface Plasmons Plasmonics: Fundamentals and Applications," ed: Springer US, 2007, pp. 65-88.
- [12] M. Moskovits, "Surface-enhanced Raman spectroscopy: a brief perspective," *Surface-Enhanced Raman Scattering: Physics and Applications*, vol. 103, pp. 1-17, 2006.

- [13] G. L. Liu, *et al.*, "Quantized plasmon quenching dips nanospectroscopy via plasmon resonance energy transfer," *Nature Methods*, vol. 4, pp. 1015-1017, Dec 2007.
- [14] Y. H. Choi, *et al.*, "Plasmon Resonance Energy Transfer (PRET)-based Molecular Imaging of Cytochrome c in Living Cells," *Nano Letters*, vol. 9, pp. 85-90, Jan 2009.

## Chapter 2

### Eagle-beak Nanoantenna for Nonblinking Single-Molecule SERS via Preconcentration

Optical field enhancement is the most promising advantage of optical nanoantennae, which enables high sensitivity of molecular detection even down to single-molecule level. However, its temporal instability, which is rather thought as a trait of single-molecule level detection, can be a limitation to practical applications. Here we suggest *preconcentration*-based nonblinking single-molecule SERS by a new design, eagle-beak nanoantenna. Whereas photothermal heat around optically resonated nanoantennae usually causes random signal blinking, eagle-beak nanoantenna is to utilize asymmetric thermal profile to attract target molecule close; and hot-spot formation around large-curvature tip in the antenna can also function to draw target molecule nearby by high electric-field gradient. In experiments high enhancement factor ( $\sim 10^{15}$ ) and low detection limit ( $\sim$ femtomolar) were attained without signal blinking; time-resolvable measurement showed that the high sensitivity and stability are from reversible preconcentration. This study indicates that a well-designed nanoantenna can be utilized not just for optical field enhancement but for manipulating molecular movement in various nanoscale applications.

#### 2.1. Introduction

Raman spectroscopy has been highlighted as a powerful molecular spectroscopic technique due to its high contrast in frequency domain, molecular fingerprint spectrum and non-invasive detection [1]. In developing this technique, the main difficulty has been overcoming the low intensity of Raman scattering. The discovery of surface-enhanced Raman scattering (SERS) [2, 3] has been the most attractive and practical development for overcoming the low signal intensity due to its simple requirements in optical setup. Even though the exact mechanism has not been verified yet, it is generally accepted that optically resonated metallic nanostructures (called ‘*optical nanoantenna*’ in comparison with macro RF antennas) dramatically increase Raman scattering of molecules close or attached to their surface [4, 5]. SERS, therefore, has been considered one of the main applications for nanoantenna research.

High enhancement of the Raman signal is the main goal in SERS research, and nanoantenna design has been considered the key to highly sensitive SERS. The ability of a nanoantenna to strongly focus light into a volume of a few attoliters (known as a ‘*hot-spot*’) is the most dominant physical phenomenon for achieving high sensitivity and resolution in

SERS [6]. Sharp tips and close tip-to-tip distance have been the main approaches to generating strong hot-spots [7], and metal nanostructures, randomly formed or intentionally designed for this concept, have detected extremely low concentration of target molecules (even down to signal-molecule level) [8, 9]. Alone however, this “nanolens” or field-focusing function does not guarantee temporally stable detection at a single-molecule level since the presence of targeted molecules in the attoliter hot-spot is not statistically guaranteed at low concentrations. This suggests that nanoantennas for sensor applications should have the additional ability of increasing the probability of molecules collecting around the hot-spot. Here, we propose a unique nanoantenna design called ‘eagle-beak’ to detect target molecules in single-molecule level with enhanced temporal stability. The high sensitivity and stability are caused by locally increased concentration (or *preconcentration*), which we assert is from thermal and electric-field gradients formed around the ‘eagle-beak’ nanoantenna.

## 2.2 Design Factors of ‘Eagle-beak’

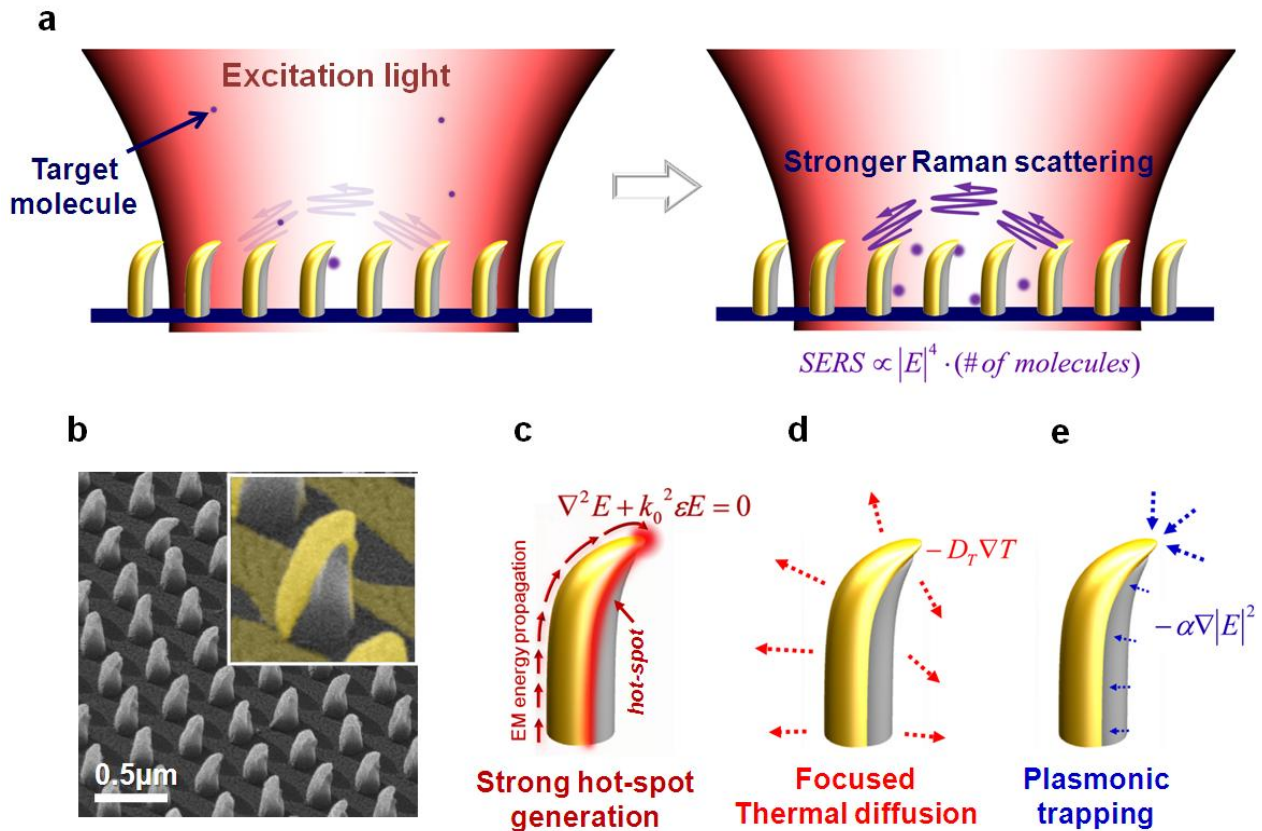


**Figure 2.1.** Schematic diagrams for highly enhanced stable SERS signal via eagle-beak nanoantenna. (A) The eagle-beak nanoantenna concentrates target molecules to the nearby volume around the nanoantenna during plasmonic excitation. More molecules concentrated around the SERS-enable volume generate higher and more stable SERS signal. (B) SEM images

of fabricated eagle-beak nanoantenna structures which consist of a bent polymer pillar and asymmetric tapered gold layer. (C) A strong hot-spot is generated around the edge at the side wall and the tip. Electromagnetic energy ( $\vec{E} \times \vec{H}^*$ ) harmonically propagates along the structure and is focused at the tip. (D) Asymmetric bent metal layer dissipates heat to surrounding media, making asymmetric thermal gradient. Thermal diffusion along thermal gradient concentrates molecules around the bottom of the eagle-beak with fluidic motion induced by thermal buoyant force. (E) The focused E-field decreases exponentially in the media, and its gradient amplitude can overcome the lower limits of possible particle size set by conventional optical trapping. Tip-based eagle-beak nanoantenna can trap nanometer-sized molecules to the strong hot-spot with this mechanism.

The *eagle-beak* design shown in Fig. 2.1 was conceptually inspired and designed to mimic a sharp beak shape and effectively function as a nanolens. The geometric factors and expected functions of *eagle-beak* can be summarized in four parts: (1) the gradually-tapered metal structure supports harmonically propagating electromagnetic waves and condenses a plasmonic electron cloud at the tip, forming hot-spots and a strong electric field (E-field) gradient (2) the metal crescent-shape structure has two sharp edges along the side wall where hot-spots are expected to form; (3) the convex metal layer asymmetrically dissipates heat and can thermally push molecules to a focal point around the cold substrate (4) a sharp vertex at the end of the structure helps fluid generate vortices. The first and second factors help attain strong hot-spots, and the third and fourth together with the first help trap molecules around the *eagle-beak* as will be described later. The combination of these characteristics can concentrate target molecules around the eagle-beak nanoantennas when excited by a resonant incident light (Fig. 2.1).

## 2.3. Function of ‘*Eagle-beak*’

### 2.3.1 Local Field Amplification of *Eagle-beak*

In regards to the generation of strong *hot-spots* (a basic requirement for sensitive SERS) the *eagle-beak* focuses harmonically propagating electric and magnetic fields around the sharp tip [10]. As Fig. 2.2 shows, the strongest *hot-spot* occurs at the structure’s tip with normally incident light polarized parallel to tip direction. The E-field amplitude can be three orders of magnitude higher than that of incident light. E-field concentration can also occur along the long vertical edges of the gold; the cross-section of eagle-beak is similar to a conventional SERS-enhancing crescent structure as demonstrated before [11].

The plasmonic response of the eagle-beak is analogous to a macro RF antenna. When the incident light is matched with the plasmonic eigenvalue & eigenvector of the structure, the optical resonance results in harmonic propagation of electromagnetic energy  $\vec{E} \times \vec{H}^*$  by forming standing waves of both electric and magnetic field (Fig. 2.2A & B). Existence of standing waves along the longitudinal axis suggests that plasmonic resonance can be tuned by changing the height of the *eagle-beak*, analogous to tuning a macro antenna’s electrical



length [12]. Additional simulations showed that the resonance shifts with a 1:2 ratio of wavelength to height of pillar, which also follows that of macro RF antennas.

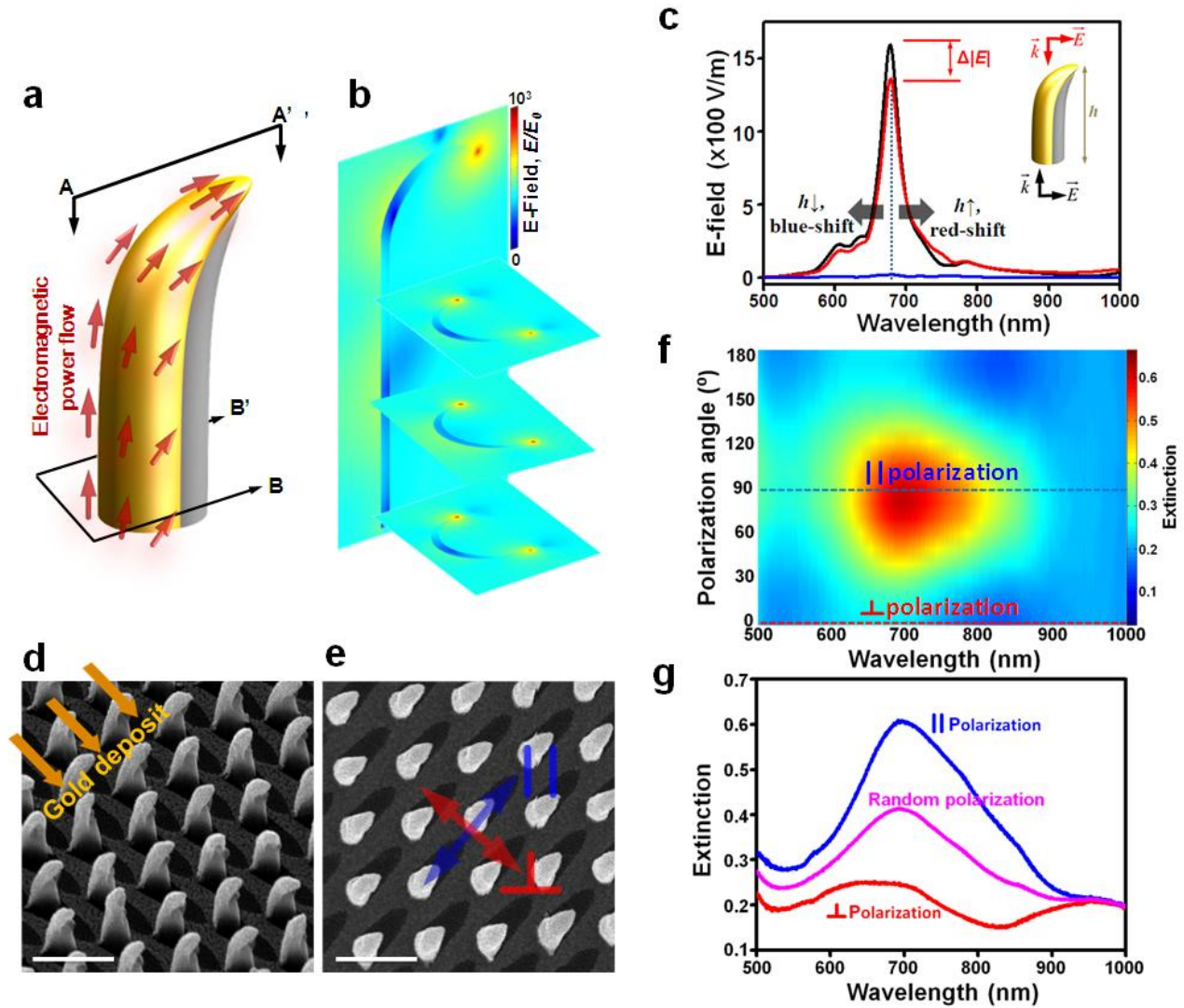


**Figure 2.2.** Optical response of eagle-beak nanoantenna. (A) Schematic diagram of electromagnetic (EM) power flow along the tapered metal layer. This power propagation results in the strongest hot-spot at the tip and weaker hot-spots along the two long edges. The geometric dimensions (the length: 550 nm, the diameter: 120 nm) were decided by fabrication constraints and tuning the plasmonic resonance to visible light (B) Simulated electric-field distribution around optically resonated eagle-beak nanoantenna. E-field enhancement reaches three orders of magnitude at the tip. (C) Simulated E-field intensity at the tip of the designed eagle-beak versus excitation wavelength. Bottom-to-top incidence (black line) focuses more EM power to the tip than top-to-bottom incidence (red line), both have a polarization parallel to AA' line in (A). Perpendicular polarization doesn't form strong enhancement at the tip (blue line). (D & E) SEM images of fabricated eagle-beak nanoantenna. The scale bar in the image is 500 nm. Oblique deposition of gold on laser interference pillar substrate (annotated arrow) fabricated eagle-beak



structure forms an asymmetric nanoantenna. In the top view e, parallel polarization (||) to the eagle-beak tip is shown as blue line, and perpendicular polarization in red. Due to the asymmetry, eagle-beak nanoantenna array has a strong polarizability in the optical response as shown in simulation results. (F) Measured extinction spectra on eagle-beak array by varying polarization angle of incident light. The contour map shows strong resonance of the array to parallel polarization incidence (||), while perpendicular polarization incidence (T) doesn't generate clear resonance in the wavelength range. (G) Measured extinction spectra for parallel, perpendicular and random polarizations. The random polarization results in the exact average of the ones of parallel and perpendicular polarizations.

The fabricated eagle-beak shown in Fig. 2.2D & E agrees well with optical simulation results including polarizability (Fig. 2.2F & G). Extinction measurements indicate that the eagle-beak array has a strong optical resonance at 680nm for normal incidence and proper polarization (noted as || polarization in Fig. 2.2), while perpendicular polarization did not show a clear optical resonance. This substrate could be used for a study of Raman scattering polarization (which provides further molecular information [13]) but here we only consider the polarization dependence for fabrication verification and optimizing laser polarization. Due to its plasmonic features, such as strong *hot-spots* and tunability, the *eagle-beak* fulfills the requirements for a SERS substrate.

### 2.3.2. Preconcentration around *Eagle-beak*

As mentioned earlier, the eagle-beak nanoantenna has been designed to increase probability of molecular presence in hot-spots by thermal and electric-field gradients to increase local concentration of target molecules. The reason why the two gradients can be effective in molecular movement can be discussed based on the following equation:

$$j = c\vec{u} - D\nabla c - cD_T\nabla T + c\mu F \quad eq. (1),$$

here  $j$  is target molecule flux ( $M\cdot m/sec$ ),  $c$  is concentration ( $M$ ),  $\vec{u}$  is fluidic velocity ( $m/sec$ ),  $D$  is diffusion coefficient ( $m^2/sec$ ),  $D_T$  is thermal diffusion coefficient ( $m^2/sec/K$ ),  $T$  is temperature ( $K$ ),  $\mu$  is mobility ( $\mu=D/kT$ ,  $k$  is Boltzmann constant) and  $F$  is plasmonic trapping force ( $N$ ). The eq. (1) helps compare fluidic motion, mass diffusion, thermal diffusion and plasmonic trapping for molecular flux. Resistive heat plasmonically generated in the gold layer induces a thermal gradient in the surrounding fluid, as well as indirectly inducing free convection and localized vortices (Fig. 2.3B & C). Localized vortices around the eagle-beak cause molecules to stay around the eagle-beak for a longer time where hot-spot forms. Moreover, the thermal gradient focused into the spot surrounded by nearby eagle-beaks results in a dominant force causing molecules to be trapped nearby eagle-beak. Fluxes in eq. (1) suggest much clear comparison. Thermal diffusion flux,  $D_T\nabla T$  is much bigger in order than convective flux,  $\vec{u}$  with rough assumption of thermal diffusion

coefficient of nm-sized molecules as the order of  $10^{-9}$  [14]. Therefore, thermal forces cause by resistive heat can effectively work as preconcentration around eagle-beak with the assistance of local vortices (Fig. 2.3A).

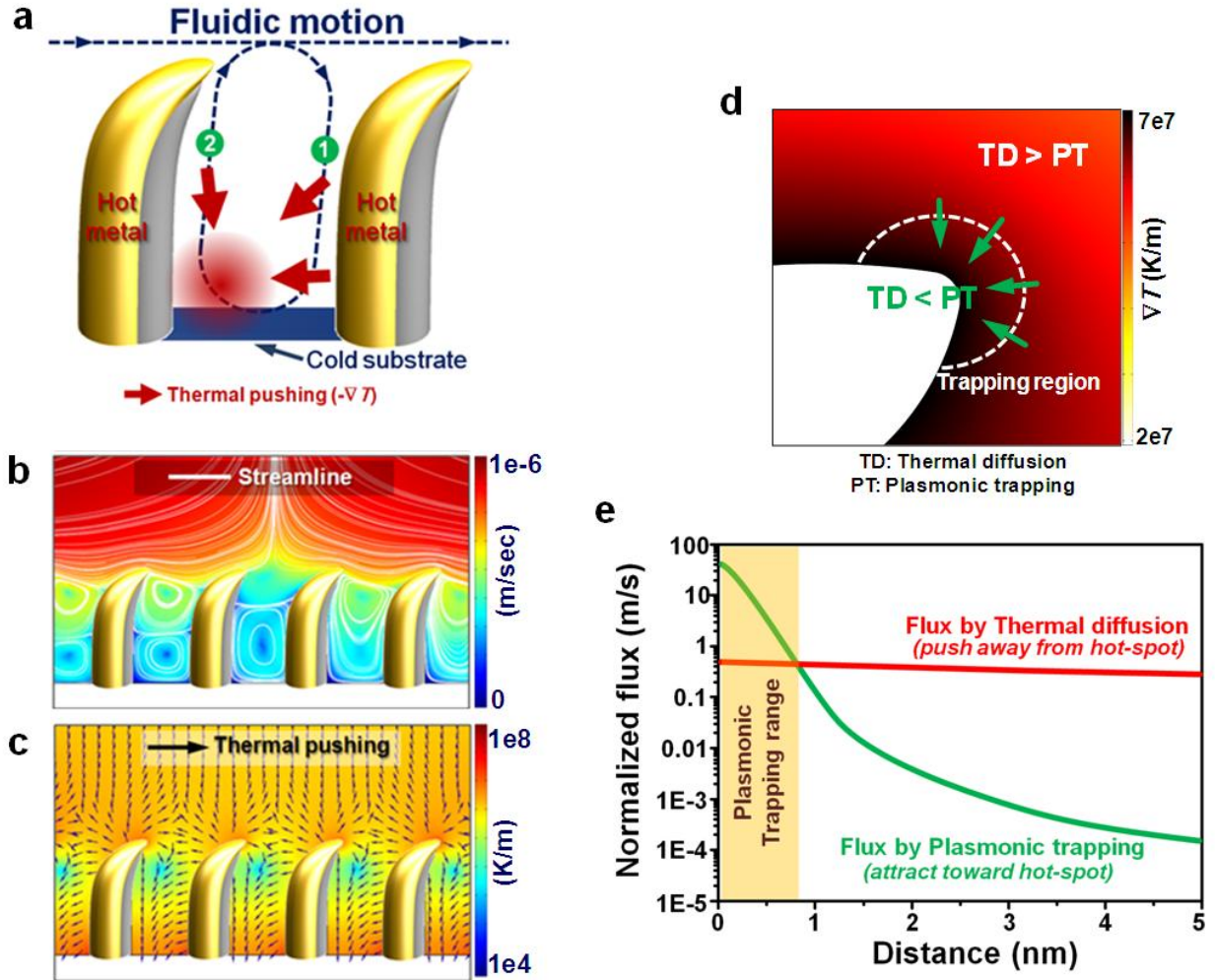


**Figure 2.3.** Proposed mechanism of preconcentration. (A) Schematic diagram of thermal diffusion based preconcentration. Thermal gradient generated by *hot* bent eagle-beak and *cold* substrate gathers target molecules nearby the eagle-beak. (B) Free convection flow around the eagle-beak. Convective flux of target molecules is  $10^{-6}$  m/sec around the top of eagle-beak. (C) Thermal diffusion caused by photothermal effect on the substrate. Its flux reaches -1 to -2 orders of magnitude for nanometer-sized molecule ( $D_T: 10^{-10} \sim 10^{-9}$  ( $\text{m}^2/\text{sec/K}$ )), which is much higher than convective flux. (D) Schematic diagram of plasmonic trapping. A defined volume has a positive trapping force where (Thermal diffusion force) < (Plasmonic trapping force). (E) Normalized flux comparison from thermal diffusion and plasmonic trapping. In the tip-based hot-spot, the electric-field gradient has potential to generate strong plasmonic trapping forces which overcome thermal diffusion.

The strong E-field gradient generation around the nanoantenna allows for optical trapping at the nanoscale (here distinguished by being called plasmonic trapping). Conventional optical trapping methods are not effective on particles smaller than a few hundreds-of-nanometers mainly due to the limited amplitude of the E-field gradient formed by dielectric lenses [15]. Because the E-field is focused at the sharp tip and decays in dielectric media within ten nanometers from the surface, the amplitude of the E-field gradient from nanoantennas is much higher than from conventional dielectric lenses (Fig. 2.2B). Optical trapping equations, ( $F = \frac{\alpha}{2} \nabla |E|^2$  and  $\alpha \propto r^3$ ), imply that particles a few nanometers in size require an E-field gradient six orders of magnitude higher compared to particles hundreds of nanometers in size. Since the nanoantenna has the potential to achieve such a high E-field gradient, the optical force involved around nanoantennas can be considered as a molecular driving force.

Electromagnetic simulations show an E-field gradient of 25 orders of magnitude ( $V/m^2$ ) around the eagle-beak's tip when a 1 mW laser is focused on a 1  $\mu m$ -radius spot. Rough assumptions regarding  $\alpha$  as a 1 nm-size molecule [16] show that the flux due to the plasmonic trapping force is several orders of magnitude higher than convective and thermally diffusive flux (Fig. 2.3E); therefore the plasmonic trapping forces acting to collect molecules into the hot-spot. The combination of thermal diffusion and plasmonic trapping can be explained as ones of main physical causes of preconcentration shown in experiments later.

## 2.4. Fabrication of Nano Eagle-beak

Another strength of the eagle-beak antenna is that the design allows for easy batch-sized fabrication over a large area without using any commonly-used serial fabrication steps, like electron-beam lithography [17] or focused ion-beam [18]. The two main techniques used are laser-interference lithography (LIL) [19] and oblique angle metal deposition. Both are easily applied to wafer-size uniform fabrication. Because a uniformity of fabrication is essential for reliable sensing applications, we took advantage of the highly ordered and dense LIL pillars by using them as the initial substrate. Moreover, a high hot-spot density can be achieved with the sub-optical period of LIL; this allows for more reliable and quantitative detection. Here, LIL pillars were fabricated on 4" wafers with a height of 550 nm and a period of 375 nm, which was determined by photoresist thickness and a half wavelength of interfering laser, respectively.

An oblique angle deposition of 20 nm of gold was applied to the LIL pillars specifically at a 35 degrees from the normal direction of the wafer to prevent the shadow of deposited gold of each pillar from touching the bottom of its diagonally neighboring pillar (Fig. 2.2D & E). Consequently, all gold structures on the wafer were connected by the thin gold film, which allows the distribution of photothermal heat to a larger area and avoids the common problem of structural deformation via melting during SERS measurements [20]. This continuous heat dissipating thin film structure is considered a large factor in the eagle beak's long-term

stability. Even 10 months after fabrication, the substrate maintained the same detection limit in the experiments described later.

## 2.5. Surface-enhanced Raman Scattering Measurement

### 2.5.1. Highly Enhanced Raman Signal via *Eagle-beak*

Highly sensitive Raman scattering detection is a strong application of the eagle-beak nanoantenna due to its high E-field enhancement, and can be indirectly used to experimentally address the nanolens functionality. First, SERS of benzenethiol adsorbed on the gold surface was measured by fixing laser polarization and rotating the sample (Fig. 2.4A). As expected, we observed a change of Raman spectra depending on the sample rotation angle. The highest intensity was measured in the parallel polarization, while the perpendicular polarization did not result in a clear spectrum (Fig. 2.4B). The polarization dependence of Raman scattering intensity which is well fit to a sinusoidal curve of  $180^\circ$  period (Fig. 2.4C), along with the optical extinction measurement, show that the fabricated eagle-beak substrate has optical characteristics matched to the simulation.

A SERS sensitivity test was done by measuring methanol-based 1,2-Bis(4-pyridyl)ethylene (BPE) at the optimal sample rotation angle. The concentrations of BPE tested ranged from 1 fM to 10 pM for SERS measurements (Fig. 2.4D), and the measurements of each concentration clearly showed a characteristic spectral fingerprint at 1200, 1617 and 1636  $\text{cm}^{-1}$  [21] with good signal-to-noise ratios (i.e. at 1 fM, SNR is around 36). For comparison, Raman spectra were measured from 0.5 M BPE with no enhancing substrate. The analytical enhancement factor defined in Fig. 2.3 reached a factor of  $10^{15}$  at 1220  $\text{cm}^{-1}$  peak (Fig. 2.4E). In order to confirm that the SERS EF was the result of the eagle beak structure and not merely gold grains, different-sized photoresist pillars on the same quartz substrate were Au coated together with the eagle beak. These pillars showed no optical resonance at 785nm and SERS measurements in concentrations up to 1  $\mu\text{M}$  BPE showed no clear Raman signals. The huge eagle beak EF, which has not previously been reported in a uniform SERS substrate, as well as detection of femto-mol concentrations, demonstrates the high sensitivity of the *eagle-beak* structure down to single-molecule level detection.

### 2.5.2 Temporal Stability of SERS via *Eagle-beak*

In addition to the high sensitivity, the *eagle-beak* structure gives high SERS signal stability in MeOH-BPE solution. While many examples of single-molecule detection suffer from signal blinking [8, 22], the enhanced Raman signal by the *eagle-beak* did not show any significant temporal fluctuation even in concentrations much less than the lowest concentrations previously reported. To determine the temporal stability of the Raman spectrum, contiguous 1-sec integrations were measured from a fixed  $1\ \mu\text{m}^2$  area centered at

the laser spot by opening and closing the laser shutter (Fig. 2.5A & B). The continuous Raman spectra showed an initial signal increase and stabilized a few seconds after opening the laser shutter. Not only was the signal constant, but this result suggests reversible preconcentration of target molecules at the laser spot with no adsorption on the nanoantenna surface.

Another experiment was performed to determine molecule preconcentration during optical excitation of the eagle-beak substrate (Fig. 2.5C). Two objective lenses were used to focus 785 and 532 nm lasers (from above and below respectively) onto the eagle-beak substrate which was immersed in 10 pM MeOH-BPE. The 785 nm laser was used to excite plasmonic phenomena on the eagle-beak substrate, while the 532 nm laser was used to excite the BPE and profile its spatial distribution by its fluorescence. When the fluorescent excitation (532 nm laser) spot overlapped the 785 nm excitation area, the fluorescence intensity was increased, indicating higher concentration of BPE (Fig. 2.5D). Also, the fluorescent intensity took 2~3 seconds to return to its previous level after extinguishing the 785 nm laser. This result supports reversible molecular preconcentration occurring only during the plasmonic excitation of the eagle-beak.

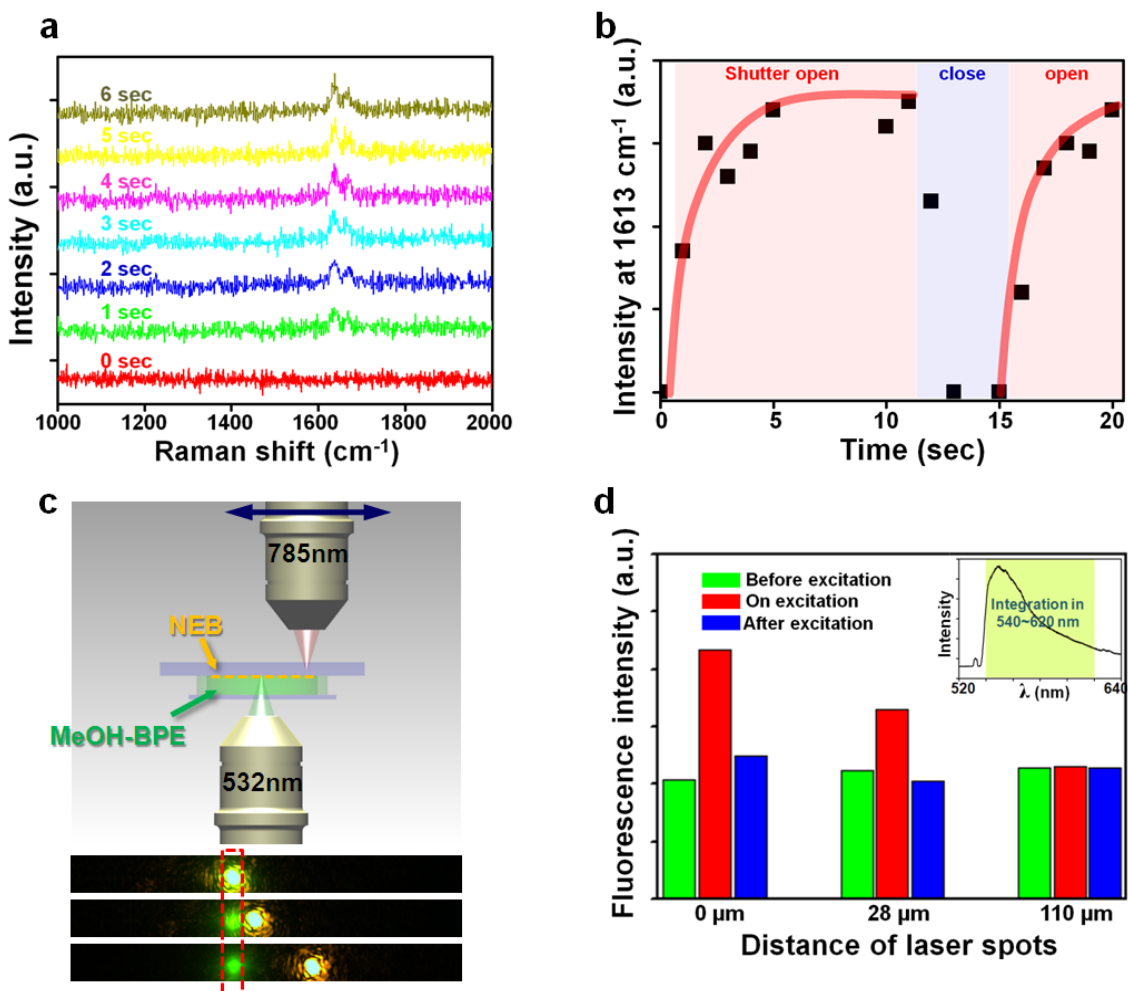


**Figure 2.5.** Temporal stability of SERS signal. (A) Time-resolved spectra of 1fM MeOH-BPE. The same experimental conditions were used. Subsequent spectra show a continuous increase of SERS signal and stabilization in a few seconds upon 785nm laser excitation. (B) Repeatable signal increase/saturation of SERS signal by laser excitation. Repeating open and close laser shutter showed the same repeating of signal increase and saturation. The target molecule is considered to gather during the laser excitation and scatter after the excitation in the solution. (C) Experimental scheme for analyzing concentration distribution change by eagle-beak substrate excitation of 785nm laser. Two opposing 20x objectives were used to focus 785nm and 532nm lasers. Center to center distance of the laser spots was changed to 0, 28, and 110  $\mu\text{m}$  (three true color images taken through a CCD camera connected to bottom objective display three different laser locations). (D) Local concentration increase by 785nm laser excitation. Fluorescence signal excited by 532 nm laser (3-sec integration) was used to determine BPE concentration. Inset plot shows a BPE fluorescence spectrum. 785nm laser was shined for 10 sec and off before 532nm excitation. The intensity of fluorescence was attained by integrating the spectrum in 540 to 620nm. Three independent experiments on different spots on the substrate showed the repeatable increase of concentration at the 785nm laser focus spot. The area apart from the 785nm excitation did not show any increase of fluorescence intensity.

## 2.6. Conclusion

In this study, we demonstrated a potential function of manipulating molecular motion by field gradients around excited nanoantennae, especially for low-concentration molecular detection. The gradually tapered asymmetric eagle-beak nanoantenna achieved single-molecule SERS detection. Based on simulation and experiments, the eagle-beak nanoantenna generates strong hot-spots at the tip and along the long edges. Time-dependent SERS measurements and fluorescence-based concentration distributions strongly suggest that increased local concentration is a large factor in increasing the SERS enhancement as well as producing temporally stable signals. We also analytically support the hypothesis that the preconcentration mechanism is due to thermal and electric-field gradients around the nanoantenna. From this study, preconcentration-based sensitivity and stability in molecular detection can enhance a next generation of high-sensitivity single-molecule detection, and expand to various nanoplasmonic applications including plasmonic energy harvest, optical communication, and biomedical applications.

## Reference

- [1] C. V. K. Raman, K. S., "The Optical Analogue of the Compton Effect," *Nature*, vol. 121, p. 711 1928.
- [2] D. L. Jeanmaire and R. P. Vanduyne, "Surface Raman Spectroelectrochemistry .1. Heterocyclic, Aromatic, and Aliphatic-Amines Adsorbed on Anodized Silver Electrode," *Journal of Electroanalytical Chemistry*, vol. 84, pp. 1-20, 1977.
- [3] M. G. Albrecht and J. A. Creighton, "Anomalously Intense Raman-Spectra of Pyridine at a Silver Electrode," *Journal of the American Chemical Society*, vol. 99, pp. 5215-5217, 1977.

- [4] G. C. Schatz, *et al.*, "Electromagnetic mechanism of SERS," *Surface-Enhanced Raman Scattering: Physics and Applications*, vol. 103, pp. 19-45, 2006.
- [5] A. Campion and P. Kambhampati, "Surface-enhanced Raman scattering," *Chemical Society Reviews*, vol. 27, pp. 241-250, Jul 1998.
- [6] J. Gersten and A. Nitzan, "Electromagnetic Theory of Enhanced Raman-Scattering by Molecules Adsorbed on Rough Surfaces," *Journal of Chemical Physics*, vol. 73, pp. 3023-3037, 1980.
- [7] H. X. Xu, *et al.*, "Electromagnetic contributions to single-molecule sensitivity in surface-enhanced Raman scattering," *Physical Review E*, vol. 62, pp. 4318-4324, Sep 2000.
- [8] S. M. Nie and S. R. Emery, "Probing single molecules and single nanoparticles by surface-enhanced Raman scattering," *Science*, vol. 275, pp. 1102-1106, Feb 21 1997.
- [9] K. Kneipp, *et al.*, "Single molecule detection using surface-enhanced Raman scattering (SERS)," *Physical Review Letters*, vol. 78, pp. 1667-1670, Mar 3 1997.
- [10] D. K. Gramotnev, *et al.*, "Optimized nonadiabatic nanofocusing of plasmons by tapered metal rods," *Journal of Applied Physics*, vol. 104, pp. -, Aug 1 2008.
- [11] K. B. Li, *et al.*, "Surface enhanced Raman scattering on long-range ordered noble-metal nanocrescent arrays," *Nanotechnology*, vol. 19, pp. -, Apr 9 2008.
- [12] R. Bansal, "Antenna Theory - Analysis and Design - Balanis, Ca," *Proceedings of the Ieee*, vol. 72, pp. 989-990, 1984.
- [13] J. M. Grzybowski, *et al.*, "Evidence of Ion-Pairing in Polarized Raman-Spectra of a Ba<sup>2+</sup>-Cro-4(2-) Doped Ki Single-Crystal," *Journal of Raman Spectroscopy*, vol. 4, pp. 25-30, 1975.
- [14] S. Duhr and D. Braun, "Thermophoretic depletion follows Boltzmann distribution," *Physical Review Letters*, vol. 96, pp. -, Apr 28 2006.
- [15] K. C. Neuman and A. Nagy, "Single-molecule force spectroscopy: optical tweezers, magnetic tweezers and atomic force microscopy," *Nature Methods*, vol. 5, pp. 491-505, Jun 2008.
- [16] K. C. Neuman and S. M. Block, "Optical trapping," *Review of Scientific Instruments*, vol. 75, pp. 2787-2809, Sep 2004.
- [17] R. E. Howard, *et al.*, "Microfabrication as a Scientific Tool," *Science*, vol. 221, pp. 117-121, 1983.
- [18] J. A. Veerman, *et al.*, "High definition aperture probes for near-field optical microscopy fabricated by focused ion beam milling," *Applied Physics Letters*, vol. 72, pp. 3115-3117, Jun 15 1998.
- [19] J. P. Spallas, *et al.*, *J. Vac. Sci. Technol. B*, vol. 13, 1995.
- [20] A. Wijaya, *et al.*, "Selective Release of Multiple DNA Oligonucleotides from Gold Nanorods," *Acs Nano*, vol. 3, pp. 80-86, Jan 2009.
- [21] W. H. Yang, *et al.*, "A surface-enhanced hyper-Raman and surface-enhanced Raman scattering study of trans-1,2-bis(4-pyridyl)ethylene adsorbed onto silver film over nanosphere electrodes. Vibrational assignments: Experiment and theory," *Journal of Chemical Physics*, vol. 104, pp. 4313-4323, Mar 15 1996.
- [22] S. R. Emory, *et al.*, "Re-examining the origins of spectral blinking in single-molecule and single-nanoparticle SERS," *Faraday Discussions*, vol. 132, pp. 249-259, 2006.



## Chapter 3

### Photothermal Physics for Optical Gene Regulation

Regulating gene expression by introducing foreign genes to individual cells has a great potential in fundamental biological science[1-3] to gene therapies[4-6] since complexity of cellular expression is managed by relatively simple biological information flow from DNA. The more advanced controllability in time and space domain of gene expression assures the more understanding in biology as well as highly efficient therapy tool in medical applications. In this respect, gold nanoparticle can be considered as the most versatile and efficient carrier due to the characteristics studied here. In brief, photothermal effect on gold nanoparticle modulates thermal profiles such as temperature and its gradient with high temporal and spatial localization. Also, variation in nanoparticle size and excitation light intensity provides the further controllability on the temperature and thermal gradients. Together with available surface chemistry, gene delivery with gold nanoparticle carrier will be a strong platform having versatile gene delivery scenarios.

#### 3.1 Introduction

Temporal controllability as well as spatial controllability in gene regulation must be attained to make a clear blueprint on the complexity. Among various gene carriers, gold nanoparticle is considered as the most versatile and efficient for the spatio-temporal controllability. The studies here can be a stepstone toward an important factor by understanding photothermal effects on nanoparticles, and furthermore suggest guidance toward the experimental design.

A recombinant virus containing gene of interest is considered as the most common vector for gene delivery, and has been demonstrated in various research and therapy fields. However, the inherent severe side effect including immune response and insertional mutagenesis (sometimes leading to death, carcinogenesis or germ-cell-line alterations) encourages alternative methods for nonviral vectors; including polymers[7], dendrimer[8], liposome[9], nanotubes[10] and metal nanoparticles. Among them, metal-nanoparticle-based carrier is considered as the most versatile and efficient.



### 3.2 Advantages of Gold Nanoparticle based Gene Delivery

The benefits of gold nanoparticle for gene delivery system are summarized as: 1) various, selective and efficient conjugation methods for biomolecules on metal nanoparticle[11] 2) highly localized ion concentration around gold nanoparticle protecting genes from degradation[12, 13] 3) convenient multiplex loading of various drugs including targeting agents[14] 4) controllability of cellular uptake and circulatory period[15-17] 4) remote optical triggering for drug activation[18-20] 5) capability in plasmonic sensing applications[21-23]. These characteristics are from material properties, nanoscale particle, various size and shape, and plasmonic characteristics of nanoscale optics. For the remote optical triggering, a light of not interfering with cellular biomolecules can effectively provide a signal to release/activate genes from nanoparticle surface[18], therein accomplishing high temporal ( $< \text{sec}$ ) and spatial ( $< \mu\text{m}$ ) controllability of gene regulation (Fig 3.1A & B). So far, however, theoretical descriptions have been limited to ultrashort pulse laser excitation[24, 25], but the theoretical understanding of gene activation using common CW NIR lasers (i.e. laser pointer), which can expand diverse biological and medical applications, is in critical demand.

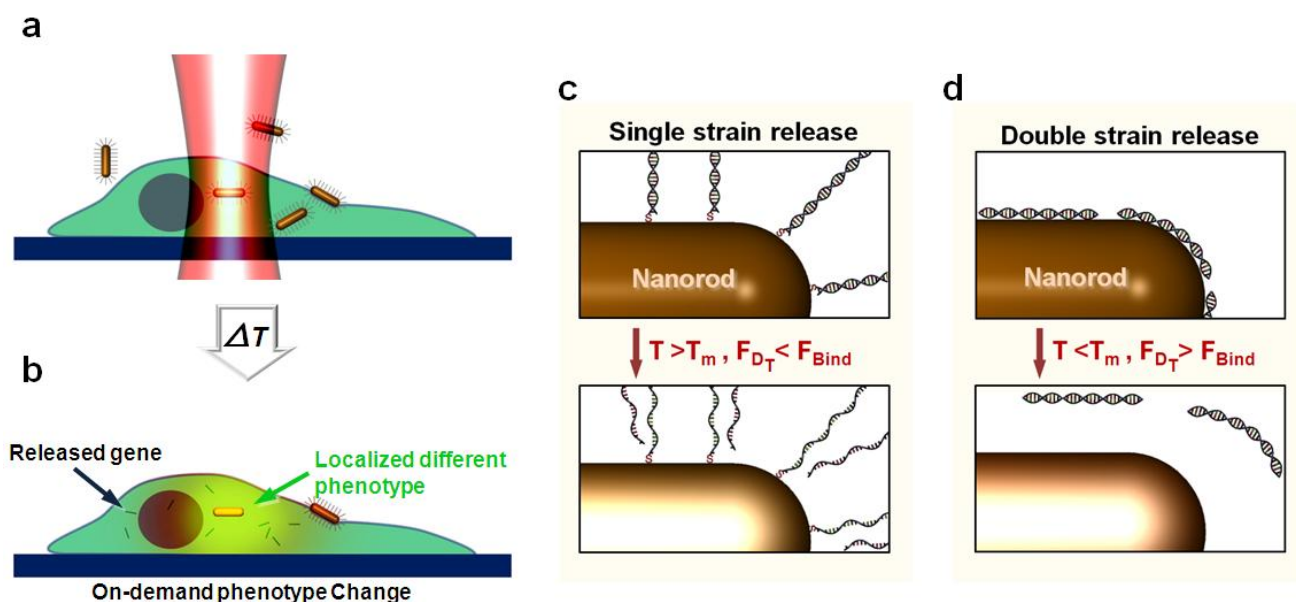


**Figure 3.1.** Scheme of molecular optogenetics and its relevant thermal profiles around excited nanorod. (A & B) internalized genes on nanorod is not activated before its detachment, but light excitation to nanorod release/activate genes to regulate gene expression. This method by light

excitation attains on-demand activation with high spatial and temporal resolution. (C & D) the combination of temperature and thermal gradient makes various gene activation scenarios by critical conditions of melting temperature and molecular binding force to nanorod.

Here, we suggest a mechanism derived from photothermal heat as a potential of releasing attached DNAs. If a time scale of interest is more than seconds, the photothermal effect is a dominant physics in the light-particle interaction. As studied in most literatures[24-26], a gold nanorod is chosen here as a representative nanometallic carrier. When a nanorod is excited by a resonant wavelength (see Supplementary Discussion), free electrons on metal are strongly oscillated in a group motion (this is dominantly distinguished from bulk metal structures). Then, two unique phenomena are followed around excited nanoparticles; locally enhanced optical field and highly generated resistive heat (Fig. 3.2).

### 3.3 Photothermal Heat from an Excited Nanorod

In the classic view of electromagnetics, two energies are expressed from electromagnetic field and particles interaction as shown in eq. 1.

$$\begin{aligned} P_{Total} = P_{radiative} + P_{resistive} &= \int_V \mathbf{H} \cdot \frac{\partial \mathbf{B}}{\partial t} dV + \int_V \mathbf{E} \cdot \frac{\partial \mathbf{D}}{\partial t} dV \\ &= \oint_S (\mathbf{E} \times \mathbf{H}) \cdot \mathbf{n} dS + \int_V \mathbf{J} \cdot \mathbf{E} dV \end{aligned} \quad \text{eq. 1}$$

Here  $\mathbf{H}$  is magnetic field,  $\mathbf{B}$  is magnetic flux,  $\mathbf{E}$  is electric field,  $\mathbf{D}$  is electric displacement, and  $\mathbf{J}$  is current density. Among plasmonic applications, the first energy term ( $P_{radiative}$ ) is critical for most sensing applications due to its optical field dependency, and the second term is a critical physics for photothermal applications including cancer therapy[27, 28] and also this optogenesis application. By combining heat transfer through convection and conduction with the resistive heat generation in electromagnetics, thermal profiles in surrounding media can be attained (Fig. 3.2C to F). Vigorous motion of electron are mostly induced in the middle part of nanorod being expressed as localized heat generation in nanorod, but high conductivity of gold ( $k_{gold}=317 \text{ W/m} \cdot ^\circ\text{C}$ ) makes uniform temperature over the nanorod within a time scale of interest ( $\sim$ pico-second). In contrast, low conductivity of water ( $k_{water}=0.595 \text{ W/m} \cdot ^\circ\text{C}$ ) results in a localized high-temperature area in the media (i.e. water) around the nanorod. Here, we find a non-ignorable physics called *thermophoresis* commonly being paid

little attention to in a macroscale. As an example, the amplitude of gradient reach to more than  $1\text{E}9\text{ }^{\circ}\text{C}/\text{m}$  in a general experimental condition at the steady state (i.e. 20mW 785nm CW laser focused on a 5 $\mu\text{m}$  diameter, see a method in Supplementary Information).

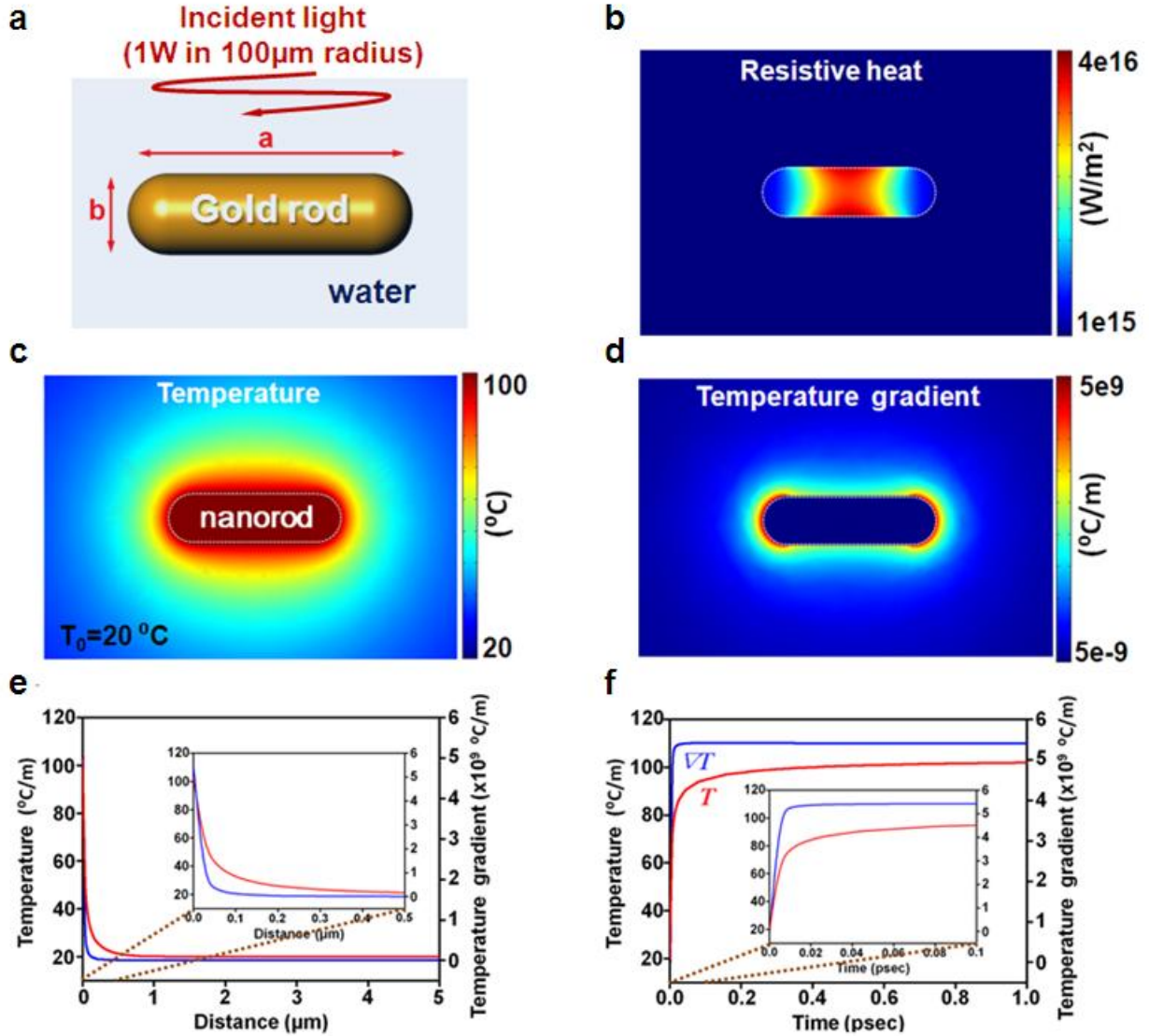


**Figure 3.2.** Thermal profiles of optically excited nanorod from multiphysics simulations. (A) A polarized incident light parallel to nanorod major axis can induce surface plasmon effectively and its resonant wavelength can be tunable depending on nanorod's aspect ratio. (B, C & D) Plasmonic excitation generates resistive heat inside nanorod, especially in the middle part, and makes a localized high temperature region near the nanorod, and therefore a big magnitude of thermal gradients. This result is from 20mW 785nm CW laser focused on a 5 $\mu\text{m}$  diameter spot. The nanorod dimension is (a,b)=(86nm, 25nm) which is commonly available for 780~785nm

excitation. (E & F) Spatial and temporal profile of temperature and thermal gradient on the nanorod.

Time resolvable study shows the temperature of nanorod reaches to the steady state (around 95 °C) within less than 1 pico-second[29] (Fig. 3.2F). Even in the steady state, high temperature is still spatially localized within 1- $\mu$ m distance from excited nanorod. Temperature gradient is much swiftly changed in time and space. It is noticeable that this result is under comparatively mild conditions without any short pulse laser excitation. This result confirms that the previous studies of on-demand optical activation by using continuous wave laser with milli-watt power could result in a fast triggering of molecular releasing [18, 20].

### 3.4 Gene Activation by Photothermal Physics

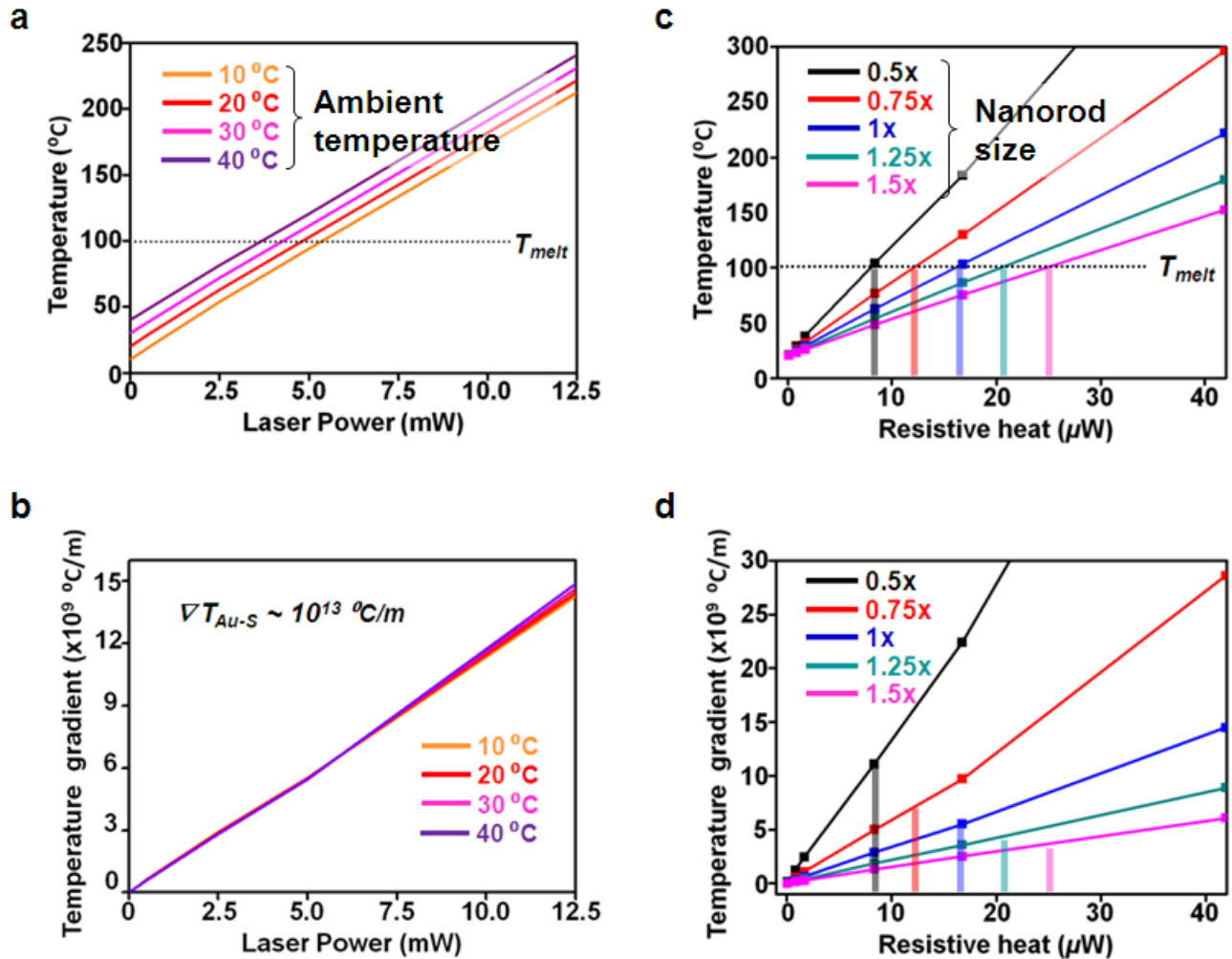


**Figure 3.3.** Modulation of thermal profiles from nanorod excitation. (A & B) Temperature and thermal gradient change linear to laser power. Temperature is superposed to ambient temperature with laser excitation but thermal gradient is not. For comparison, a melting temperature of two-order base-pair dsDNA and required thermal gradient to match gold-thiol binding force are shown in plots. (C & D) The change of nanorod size even with the same amount resistive heat generation results in a variety of thermal profiles. Smaller size can make higher temperature and bigger gradient. 1x indicates a nanorod size of (86nm, 25nm).

Now, a diversity of thermal response from nanorod-light interaction can be considered for various carrying and releasing scenarios (Fig. 3.1C & D). First, adjustment of laser power is one of ways controlling resistive heat amount (Fig. 3.3A and B). As the law of energy conservation, heat generation from an excited nanorod is linear to laser power within a certain range of laser power of not damaging nanostructure. As shown Fig. 3.3A, the temperature is linear to the power of laser, with being superposed to ambient temperature. Also, the magnitude of thermal gradient is linearly dependant to laser power, but not clearly related to ambient temperature (Fig. 3.3B). This trend will be explained in an analytical way later. If releasing mechanism be schemed as melting to release a single strain from thiolated cargo DNA (Fig. 3.1C), this requires the condition of  $T > T_{Melt}$  &  $F_{\nabla T} < F_{Bind}$  which is conveniently attainable in this scheme.

To compare the amount of  $F_{\nabla T}$  and  $F_{Bind}$ , a convenient index can be defined from forced diffusion equation.

$$J = J_{Conv} + J_{Diff} + J_{Forced} = (\mathbf{u} \cdot \mathbf{c}) + (-D \cdot \nabla c) + c \cdot (\boldsymbol{\mu} \cdot \mathbf{F}_{Bind} - D_T \cdot \nabla T) \quad \text{eq. 2}$$

Here,  $\mathbf{J}$  is total flux,  $\mathbf{J}_{Conv}$  is convection flux,  $\mathbf{J}_{Diff}$  is diffusion flux,  $\mathbf{J}_{Forced}$  is forced flux including binding force and thermophoresis. And  $\mathbf{u}$  is fluid velocity,  $\mathbf{c}$  is concentration,  $\mathbf{D}$  is diffusion coefficient,  $\boldsymbol{\mu}$  is mobility ( $\boldsymbol{\mu} = \mathbf{D}/kT$ ,  $k$  is Boltzmann constant),  $\mathbf{F}_{Bind}$  is binding force between nanorod and gene,  $\mathbf{D}_T$  is thermal diffusion coefficient and  $\mathbf{T}$  is temperature. During initiating gene detachment from nanorod, the first two term of  $\mathbf{J}_{Conv}$  and  $\mathbf{J}_{Diff}$  can be ignored, and  $\boldsymbol{\mu} \cdot \mathbf{F}_{Bind}$  and  $\mathbf{D}_T \cdot \nabla T$  can be compared. Now we get the index variable shown in eq. 3.

$$I_{sep} = \frac{D_T \cdot \nabla T}{\mu \cdot F_{Bind}} = \frac{D_T}{D} \cdot \frac{\nabla T \cdot T \cdot k}{F_{Bind}} \quad \text{eq.3}$$

In case of thiolated dsDNA delivery scheme,  $I_{sep}$  is about  $2\text{E-}4$  ( $\frac{D_T}{D}=0.01$  / $^{\circ}\text{C}$ [30],  $\nabla T=6\text{E}9$   $^{\circ}\text{C/m}$  at  $T=100$   $^{\circ}\text{C}$  and  $F_{Bind}=1.4\text{E-}9$  N[31]) and so the thiol binding on gold is strong enough to overcome thermophoretic force and to only release a single strain by melting.

Changing overall size of nanorod can be another way to vary thermal response. Now we can assume the amount of resistive heat from nanorods due to controllability of laser power to produce a certain amount as shown in Fig 3A. As shown in Fig. 3.3C & D, thermal profile can be more dynamic from changing the size along with resistive heat amount. Overall trend is that bigger nanorod requires more resistive heat generation to attain a certain temperature but generates less magnitude of thermal gradient. This result indicates that localization of heat generation is important factor to nanorod temperature and thermal gradient in media.

This trend is more directly elucidated by using an equivalent circuit concept as shown Fig. 3.4A, and a simplified calculation at a steady state can be derived by assuming the nanorod as an effective sphere. The radius of the effective sphere is calculated as an average of major ( $a$ ) and minor axis ( $b$ ). Then, thermal flux  $Q$  from sphere to media (where the temperature is  $T_{inf}$ ) is assumed to go through an equivalent thermal resistance of  $R$ . From the Fig. 3.4A, the relevant equation are summarized as eq. 4[32].

$$Q = \frac{(T_r - T_{inf})}{R}, R = \frac{1}{4\pi k r} \quad \text{eq. 4}$$

From eq. 4, temperature and thermal gradient at the interface of sphere and media is attained as eq. 5.

$$T_r|_{r=r_0} = T_{inf} + \frac{Q}{4\pi k r_0} \quad \text{eq. 5a}$$

$$\left. \frac{dT_r}{dr} \right|_{r=r_0} = f \cdot \left[ -\frac{Q}{4\pi k r_0^2} \right] \quad \text{eq. 5b}$$

Here,  $k$  is thermal conductivity of media ( $W/m \cdot ^\circ C$ ),  $r_0$  is the effective radius of the sphere ( $m$ ). In eq. 5b, non-uniform distribution of thermal gradient on nanorod surface (Fig. 3.2D) makes a necessity of an empirical geometry factor of  $f$  for  $\left[\frac{dT_r}{dr}\right]_{r=r_0}_{nanorod} = f \cdot \left[\frac{dT_r}{dr}\right]_{r=r_0}_{sphere}$ .

As discussed in supplementary information,  $f$  for this nanorod is 2. The eq. 5 provides clearer picture for  $Q$  and  $r_0$  (therefore providing nanorod size). As an example, one calculation result is shown in Fig. 3.4B, denoting  $T_{critical}$  is a melting temperature for 2-order base-pair ddDNA (here,  $80^\circ C$ ) and  $\nabla T_{critical}$  aim a thermophoretic force to match an electrostatic force which is 4 order less than Au-S binding force (here  $3 \times 10^{-10} C/m$ ). From conditions of  $T = T_{critical}$  and  $\nabla T = \nabla T_{critical}$ , the four regions are distinguished as shown in Fig. 3.4B, which are  $X$ =(no melt, detach),  $Y$ =(no melt, no detach),  $Z$ =(melt, no detach),  $W$ =(melt, detach). From this plot, a critical dimension of nanorod of which  $r_{eff}$  is equal to 30 nm is found, and therefore nanorod axis ( $a, b$ ) is (46 nm, 14 nm) (Fig. 3. 4C).

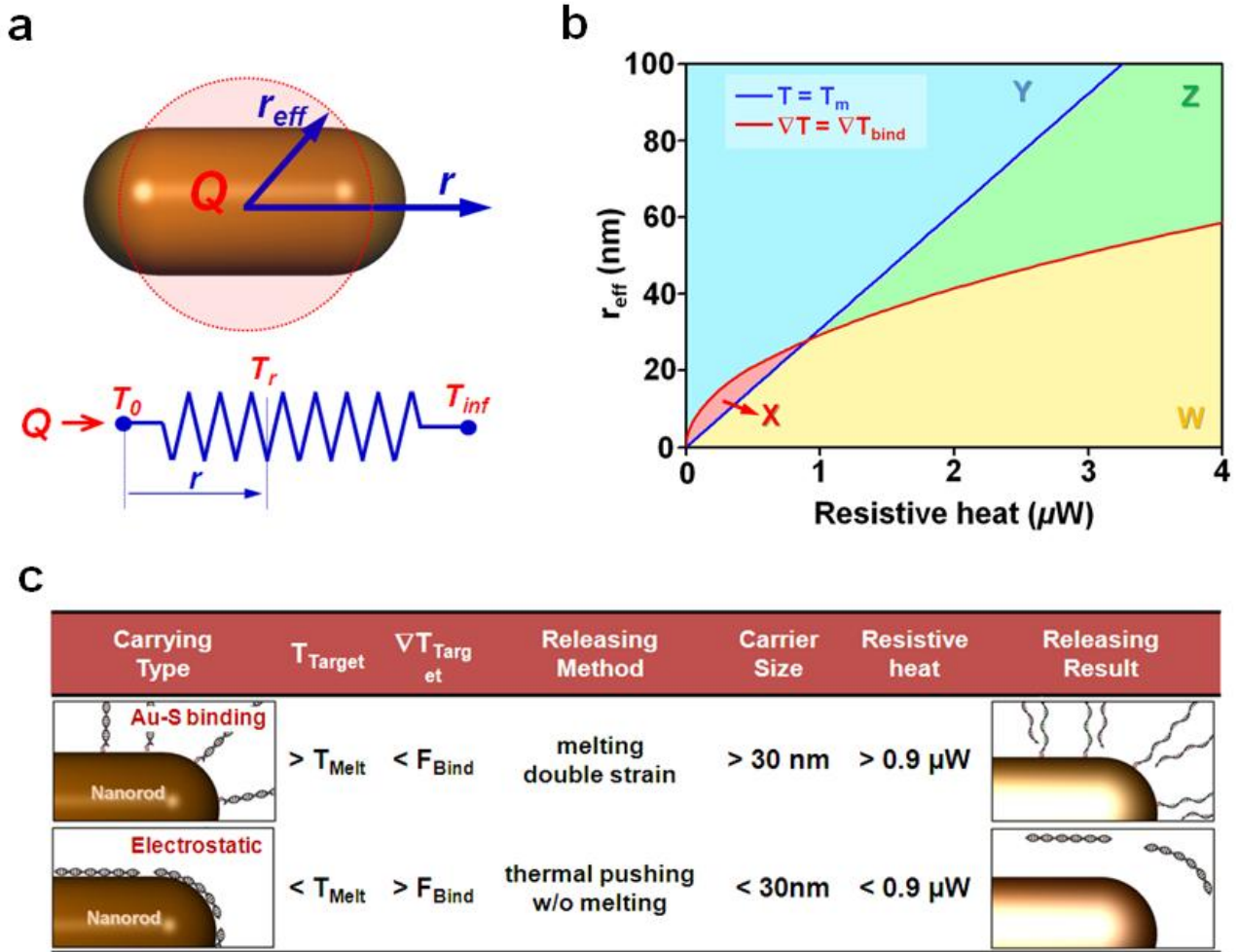


**Figure 3.4** Equivalent thermo-circuit model and its analytical calculations. (A) By defining an effective radius of sphere for the nanorod, thermal response of temperature and its gradient can be simplified as an equivalent circuit and be calculated as shown eq. 5. The effective radius is an average of major and minor axis of nanorod. (B) Two conditions of  $T=T_m$  and  $\Delta T=\Delta T_{bind}$  can guide to find required size of nanorod and resistive heat. Here,  $T_m=80\text{ }^{\circ}\text{C}$  and  $\Delta T_{bind}=3\text{ }10^{10}\text{ }^{\circ}\text{C/m}$ . (C) For the scenarios shown in Fig. 1c, resistive heat and equivalent radius are summarized from the eq. 5 calculation. Here electrostatic binding force is assumed 4 order smaller than gold-thiol binding force.

### 3.5 Conclusion

In this study, thermophysics of excited metal nanoparticle (i.e. nanorod) was discussed in the view of the *optogenetics* application. The resistive heat from plasmonic resonance can generate thermophoretic force comparable to electrostatic binding, and localized high-temperature field to melt dsDNA on a nanorod, therefore capable of various delivery/activation scenarios. This discussion together with the equivalent thermo-circuit model can guide in choice of metal nanoparticle and resistive heat amount, and furthermore is applicable to various nanoscale thermophysics of biophotonics, nanoelectronics, plasmonic sensor, nanofluidics and energy nanotechnology.

### Reference

- [1] M. T. McManus and P. A. Sharp, "Gene silencing in mammals by small interfering RNAs," *Nature Reviews Genetics*, vol. 3, pp. 737-747, Oct 2002.
- [2] K. Berns, *et al.*, "A large-scale RNAi screen in human cells identifies new components of the p53 pathway," *Nature*, vol. 428, pp. 431-437, Mar 25 2004.
- [3] P. J. Green, *et al.*, "The Role of Antisense Rna in Gene-Regulation," *Annual Review of Biochemistry*, vol. 55, pp. 569-597, 1986.
- [4] M. Cavazzana-Calvo, *et al.*, "Gene therapy of human severe combined immunodeficiency (SCID)-X1 disease," *Blood*, vol. 96, pp. 590A+, Nov 16 2000.
- [5] M. H. Tuszynski, *et al.*, "A phase 1 clinical trial of nerve growth factor gene therapy for Alzheimer disease," *Nature Medicine*, vol. 11, pp. 551-555, May 2005.
- [6] Y. Isaka, *et al.*, "Gene therapy by skeletal muscle expression of decorin prevents fibrotic disease in rat kidney," *Nature Medicine*, vol. 2, pp. 418-423, Apr 1996.
- [7] D. W. Pack, *et al.*, "Design and development of polymers for gene delivery," *Nature Reviews Drug Discovery*, vol. 4, pp. 581-593, Jul 2005.



- [8] M. X. Tang, *et al.*, "In vitro gene delivery by degraded polyamidoamine dendrimers," *Bioconjugate Chemistry*, vol. 7, pp. 703-714, Nov-Dec 1996.
- [9] J. H. Felgner, *et al.*, "Enhanced Gene Delivery and Mechanism Studies with a Novel Series of Cationic Lipid Formulations," *Journal of Biological Chemistry*, vol. 269, pp. 2550-2561, Jan 28 1994.
- [10] A. Bianco, *et al.*, "Applications of carbon nanotubes in drug delivery," *Current Opinion in Chemical Biology*, vol. 9, pp. 674-679, Dec 2005.
- [11] M. C. Daniel and D. Astruc, "Gold nanoparticles: Assembly, supramolecular chemistry, quantum-size-related properties, and applications toward biology, catalysis, and nanotechnology," *Chemical Reviews*, vol. 104, pp. 293-346, Jan 2004.
- [12] G. Han, *et al.*, "Stability of gold nanoparticle-bound DNA toward biological, physical, and chemical agents," *Chemical Biology & Drug Design*, vol. 67, pp. 78-82, Jan 2006.
- [13] Y. Ren, *et al.*, "Charge Density and Molecular Weight of Polyphosphoramidate Gene Carrier Are Key Parameters Influencing Its DNA Compaction Ability and Transfection Efficiency," *Biomacromolecules*, Nov 10 2010.
- [14] A. K. Salem, *et al.*, "Multifunctional nanorods for gene delivery," *Nature Materials*, vol. 2, pp. 668-671, Oct 2003.
- [15] B. Kim, *et al.*, "Tuning payload delivery in tumour cylindroids using gold nanoparticles," *Nature Nanotechnology*, vol. 5, pp. 465-472, Jun 2010.
- [16] Y. Qiu, *et al.*, "Surface chemistry and aspect ratio mediated cellular uptake of Au nanorods," *Biomaterials*, vol. 31, pp. 7606-7619, Oct 2010.
- [17] B. D. Chithrani, *et al.*, "Determining the size and shape dependence of gold nanoparticle uptake into mammalian cells," *Nano Letters*, vol. 6, pp. 662-668, Apr 2006.
- [18] S. E. Lee, *et al.*, "Remote Optical Switch for Localized and Selective Control of Gene Interference," *Nano Letters*, vol. 9, pp. 562-570, Feb 2009.
- [19] A. Wijaya, *et al.*, "Selective Release of Multiple DNA Oligonucleotides from Gold Nanorods," *Acs Nano*, vol. 3, pp. 80-86, Jan 2009.
- [20] A. Barhoumi, *et al.*, "Light-induced release of DNA from plasmon-resonant nanoparticles: Towards light-controlled gene therapy," *Chemical Physics Letters*, vol. 482, pp. 171-179, Nov 12 2009.
- [21] B. Nikoobakht and M. A. El-Sayed, "Surface-enhanced Raman scattering studies on aggregated gold nanorods," *Journal of Physical Chemistry A*, vol. 107, pp. 3372-3378, May 8 2003.
- [22] G. L. Liu, *et al.*, "Quantized plasmon quenching dips nanospectroscopy via plasmon resonance energy transfer," *Nature Methods*, vol. 4, pp. 1015-1017, Dec 2007.
- [23] G. L. Liu, *et al.*, "A nanoplasmonic molecular ruler for measuring nuclease activity and DNA footprinting," *Nature Nanotechnology*, vol. 1, pp. 47-52, Oct 2006.

- [24] P. K. Jain, *et al.*, "Ultrafast cooling of photoexcited electrons in gold nanoparticle-thiolated DNA conjugates involves the dissociation of the gold-thiol bond," *Journal of the American Chemical Society*, vol. 128, pp. 2426-2433, Feb 22 2006.
- [25] O. Ekici, *et al.*, "Thermal analysis of gold nanorods heated with femtosecond laser pulses," *Journal of Physics D-Applied Physics*, vol. 41, pp. -, Sep 21 2008.
- [26] S. Link, *et al.*, "Simulation of the optical absorption spectra of gold nanorods as a function of their aspect ratio and the effect of the medium dielectric constant," *Journal of Physical Chemistry B*, vol. 103, pp. 3073-3077, Apr 22 1999.
- [27] X. H. Huang, *et al.*, "Cancer cell imaging and photothermal therapy in the near-infrared region by using gold nanorods," *Journal of the American Chemical Society*, vol. 128, pp. 2115-2120, Feb 15 2006.
- [28] C. Loo, *et al.*, "Immunotargeted nanoshells for integrated cancer imaging and therapy," *Nano Letters*, vol. 5, pp. 709-711, Apr 2005.
- [29] This value can be physically different possibility due to time lapses from photon-phonon-electron energy transfer; but it still show the thermal response of nanorod is faster than interesting time range of seconds to hours.
- [30] C. B. Mast and D. Braun, "Thermal Trap for DNA Replication," *Physical Review Letters*, vol. 104, pp. -, May 7 2010.
- [31] M. Grandbois, *et al.*, "How strong is a covalent bond?," *Science*, vol. 283, pp. 1727-1730, Mar 12 1999.
- [32] F. P. Incropera and D. P. DeWitt, *Fundamentals of heat and mass transfer*, 4th ed. New York: Wiley, 1996.

# Chapter 4

## Depolarization of Plasmonic Scattering

Large optical cross-section and electron oscillation generate unique optical properties of metallic nanostructures. Locally amplified optical field is a representative characteristic enabling various applications including molecular imaging. However, considering light as 3-dimensional vector geometry can find other unique potential of metallic nanostructure. Depolarized scattering and curved Poynting vector are distinguishable optical geometric factors around optically excited metallic nanostructures. First, we demonstrate the effects of curved Poynting vector (or out-of-plane depolarization) on molecular scattering profile. It is known that molecular scattering has spectral variation along observation angles. Since resonating plasmonic nanoparticles can induce a curved Poynting vector, the spectral variation between presence and absence of plasmonic particles around fluorescence molecules should be similar to spectral variation between normal and oblique angle excitation. Experimentally and numerically we verified this spectral variation. Second, depolarized electric-field scattering is studied as a new molecular detection scheme. Even though the orthogonal component of electron motion to incident polarization usually happens as high-order poles and the electron motion is not much expressed as far-field scattering, far-field observers still observe a level of depolarization from metallic nanostructure scattering. Herein, we suggest a regular array of nanodisk to confine the depolarization scattering around the array plane and the usefulness of confined depolarization zone as a new molecular detection scheme. Thus, in addition to optical field amplification, 3-dimensional optical geometry will provide further flexibility and in-depth understanding in molecular detection.

### 4.1. Introduction

The light interaction with nanoscale metallic structures expresses distinctive physical phenomena from bulk structures [1, 2]. The uniqueness is mainly caused by nanoscale confinement of free electron motion. Since the nanoscale is smaller than or similar to the optical wavelength, resonant oscillation of free electron in a group motion results in strong scattering of light and photothermal heat generation. These two distinctive phenomena have been utilized for various applications such as molecular detection [3-5], plasmonic energy harvest [6], multiple harmonic generation [7], photothermal therapy [8] and optoelectronics [9, 10].

The listed applications are based mainly on the amount of absorbed light and a magnitude of scattered electric field or generated heat. Since electromagnetic wave (or

radiation) is three-dimensional comprising electric field, magnetic field and propagation vector, electromagnetic vectors can underpin other uniqueness or usefulness of plasmonic applications. Polarization can be one of representative examples as will be discussed here.

Since free electron movement is much larger than metal lattice size under an excitation of optical field, electron motion is strongly affected by boundary shape, therefore overall plasmonic response being related to boundary shape. It is a key difference from dielectric materials which has only parallel oscillation of electron to incident polarization. As shown in Fig. 5.1A, free electron motion is influenced by the combination of external electric field and boundary shape to suppress local charge inside metal. Thus, scattered field from the electron oscillation should include a certain amount of depolarization. Also if the depolarized scattering from objects propagates to a far field, the depolarization can be observed among plasmonic structure scattering, as several literatures discussed [11-14].

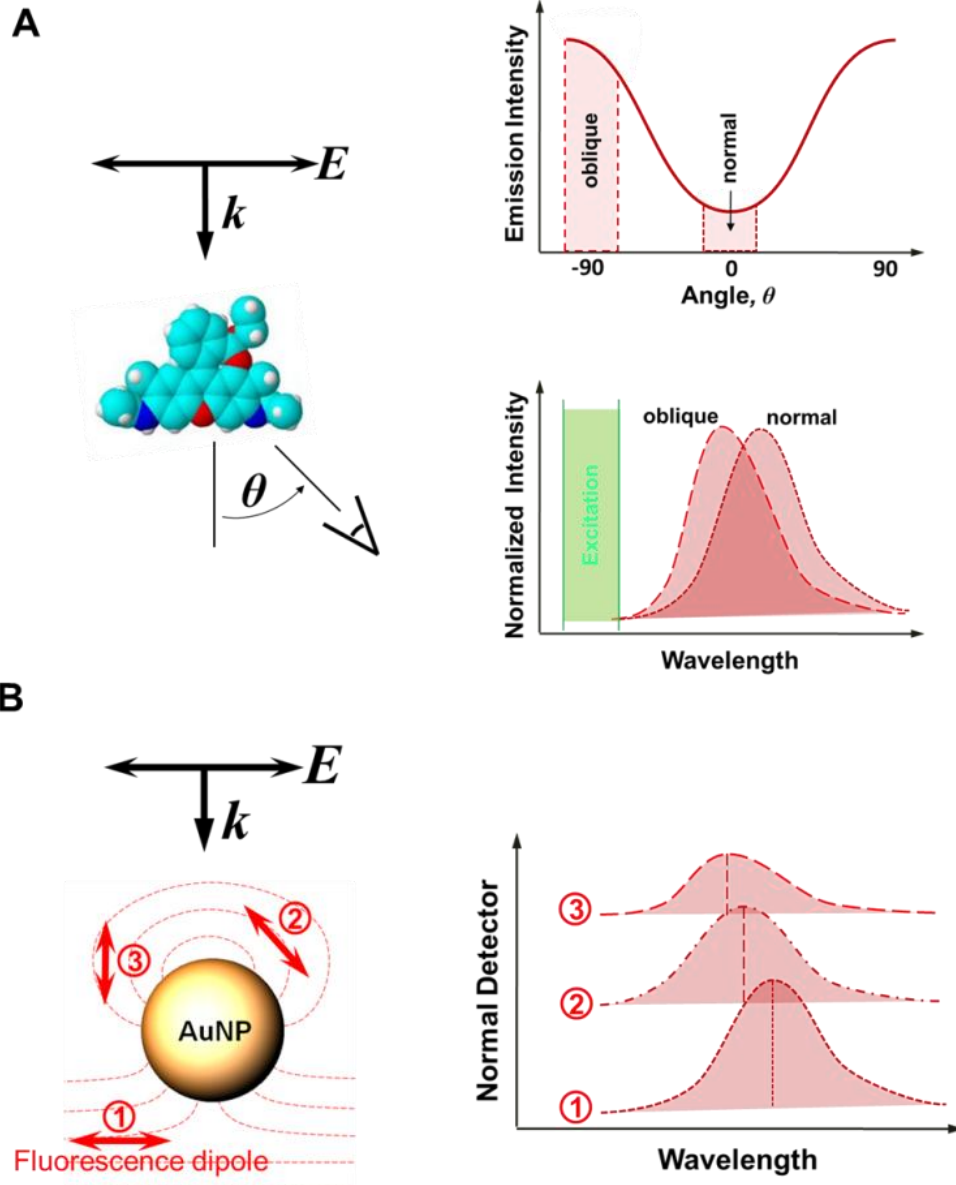


**Figure 4.1.** Angle-dependent molecular scattering and effects of plasmonic phenomenon. (A) Under a polarized excitation, molecular scattering can be various in terms of intensity and spectral profile along the angle of observation. (B) Angle-dependent spectral variation can be mimicked by the position of molecules regarding excited plasmonic structures.

## 4.2 Molecular Spectrum Variation around Excited Plasmonics

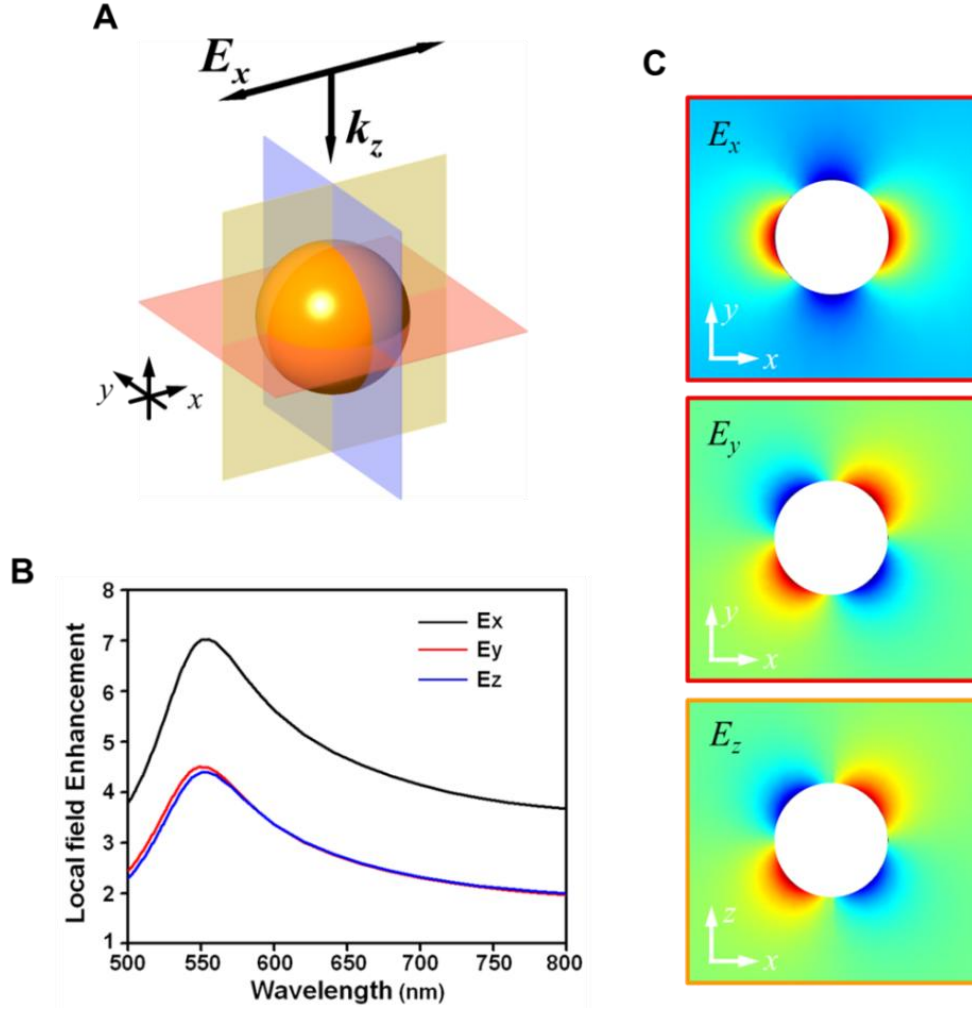
Mainly enhancement of molecular scattering by using optical field enhancement has been researched for fluorescence and Raman scattering [15-18]. At the same time, variation of spectral difference from enhanced molecular scattering has been also reported. While 2-digit information (i.e. resonance peak frequency, bandwidth and overall photon number) can still yield molecular structure information, the detail characterization in spectral profile can enrich fingerprint information showing molecular orientation, stretching, bending and rotation. The observed change of spectral profile in previous literatures can be supported by relative position of molecular position to amplified optical field vectors like electric field and Poynting vector. To study the effect of optical field generated by excited nanostructure on molecular scattering, a set of resonance-matching nanoparticle and fluorescence molecule is investigated here.

### 4.2.1 Spatial Pattern of Molecular Scattering Spectrum

Fig. 4.1A shows molecular scattering can be variable in different observation angles, which is caused by dipole-like emission pattern, multiple energy level, internal energy conversion, molecule rotational time, fluorescence life time and so on. Since dielectric media maintain optical field polarization along light pathway, molecules in a dielectric medium are excited as mostly being parallel to incident electric field, and therefore different angles of observation causes a change of scattering spectrum. This spectral variation can be mimicked in the comparison between presence and absence of metallic nanoparticles which have a frequency resonance to excite molecular scattering, since large optical cross-section of nanoparticles necessitates light to be focused and bent toward the nanoparticles, and molecular excitation non-parallel to incident electric field is around the nanoparticles (Fig. 4.1B).

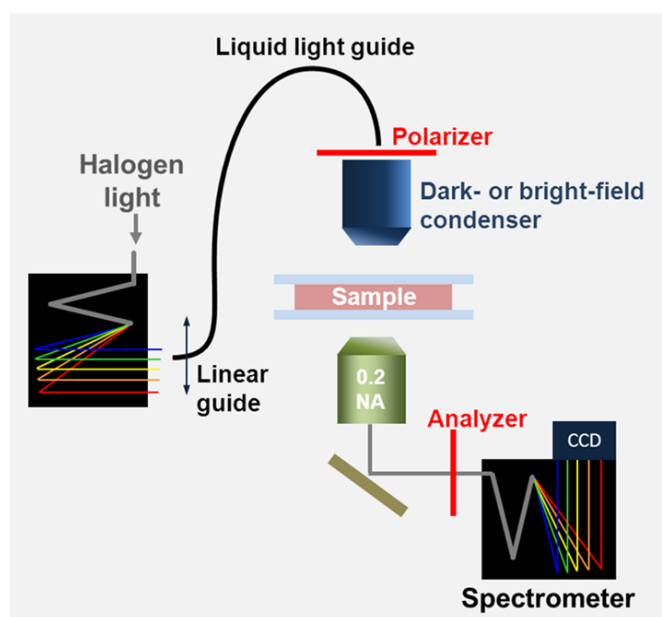
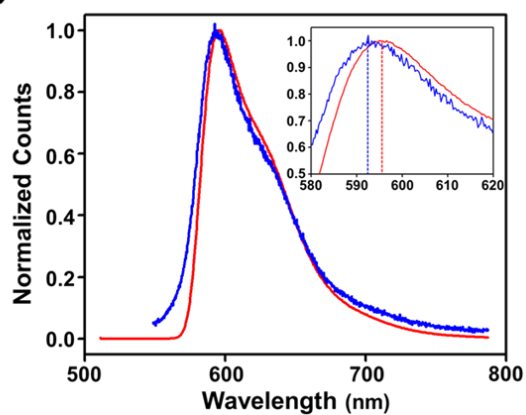
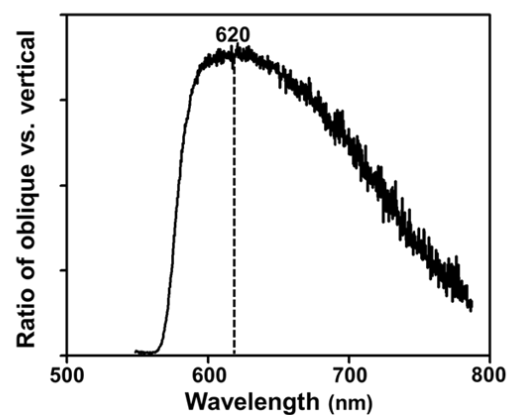
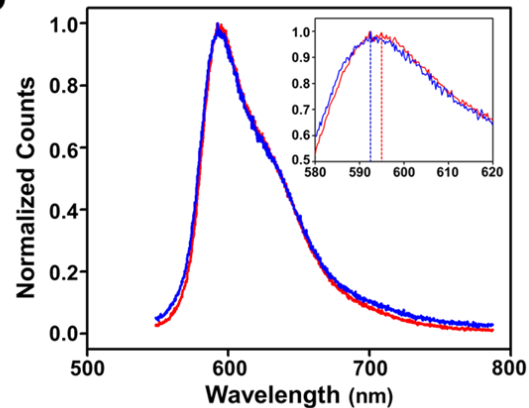
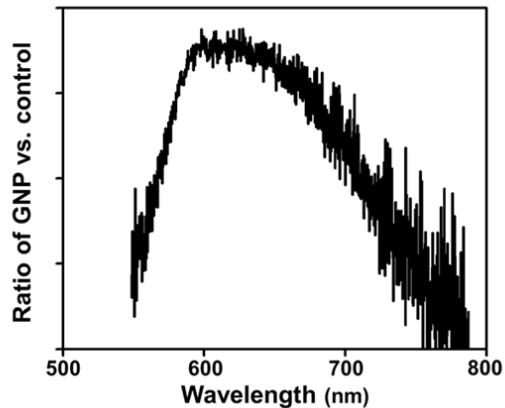
In this study, we used 50-nm gold nanosphere as metallic nanoparticle and rhodamine B as a molecular emitter, both of which have the similar wavelength of excitation resonance (540~550 nm). First, an optical field profile around nanostructure is calculated by electromagnetic simulation. A Drude-Lorentz dielectric function of gold is adopted from the previous literature [19]. The 50-nm gold nanoparticle in water ( $n=1.33$ ) shows 550-nm wavelength of resonance in near-field amplification being matched with extinction measurement of the used nanoparticle solution (data not shown here). As discussed upper, the gold nanoparticle can amplify an electric field parallel to incident electric field ( $E_x$ ) as well as non-parallel field of  $E_y$  and  $E_z$ . Since the magnitude of  $E_y$  and  $E_z$  reach to about 60%

magnitude of  $E_x$ , molecular scattering around the nanoparticle can be strongly affected by the non-parallel electric field. Interestingly, the parallel electric field,  $E_x$  is formed as dipole shape while the non-parallel electric-fields,  $E_y$  and  $E_z$  are formed as quadrupole shape (Fig. 4.2C,D and E). In the later part of this study, the quadrupole effect will be discussed.



**Figure 4.2.** Simulation of gold nanosphere for depolarized scattering. (A) A defined optical geometry and 50-nm gold nanosphere. (B) Electric-field spectra show similar magnitude of depolarized fields. (C) Dipole-like scattering of  $E_x$  and quadrupole-like scattering of  $E_y$  and  $E_z$  are observed around the resonated gold nanosphere.

#### 4.2.2 Plasmonic-induced Variation of Molecular Scattering Spectrum

**A****B****C****D****E**

**Figure 4.3.** Measurement of angle-dependent scattering and GNP-induced spectral variation (A) The experimental setup. By using two gratings, input and output wavelengths were characterized. (B & C) Angle-dependent scattering change. The blue line is a normal direction scattering, the red line is oblique angle scattering (70~80°), and the black line is normalized oblique angle scattering to normal direction scattering. (D & E) GNP influence in molecular scattering. The blue line is without-GNP, the red line is with-GNP and the black is normalized with-GNP scattering to without-GNP. These measurements were normal excitation and normal detection.

Then a fluorescence molecule, rhodamine B was analyzed for the spectral variation along observation angle by using the optical setup shown in Fig. 4.3A. Instead of laser source for excitation, a grating set of spectrometer was used to extract a narrow band of target wavelength from white light source (halogen bulb). The change of angle between excitation and observation by using bright- and dark-field condenser lenses resulted in a variation of emission spectrum; and the oblique angle showed to generate enhanced emission at 620 nm as shown Fig. 4.3B and C. As hypothesized, the presence and absence of gold nanoparticle in the rhodamine B solution should be able to generate the similar spectral variation without changing excitation angle. The applied nanoparticle concentration was  $2 \times 10^{10}$  particles/ml, where the whole GNPs take ignorable portion of total volume (total GNP volume versus water  $\sim 10^{-6}$ ). And in the rhodamine B solution, the gold nanoparticles were stable and not aggregated during the experiments less than 1 hour. The normal direction excitation on with-GNP and without-GNP rhodamine B solutions showed the same variation of emission spectrum as shown in Fig 4.3D and E. The comparison of the two different measurement shows that the presence of GNPs in solution results in z-component scattering shown in Fig 4.1.

### 4.2.3 Emitting Pattern Change around Nanoparticle

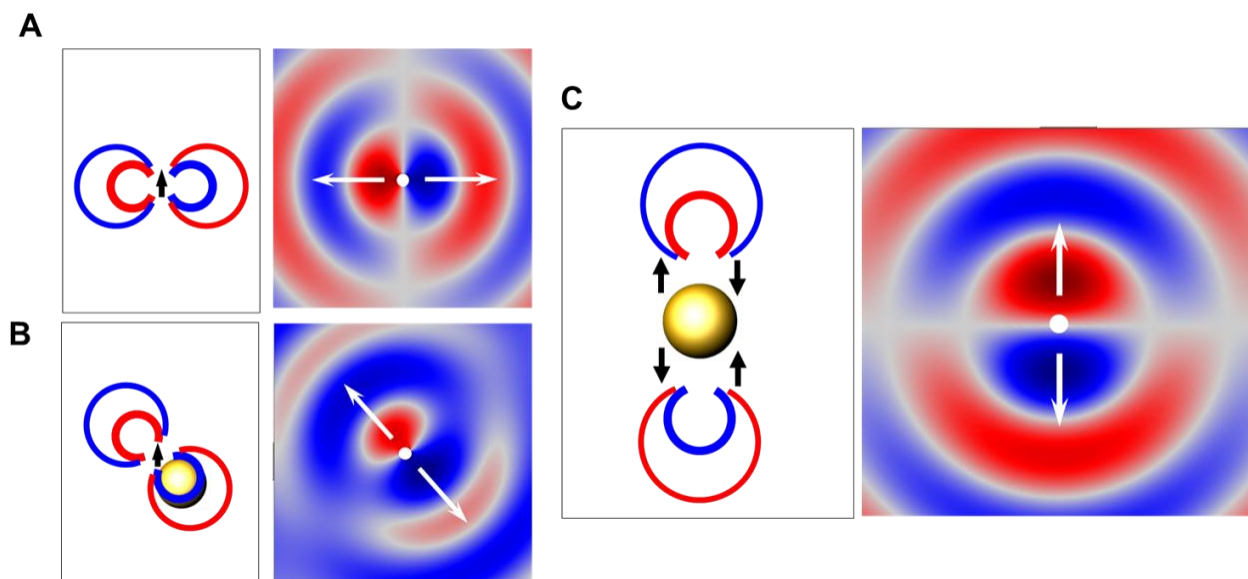




**Figure 4.4.** Scattering spatial pattern change near gold nanosphere. (A) A defined emitter scattering shows main scattering happens normal to dipole direction. (B) A single dipole-like emitter near to gold nanosphere change its scattering patterns with function of position. (C) Quadrupole-like positioning four emitters bring the scattering patterns to parallel to dipole direction.

Even the volume fraction of GNPs is as small as  $10^{-6}$ , the z-component scattering was clearly observed, which is assessed due to the change of scattering patterns around GNPs. When the molecular emitters are close to metallic nanostructure, it has been discovered that the emission patterns can be strongly affected based on distance between molecules and nanostructure [1]. Intact z-dipole scattering mainly propagates to xy-plane; therefore not clearly being observed z-axis aligned light-sample-objective configuration (Fig. 4.4A). Assumed that a molecular emitter is excited along the z axis in the area of enhanced  $E_z$  of Fig. 4.2E, the close distance to GNP results in strongly affected scattering pattern. Fig. 4.4B shows z-dipole scattering pattern around GNP at the wavelength of 570nm which is rhodamine B emission peak, and the pattern of z-dipole is similar in the range of rhodamine B emission (550 ~ 700 nm). Since the concentration of rhodamine B is high concentration, the molecular distribution can be assumed to be uniformly distributed around GNP. As shown in Fig. 4.2E,  $E_z$  forms as a quadrupole pattern which has  $\pi$ -phase difference between each pole. Correlated z-dipole excitation to GNP's  $E_z$  phase distribution, interestingly, changes the scattering pattern along z axis, which can make a clear observation in the z-axis aligned light-sample-objective configuration. Based on this numerical calculation results, we can understand that the clearly distinguishable spectral variation between the with-GNP and without-GNP cases.

### 4.3 Confinement of Depolarized Scattering and its Applications

The shape of boundary is an effective way to modulate depolarization properties such as the depolarization amount and far-field propagation. In this study, the symmetry of 2-D boundary is mainly discussed to present a distinctive example for depolarization study. The symmetric boundary causes a clear quadrupole pattern in orthogonal electron motion (OEM), which consequently generates orthogonal electric field around the nanodisk. Even with the  $\pi$ -phase difference between each pole, the scattering from OEM cannot be suppressed completely due to the physical distance between each pole. Thus a certain amount of depolarized scattering propagates to far field as shown in Fig. 4.5B.

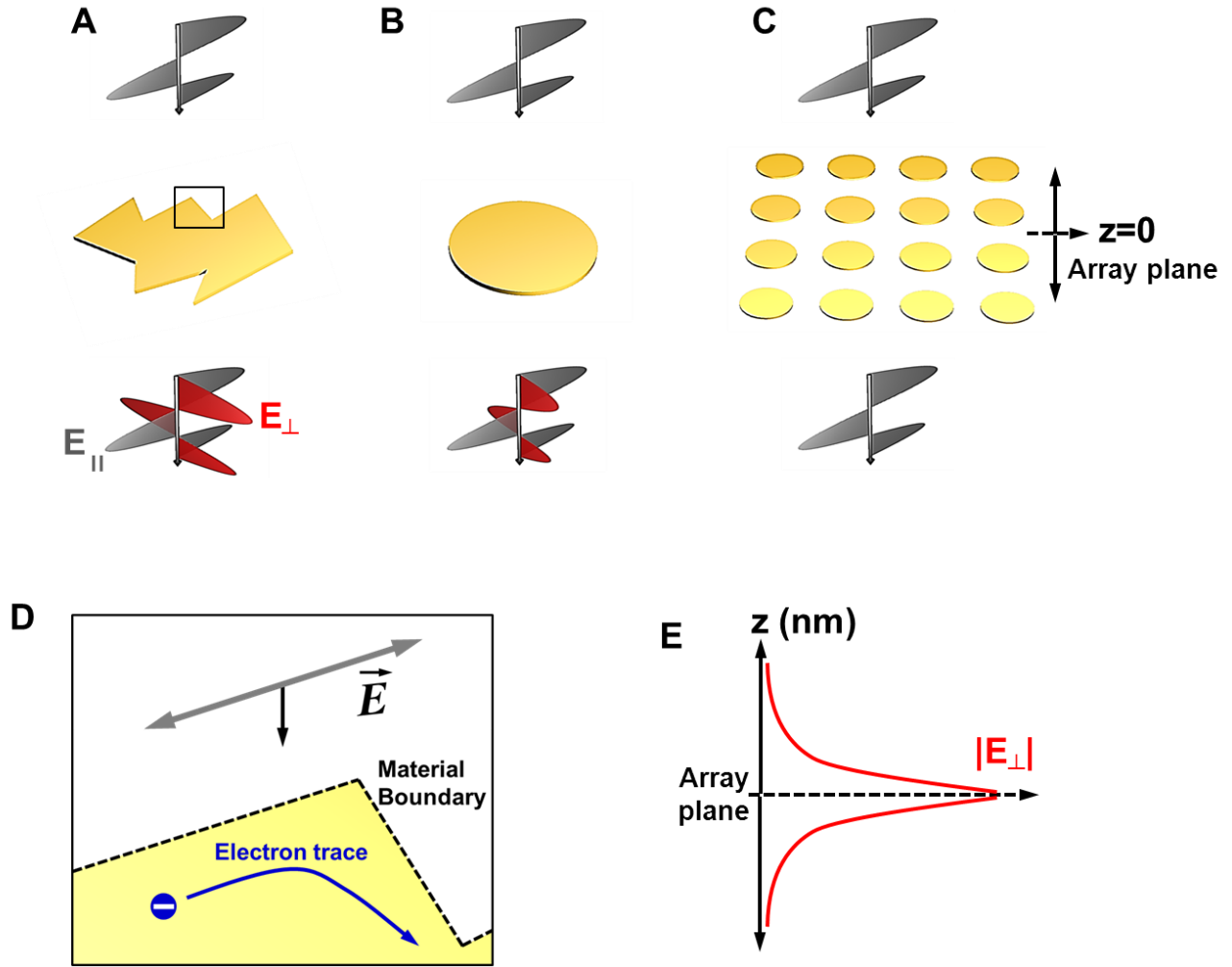


**Figure 4.5.** Depolarized scattering from various nanostructures. (A) A random geometry can induce a large depolarization ratio; (B) while 2-dimensional symmetric nanodisk suppresses the depolarization scattering. (C) An array of nanodisk can only transfer the same polarization scattering to a far field by completely suppressing the depolarization scattering. (D) The physical reason of depolarization scattering is electron oscillation happens at a similar range to nanostructure dimension under optical field excitation. (E) In case of nanodisk array, the orthogonal electric field is confined around array plane like evanescent wave of total internal reflection.

#### 4.3.1 Depolarized Scattering from 2-dimensional Metallic Nanostructure

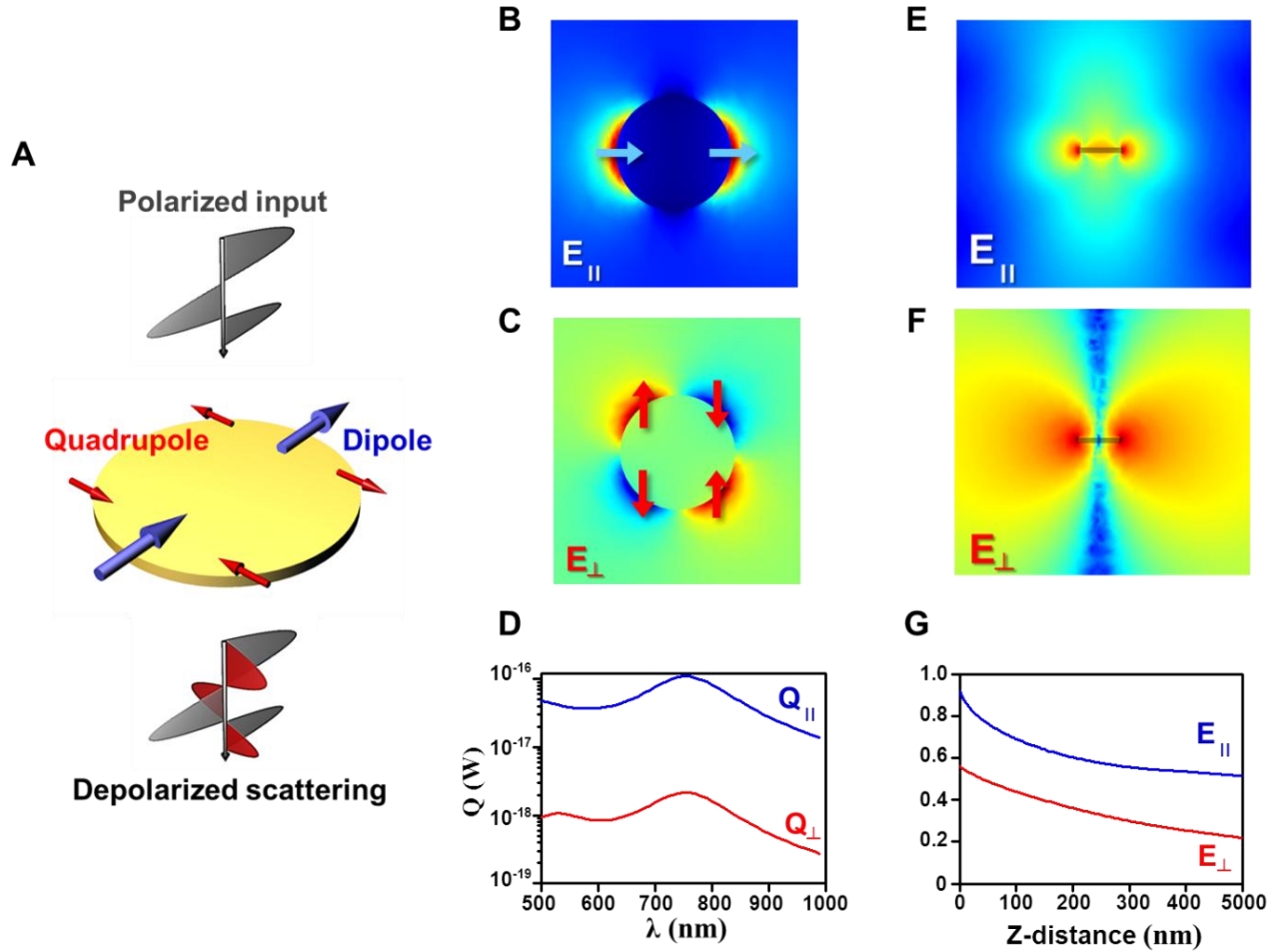


**Figure 4.6.** Depolarized scattering from a single nanodisk. The studied nanodisk is 100-nm diameter and 20-nm thickness, and its material is supposed as gold. (A) A polarized electric field excitation causes dipole-like parallel electron motion and quadrupole-like orthogonal electron motion in the disk. Even with quadrupole-like oscillation, the distance between each pole cannot suppress depolarized scattering to far field completely. (B) Parallel electric field forms as dipole pattern around the nanodisk, while (C) orthogonal electric field forms as a quadrupole of  $\pi$ -phase shift between each pole. (D) Generated photothermal heat is calculated separately regarding parallel electron motion and orthogonal electron motion. (E)  $E_{||}$  shows propagation like typical dipole scattering of plasmonic structure, while (F)  $E_{\perp}$  cannot be suppressed completely due to the distance between each pole of  $E_{\perp}$  quadrupole. (G) The field intensity of  $E_{||}$  and  $E_{\perp}$  is compared by integration of each electric field over a 10 times bigger area along normal direction of nanodisk plane. The color maps of (B) and (C) are as linear, and one of (E) and (F) are plotted as log scale.

Since non-parallel electron motion cannot be avoided in 2-D or 3-D metallic nanostructures, a certain amount of depolarization scattering from metallic nanostructure always exist. However since depolarization scattering is confined around nanostructures, the

depolarization field can be useful like evanescent wave of total internal reflection. In this aspect, here, an array of nanodisk is suggested as an efficient way to confine depolarization field around the nanostructures and keep it from propagating to a far field as shown in Fig. 4.5C.

For a detail analysis of optically excited nanodisk, an electromagnetic simulation was applied for a single nanodisk surrounded by air ( $\epsilon=1$ ). Incident light propagate along the normal direction of the disk plane. As shown in Fig. 4.6A and B, two orthogonal electric fields being parallel and orthogonal to incident electric field are expressed around the nanodisk; and the parallel electric field (PEF) forms as dipole configuration while orthogonal electric field (OEF) forms as quadrupole. Similarly to dipole scattering pattern, PEF can propagate to a far field without loss and the scattering of PEF can be mainly observed. This is the reason why optically excited nanoparticles are sometime described as simple electric dipoles. In case of quadrupole of OEF, the field does not propagate due to the  $\pi$ -phase difference between each pole. Since each pole has a distance of nanostructure size, the quadrupole cannot completely cancel out to a far field, and propagates mainly along in-plane direction. As shown in Fig 4.6E, a detector positioning along the normal direction of the nanodisk plane attains the depolarized scattering unless the detection angle (i.e., numerical aperture, NA) is limited to a small number (in the simulated configuration, a bigger than 10-degree NA can detect depolarization scattering). The amount of PEM and OEM is quantitatively compared by calculating resistive heat amount. As shown in Fig. 4.6D, the orthogonal movement of electron is comparable to parallel one in a similar order; therefore the far-field scattering of PEF and OEF being also comparable to each other (Fig. 4.6E).

### 4.3.2 Suppressed Depolarized Scattering via Nanostructure Array

As mentioned, an array of identical dimension of nanodisk is adopted for suppression of far-field propagation (Fig 4.7A). Two nearby poles of OEF from neighboring disks interferes since those scattering direction is to each other. The inference among OEF poles results in exponential decay along the normal direction of nanodisk like evanescent wave (Fig 4.7B). In addition of complete suppression of depolarized field, the depolarization phenomena from nanodisk array has several interesting characteristics. The first characteristic is a concordance of wavelength spectrum of  $E_{\perp}$  and  $E_{\parallel}$ ; the second is the identical z-axis profile of  $E_{\perp}$  decay independent to wavelength; and the third is  $E_{\perp}$  resonance is related to dark scattering of  $E_{\parallel}$  to a far field.

The circular shape of the nanodisk can cause the similar ratio of PEM and OEM, since the size of nanodisk (100-nm diameter) is smaller than the wavelength of interest. Actually electron movement in the nanodisk is calculated to remain identical over the wavelength of interest. Yet, bigger dimension nanostructures can induce the disparity of PEM and OEM, which can augment OEM further with suppressed PEM for particular applications like metamaterials.

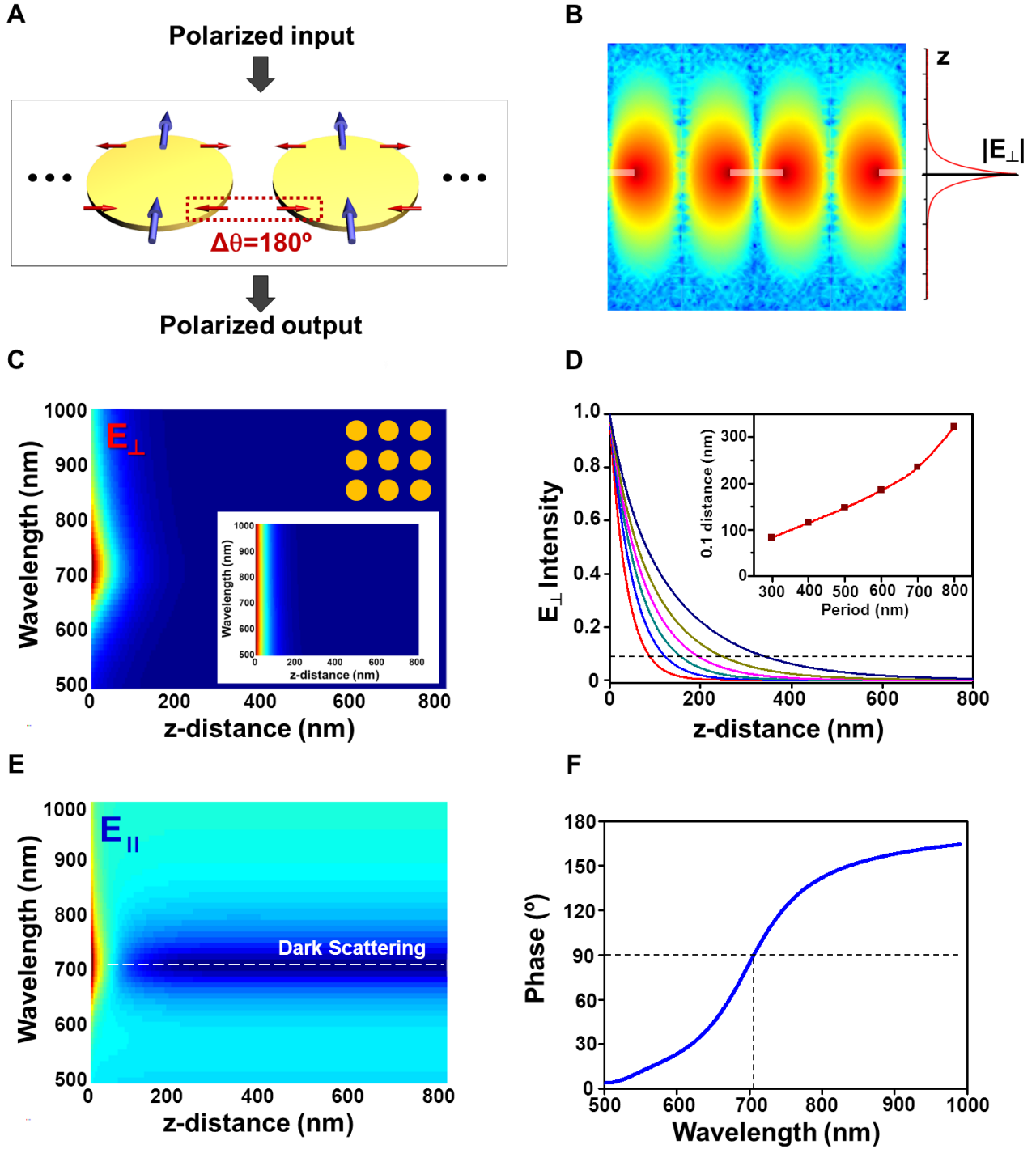


**Figure 4.7.** Depolarized scattering from a nanodisk array. (A) A schematic diagram shows how to complete suppression of  $E_\perp$  can be involved in an array form. (B) The calculated field intensity of  $E_\perp$  along a normal direction of plane, showing exponential decay like evanescent wave. The presented results in Fig. 4.7 are from a rectangular array of 100-nm diameter nanodisk and 400-nm periodicity, if not indicated further. (C) A color map of  $E_\perp$  about wavelength and  $z$ -

axis distance. The wavelength spectrum of  $E_{\perp}$  is identical to  $E_{\parallel}$  around the nanodisk plane, but  $E_{\perp}$  propagates to far field by having the same decay constant along  $z$  axis (inset color map) independently to wavelength. (D) The decay profile is determined only by the periodicity of nanodisk array, and a linear relation exists between the periodicity and decay constant. The curves from left to right indicate the cases of 300, 400, 500, 600, 700, 800 nm periodicity, respectively. (E) A color map of  $E_{\perp}$  about wavelength and  $z$ -axis distance shows a dark scattering existence at the resonance excitation. (F) Induced electric field phase at the center of nanodisk. The  $\pi/2$  phase retardation can be related to the resonance of  $E_{\perp}$  and dark field scattering of  $E_{\parallel}$ .

Differently from  $E_{\parallel}$  which should interact with incident electric field during propagation,  $E_{\perp}$  is radiated only from the nanodisk array. Thus, the spatial pattern of  $E_{\perp}$  is independent to the wavelength. Fig. 4.7C shows that the normalized  $E_{\perp}$  pattern over  $z$  axis is identical over the wavelength range. Now, the decay constant of  $E_{\perp}$  is expected only to be a function of periodicity of nanodisk array. The shorter distance between nanodisks confines  $E_{\perp}$  closer to the nanodisk array plane by following a linear trend (Fig. 4.7D). These 1<sup>st</sup> and 2<sup>nd</sup> characteristics can simplify the design of  $E_{\perp}$  field. Even though  $E_{\perp}$  does not propagate to far field, the measurement of  $E_{\parallel}$  can estimate the spectral profile of  $E_{\perp}$  and the periodicity of nanodisk array can determine spatial profile of  $E_{\perp}$  over the wavelength of interest.

The third characteristic of  $E_{\perp}$  is related to dark scattering which is currently discussed together with Fano resonance [20]. At a resonance wavelength (710 nm), the nanodisk array shows maximal expression of  $|E_{\parallel}|$  at the nanodisk array plane while  $|E_{\perp}|$  is minimal after a propagation along  $z$  axis at the resonance wavelength. Analytically the less propagation of  $E_{\parallel}$  is explained by 90° phase retardation of PEM in nanodisk, since incident magnetic field ( $H_0$ ) not changeable over the interaction with gold nanodisk ( $\mu=1$ ) and  $(E_{\parallel} \times H_0)$  does not propagate to far field due to the phase difference. Fig. 4.7F shows that 90° phase happens together with maximal phase change rate along wavelength, which we assess to be related to the spectrum of  $E_{\perp}$ .

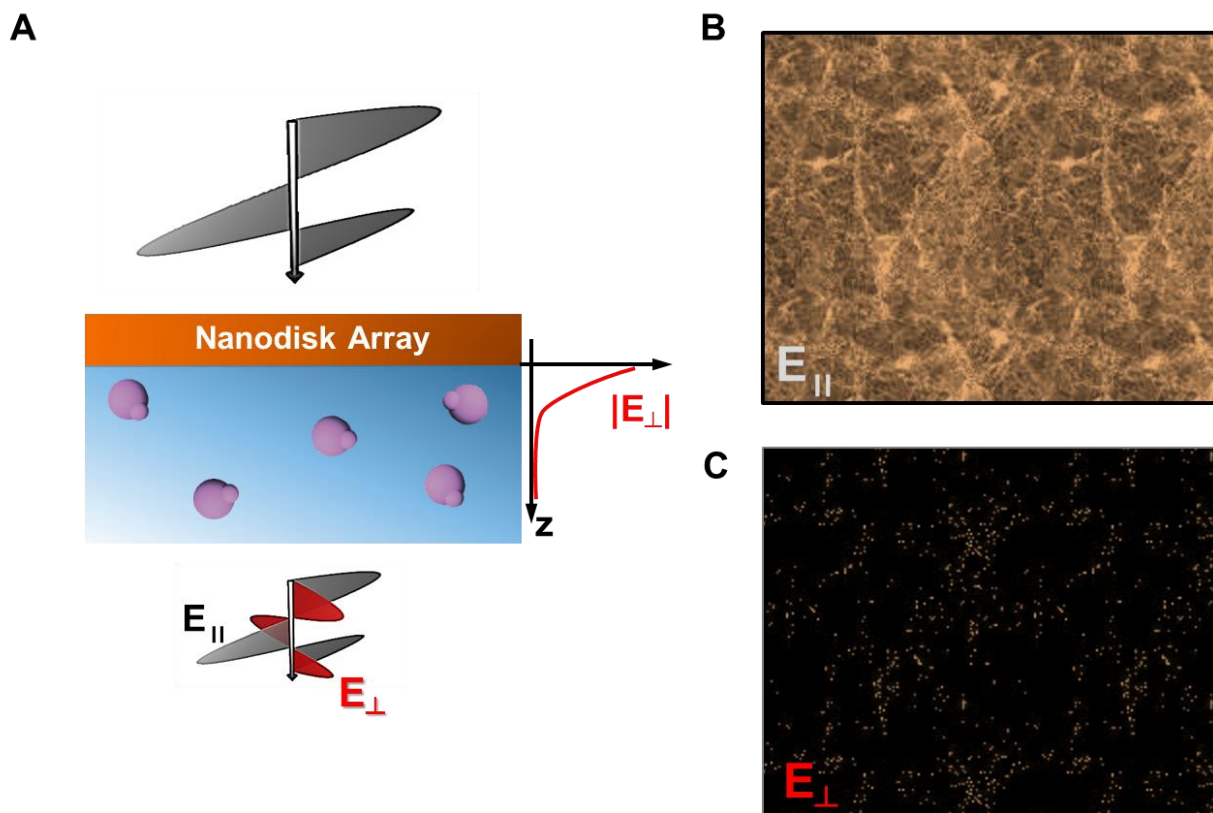


**Figure 4.8.** Localized depolarization application for molecular imaging. (A) A polarized light input can generate a confined depolarized scattering around the nanodisk array. By using two linear polarizers, the parallel polarization can be screened out, but only molecular scattering excited by depolarized field can be imaged. (B) and (C) are expected molecular imaging results by setting an analyzer parallel and cross to a polarizer. Images of (C) will be able to image molecules only nanoscale-distant from nanodisk array or furthermore calculate the distance of molecules from nanodisk array.

### 4.3.3 Localized Depolarized Scattering for Molecular Imaging

For the last century, surface-confined fields have been used for various molecular imaging methods. Total internal reflection fluorescence is a representative example. Likewise, the concept of confined depolarization zone can be also utilized as the same localized molecular imaging method. Since polarization information can be highly contrasted with a simple polarizer setup with a conventional optical microscope, it will be possible to map molecular distance from a certain nanostructure plane as shown in Fig. 4.8.

As a near future study, we suggest the combination with zero waveguide for molecular dynamic imaging methods similarly to currently highlighted DNA sequencing methods. In addition, metallic nanostructure can also involve highly enhanced optical field for various plasmonic molecular imaging methods such as surface-enhanced Raman

scattering; therefore this concept can expand to multiplex imaging methods as a simple optical setup in the future.

## 4.4 Conclusion

In sum, electron depolarization is always induced in case of 2-D or 3-D metallic nanostructures due to the electron oscillation over lattice. The orthogonal electric fields, in case of gold nanosphere, form as quadrupole pattern of  $\pi$ -phase difference. This phenomenon transforms a xy-plane emission pattern of a molecular emission to be along z axis. By using a resonance-matching molecule, rhodamine B, we demonstrate that the presence of GNPs in the solution enables to observe xy-plane scattering in the light pathway. The study of molecular emitter and nanostructure interaction is expected to advance various molecular imaging methods containing high spatial resolution as well as further enriched molecular fingerprint information.

In the second part, we discussed the characteristics of depolarization scattering and suggest how to modulate the depolarization scattering to far field. A 2-D array of nanodisk was shown to confine depolarization scattering around the array plane due to destructive interference of quadrupole-like scattering of  $E_{\perp}$ . This scheme can be utilized in various imaging methods similarly to evanescent wave of total internal reflection.

## Reference

- [1] V. Giannini, *et al.*, "Plasmonic Nanoantennas: Fundamentals and Their Use in Controlling the Radiative Properties of Nanoemitters," *Chemical Reviews*, vol. 111, pp. 3888-3912, Jun 2011.
- [2] N. J. Halas, *et al.*, "Plasmons in Strongly Coupled Metallic Nanostructures," *Chemical Reviews*, vol. 111, pp. 3913-3961, Jun 2011.
- [3] K. Kneipp, *et al.*, "Single molecule detection using surface-enhanced Raman scattering (SERS)," *Physical Review Letters*, vol. 78, pp. 1667-1670, Mar 3 1997.
- [4] G. L. Liu, *et al.*, "Quantized plasmon quenching dips nanospectroscopy via plasmon resonance energy transfer," *Nature Methods*, vol. 4, pp. 1015-1017, Dec 2007.
- [5] A. J. Haes, *et al.*, "Detection of a biomarker for Alzheimer's disease from synthetic and clinical samples using a nanoscale optical biosensor," *Journal of the American Chemical Society*, vol. 127, pp. 2264-2271, Feb 23 2005.
- [6] K. R. Catchpole and A. Polman, "Plasmonic solar cells," *Optics Express*, vol. 16, pp. 21793-21800, Dec 22 2008.



- [7] S. Kim, *et al.*, "High-harmonic generation by resonant plasmon field enhancement," *Nature*, vol. 453, pp. 757-760, Jun 5 2008.
- [8] X. H. Huang, *et al.*, "Plasmonic photothermal therapy (PPTT) using gold nanoparticles," *Lasers in Medical Science*, vol. 23, pp. 217-228, Jul 2008.
- [9] E. Ozbay, "Plasmonics: Merging photonics and electronics at nanoscale dimensions," *Science*, vol. 311, pp. 189-193, Jan 13 2006.
- [10] M. Salerno, *et al.*, "Plasmon polaritons in metal nanostructures: the optoelectronic route to nanotechnology," *Opto-Electronics Review*, vol. 10, pp. 217-224, Sep 2002.
- [11] M. Meier and A. Wokaun, "Enhanced Fields on Large Metal Particles - Dynamic Depolarization," *Optics Letters*, vol. 8, pp. 581-583, 1983.
- [12] N. Calander, *et al.*, "Interference of surface plasmon resonances causes enhanced depolarized light scattering from metal nanoparticles," *Chemical Physics Letters*, vol. 434, pp. 326-330, Feb 5 2007.
- [13] Z. Gryczynski, *et al.*, "Depolarized light scattering from silver nanoparticles," *Chemical Physics Letters*, vol. 421, pp. 189-192, Apr 3 2006.
- [14] K. Drozdowicz-Tomsia, *et al.*, "Depolarized light scattering from colloidal gold nanoparticles," *Chemical Physics Letters*, vol. 468, pp. 69-74, Jan 13 2009.
- [15] K. Kneipp, *et al.*, "Approach to Single-Molecule Detection Using Surface-Enhanced Resonance Raman-Scattering (Serrs) - a Study Using Rhodamine 6g on Colloidal Silver," *Applied Spectroscopy*, vol. 49, pp. 780-784, Jun 1995.
- [16] S. M. Nie and S. R. Emery, "Probing single molecules and single nanoparticles by surface-enhanced Raman scattering," *Science*, vol. 275, pp. 1102-1106, Feb 21 1997.
- [17] M. Moskovits, "Surface-Enhanced Spectroscopy," *Reviews of Modern Physics*, vol. 57, pp. 783-826, 1985.
- [18] J. R. Lakowicz, *et al.*, "Advances in surface-enhanced fluorescence," *Journal of Fluorescence*, vol. 14, pp. 425-441, Jul 2004.
- [19] P. G. Etchegoin, *et al.*, "An analytic model for the optical properties of gold," *Journal of Chemical Physics*, vol. 125, pp. -, Oct 28 2006.
- [20] B. Luk'yanchuk, *et al.*, "The Fano resonance in plasmonic nanostructures and metamaterials," *Nature Materials*, vol. 9, pp. 707-715, Sep 2010.

## Chapter 5

### Tunable Sensitivity of Plasmonic Nanoflake on Photonic Crystal

A well-designed metallic nanostructure interacts with light effectively as ‘surface plasmon polariton’, and expresses locally enhanced optical field useful for various applications including molecular fingerprint detection. Surface-enhanced Raman scattering (SERS) is a representative example whose sensitivity reaches down to a single-molecule level. The last-several-decade endeavor to accomplish the single-molecule sensitivity resulted in metallic nanostructure fabrications methods, from random aggregation to delicate top-down fabrication. The flexibility of molecular detection via plasmonics requires a plasmonic substrate design of performing frequency selectivity and detection sensitivity. In this respect, we investigated gold nanoflake structure on top of high dielectric photonic crystals. A controlled nucleation process on anodized aluminum oxide template resulted in a thin gold layer of having a great amount of nanogaps, which are expected to generate strong optical hot-spots. By fixing the thickness of gold layer but changing thickness of AAO, we can attain a large range of frequency resonance, exactly identical details of gold morphology, and no change of optical properties to environmental refractive index. The fabricated gold nanoflake successfully demonstrated a tunable sensitivity in single-molecule level detection: sub-femtomolar concentration of 1,2-bis(4-pyridyl)ethylene and an analytical enhancement factor up to  $10^{15}$  which is higher than what has been reported so far. We believe the gold nanoflake can be an ideal SERS substrate from a research level to a commercial product due to easy and uniform fabrication, well-developed fabrication process of AAO and structural stability of AAO over a long time.

#### 5.1 Introduction

Surface-enhanced Raman scattering is a promising molecular detection method by using plasmonic nanostructures. SERS can monitor molecular information as an in-situ and remote non-invasive manner, and when combined with a well-designed nanostructure, its detection limit can reach down to a single-molecule level [1-5]. Also, scattering contrast in frequency domain (called Stoke or anti-Stoke scattering) promises broad-range practicability due to recent realization of efficient but inexpensive optical filters. However, since current

light source of single wavelength (i.e. laser) do not cover a large range of wavelength, flexible selectivity of resonance wavelength is another criterion in plasmonic structure design.

Because a metallic nanostructure does not response uniformly to a broad range of wavelength due to its resonance complexly from its retardation and geometric effects [6], it is critical to match resonance wavelength to specific wavelength for applications. The wavelength tunability can accomplish with choices of metal types, environmental or supporting dielectric types and structural geometry. The order of metals - copper, aluminum, silver to gold redshifts; higher dielectric constant of surrounding material redshifts; bigger aspect ratio parallel to exciting electric field also redshifts resonance wavelength. Thus, the combined factors determines resonance wavelength, which makes plasmonic design more difficult.

For amplified Raman scattering, particular geometries are also required to focus optical response to a small volume as locally enhanced optical field. Since the optical field intensity on SERS substrate surface can increase Raman signal with nonlinear proportionality (commonly considered as being proportional as  $|E|^4$ , here  $E$  is electric field [7]), SERS signal intensity is highly dependent to the optical field enhancement. In previous literatures, a variety of geometrical design for sharp tips or close tip-to-tip distance has been characterized theoretically and experimentally [8-11], suggesting maximized enhancement usually possible in nanometer- or atomic-scale accuracy. A general approach to nanostructure geometry for optical field enhancement is sharp tips or close tip-to-tip distance where geometric resolution should be down to nanometer or atomic scale accuracy for maximized functions. However, since current nanofabrication of top-down methods is currently limited to a few nanometers to tens nanometers, randomly formed nanostructures yet containing geometric morphologies for optical field enhancement are still practically useful and function as excellent SERS substrates.

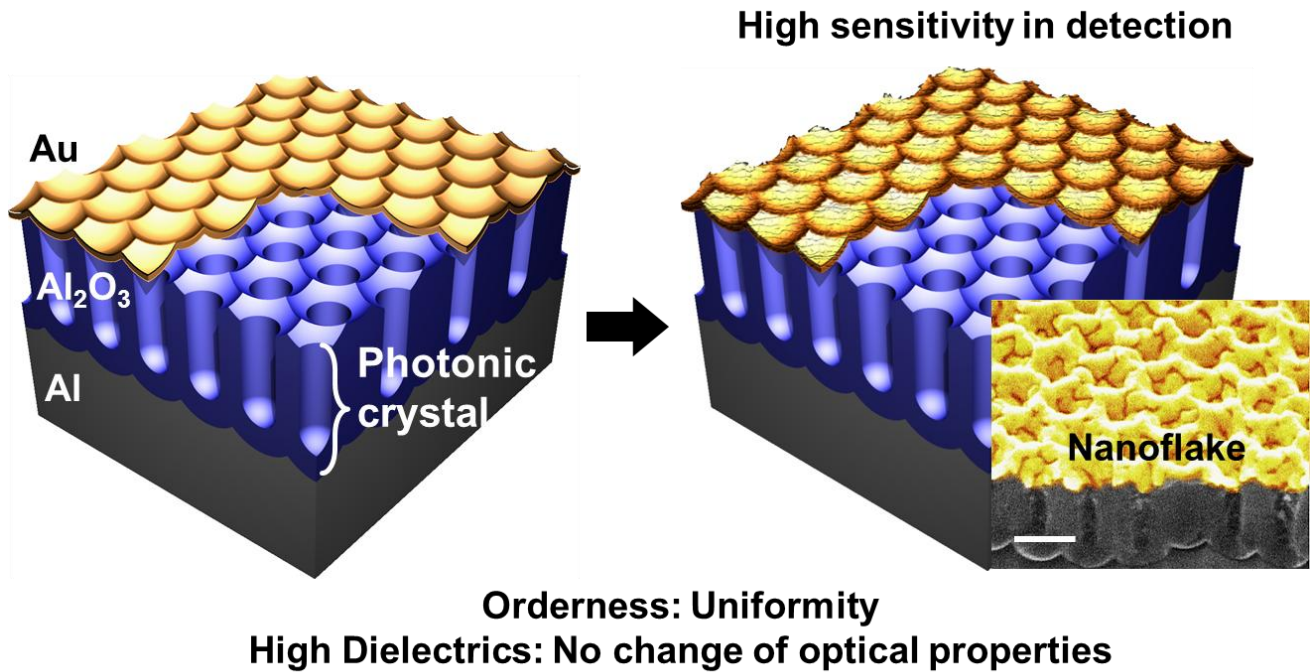


**Figure 5.1.** Design of nanoflake on photonic crystal. A combination of gold and AAO complex ( $\text{Al}_2\text{O}_3$  and aluminum) is useful to tune optical properties by changing the thickness of  $\text{Al}_2\text{O}_3$  and maintaining gold layer thickness. For enhanced optical hot-spot formation, a flake-like structure can be formed on the top of AAO complex, but the high dielectric property of AAO can maintain the overall optical properties (i.e., extinction) with the same thickness of smooth gold AAO.

## 5.2 Design of Nanoflake on Photonic Crystal

In any cases, nanoscale resolution in metallic structure, especially in top-down process, is usually not repeatable in changes of thickness, substrate or metal types. Strictly speaking, it is quite challenging to modulate wavelength selectivity and detection sensitivity together from a set of nanostructure fabrication especially to cover broad-range selectivity. In this aspect, geometry change of supporting dielectric structure can be the most reasonable way for this purpose, if resonance tuning ranges broadly. In this aspect, single-material photonic crystal enabling a broad range of optical response can be a candidate for supporting dielectric structure for metallic nanostructure.

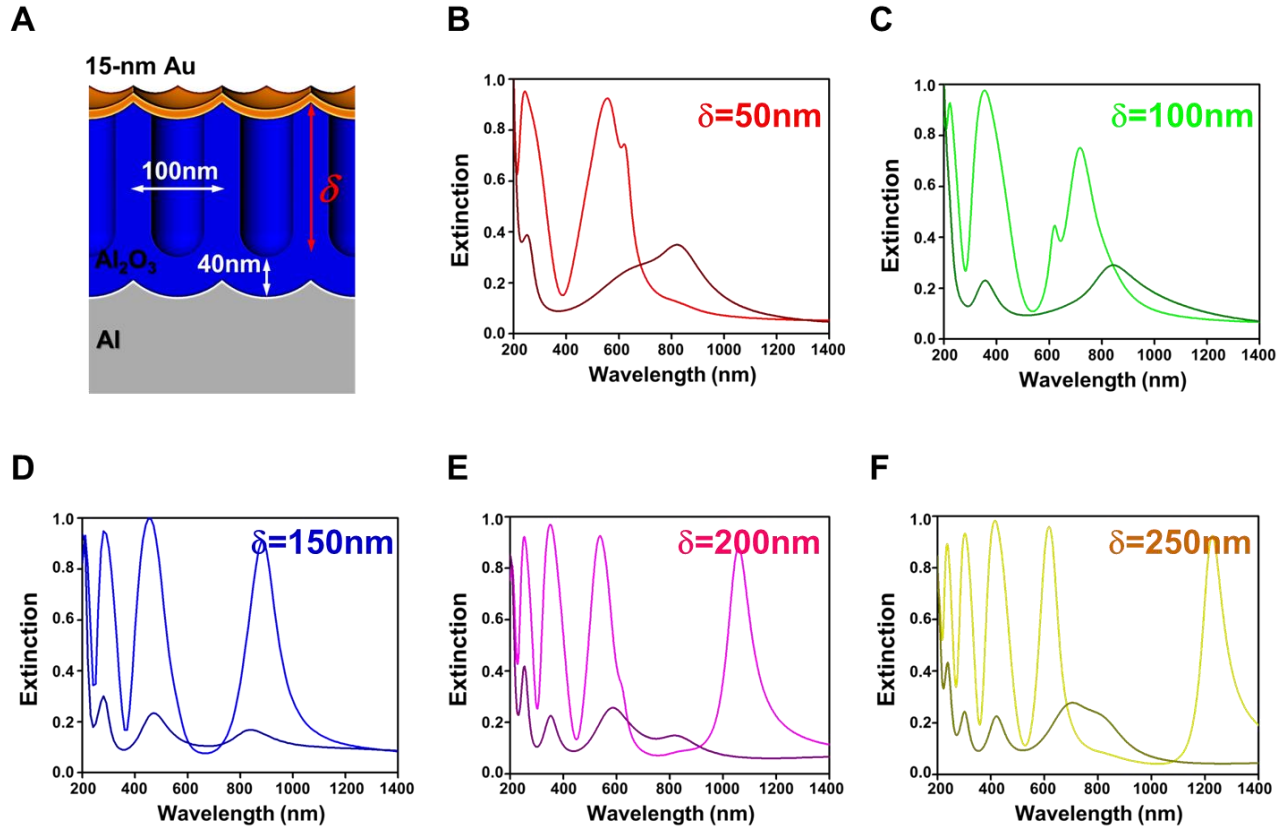


**Figure 5.2.** Simulated optical property (or extinction) of gold-coated AAO. (A) Configuration of the simulation structure. The gold-AAO consists of 15-nm gold layer thickness, thick aluminum supports, and various thicknesses of alumina layer. The periodicity of AAO is fixed to 100 nm since an adopted electrochemical process determines the periodicity regardless of AAO thickness. (B to F) AAO and gold-coated AAO optical properties for various gold thicknesses as noted in plots. The original optical property of AAO is shown to strongly affect the optical properties of gold-AAO.

As a photonic crystal platform, hexagonally arrayed nanohole pattern of anodized aluminum oxide (AAO) was used [12, 13]. From a prevalent fabrication method, AAO is realized as cylindrical hole array in aluminum oxide ( $\text{Al}_2\text{O}_3$ ) layer on nanoscale-rippled  $\text{Al}_2\text{O}_3$  and aluminum support. The periodicity and depth of nanohole can be modulated by electrochemical anodizing process (i.e. voltage, chemical and time) [14]. The AAO platforms used in this study have 100-nm periodicity and various depths ranged in 50 to 500 nm. The change of aluminum oxide layer thickness shows a clear modulation of AAO complex optical property (Fig. 5.2), and when it is combined with plasmonic structure on the top, optical properties of pure AAO complex is strongly deterministic to one of Au-coated complex.

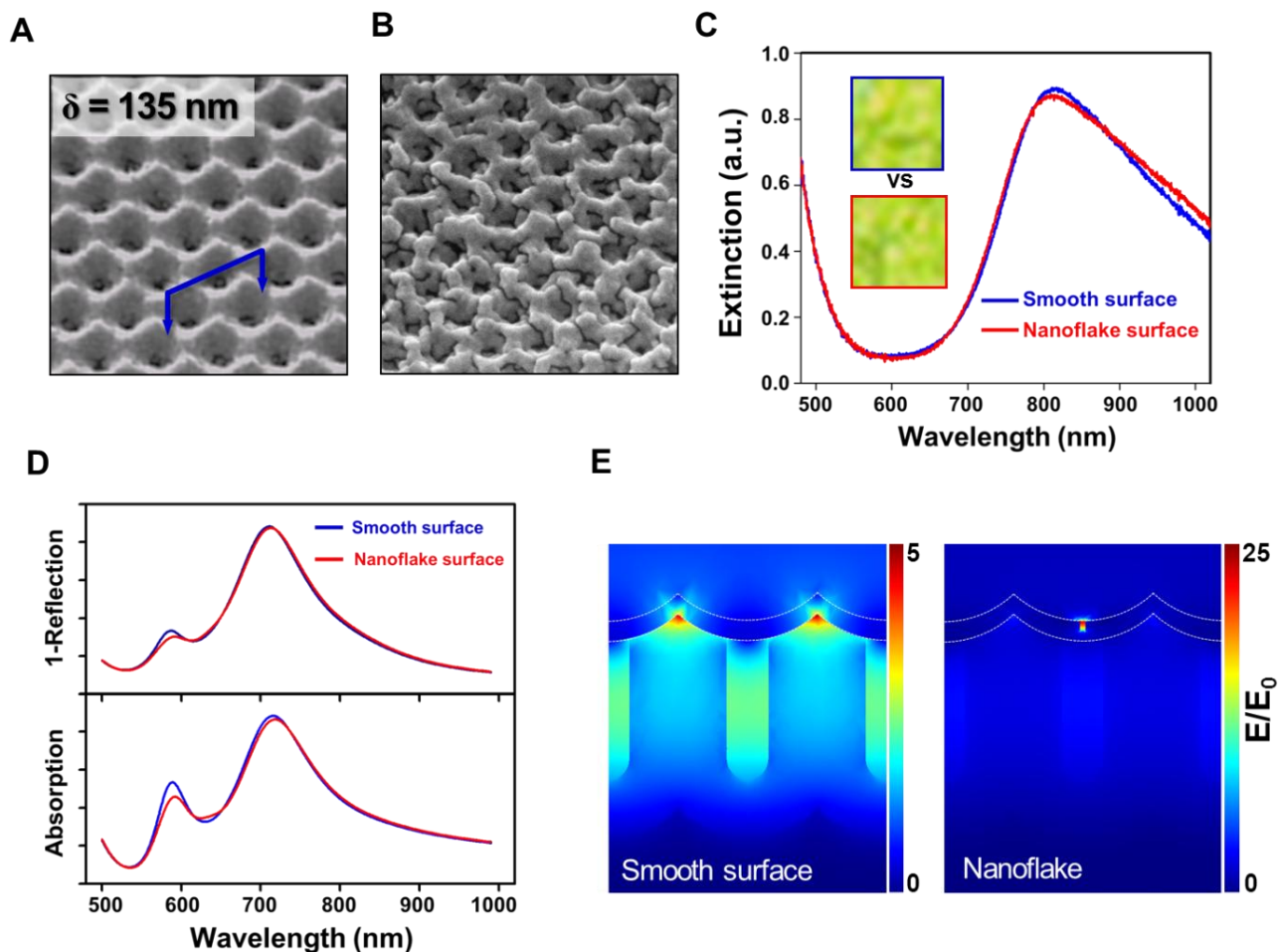


**Figure 5.3.** Comparison of smooth gold-AAO and nanoflake-AAO complex. (A & B) Scanning electron micrographs for the two cases of gold AAO. (C) The two cases of gold AAO shows identical optical extinction regardless of the gold layer morphology. Insets are naked-eye color taken by a general digital camera. (D & E) Simulation comparison for the two cases. Overall optical properties such as reflection and absorption show identical spectra, while strong optical hot-spots can be formed around nanogaps in the nanoflake layer.

Fig. 5.2 shows the simulation calculation of thin gold film conjugation and pure AAO template. The high dielectric property of alumina,  $\text{Al}_2\text{O}_3$  ( $\epsilon_r \approx 3.2$ ) can dramatically change optical response with a small change of  $\text{Al}_2\text{O}_3$  thickness. The simulation calculation for normal-excitation reflectance shows that the change of the oxide layer thickness can make following trends: the higher oxide layer generates the more numbers of resonance in ultraviolet-to-infrared range by red-shift in 200 to 600 nm and blue-shift in longer than 600 nm wavelength. Being combined with gold layer on top, resonance frequency does not change in less than 500 nm but longer wavelength than 500 nm is blue-shifted or red-shifted from pure AAO templates' resonance. The dynamic resonance shift of the Au-AAO complex,

with the pure AAO's broad range of resonance, shows effective capability of targeting a large range of resonance. Moreover, overall optical response extent becomes amplified by combining a plasmonic gold layer as shown in reflectance in Fig. 5.2.

Even though the AAO template is beneficial in resonance selectivity, optical field enhancement is not enough for sensitive molecular detection by being combined with smooth Au surface on top [15, 16]. In this respect, we adopted a metal deposition method to modulate grain growth by controls of temperature and deposit rate. The controlled deposition resulted in a large amount of nanogap morphology in the metal layer templates (here, we called this nanogap morphology as *gold nanoflake*). Differently from previously demonstrated roughened metal surface [17-19], the nanoflake shows certain regularity with the same periodicity as AAO template, and almost identical morphology in all different thickness of AAO template.

More interestingly, the nanoflake morphologies did not distinguish optical response from the smooth Au-AAO, when the thickness of gold layer was the same. Fig. 5.3A and B show two examples of smooth or nanoflake surface, and Fig. 5.3C is reflectance measurement from the two; naked-eye color (insets of Fig. 5.3C) and reflectance-based extinction spectrum did not show clear difference. Then, we applied a simplified surface morphology of nanoflake on the simulation to confirm identical optical response in reflectance. Simplified nanoflake surface contains a half depth of crevice with a nanogap of 2 nm. The comparison in smooth surface and nano-crevice surface resulted in quite identical reflectance and also absorption. However, the heat map of Fig. 5.3E shows a clear different in local field enhancement. In case of smooth surface, optical field is focused into  $\text{Al}_2\text{O}_3$  layer due to its high dielectric constant, while nano-crevice surface can bring optical response into the nanogap which can be accessible by external molecules and beneficial for molecular detection schemes.



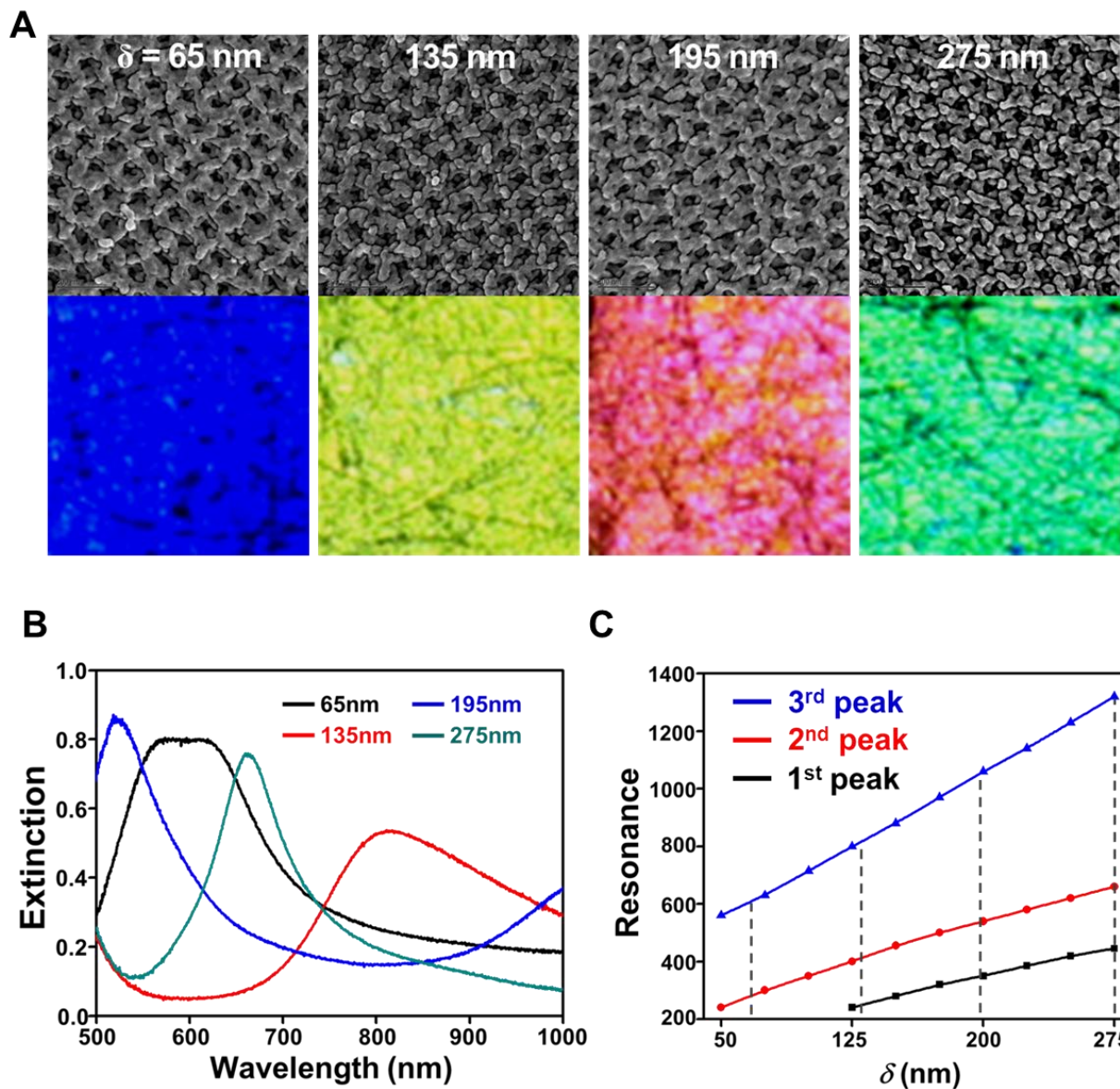


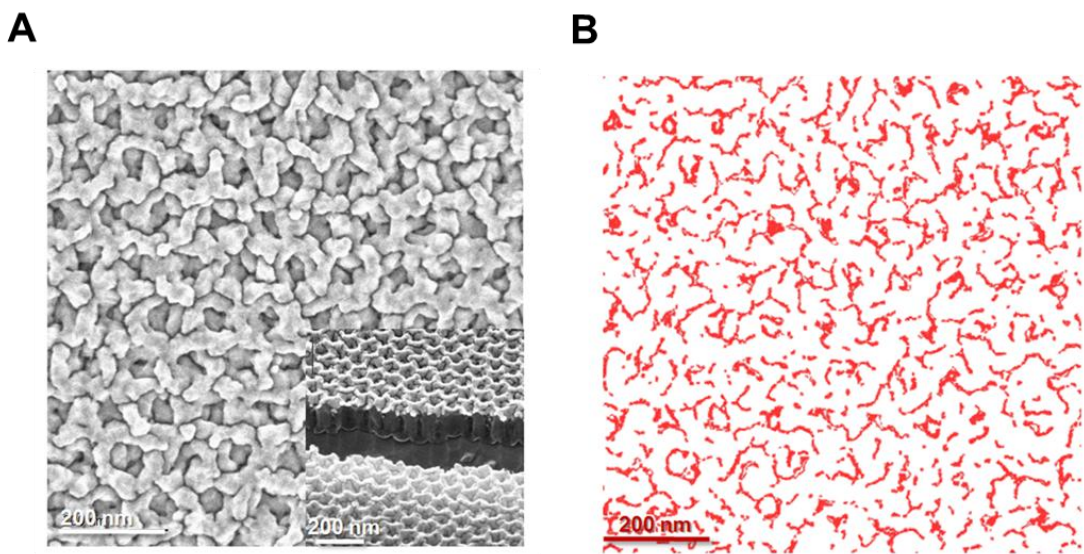
**Figure 5.4.** Optical properties of a fabricated nanoflake set. (A) SEMs and naked-eye colors for various thicknesses of AAO. The same morphology of gold layer was formed regardless of thickness of AAO. The same thickness and morphology of gold layer and different thickness of AAO produce a dynamic color change over visible light. (B) Extinction spectra of the four nanoflake samples. The extinction was measured based on reflection due to AAO's opacity. (C) A plot for simulated 1<sup>st</sup> to 3<sup>rd</sup> peaks change along various thickness of AAO. The vertical dot lines indicate 65, 135, 195 and 275 nm, and crossed points from 1<sup>st</sup>, 2<sup>nd</sup> and 3<sup>rd</sup> peak accord with the measured extinction resonances.

### 5.3 Single-molecule Level Detection via Nanoflake



By applying the same deposition method, a set of AAO templates (65, 135, 195, 275 nm) were conjugated with nanoflake structure on top (Fig. 5.4). The gold layer conjugation strongly amplified optical response of pure AAO complex, and generated colorful reflectance as expected from the simulation of Fig. 5.2. The same crystalline surface of AAO exhibited a clear reproducibility of nanoflake morphology regardless of AAO depth as shown in the SEM images. The reflectance-based extinction measured in a normal direction showed clearly distinguishing spectra (Fig. 5.4B) and individual resonance wavelength was well matched compared to the simulation results. Again, different morphology of gold surface was verified to generate the same optical response (far-field response) as a smooth thin film conjugation.

As demonstrated in the simulation, we can expect nanogaps in the flake-like nanoscale morphology to generate strong hot-spots when overall complex is optically resonated. Moreover, as predicted in Fig. 5.5B the high density of nanogaps can produce a large number of hot-spot in a unit area (i.e. laser focus spot in SERS measurement), therefore enhancing signal stability from molecular random motion in media. The set of gold AAOs was test as SERS substrate to detect a single-molecule level concentration of 1,2-bis(4-pyridyl)ethylene (BPE) [20]. The excitation source was 785-nm continuous wave laser. The measured extinction follows a sequence of 135, 65, 235, 195-nm AAOs in magnitude. Remarkably, the SERS signal intensities follows the optical extinction of 135, 65, 235, 195-nm AAOs and all of the four gold-AAOs demonstrated down to 1-fM concentration sensitivity. The analytical calculation compared to bulk Raman measurement can be down to  $10^{15}$ , which is higher than what has been reported so far (Fig. 5.5D).



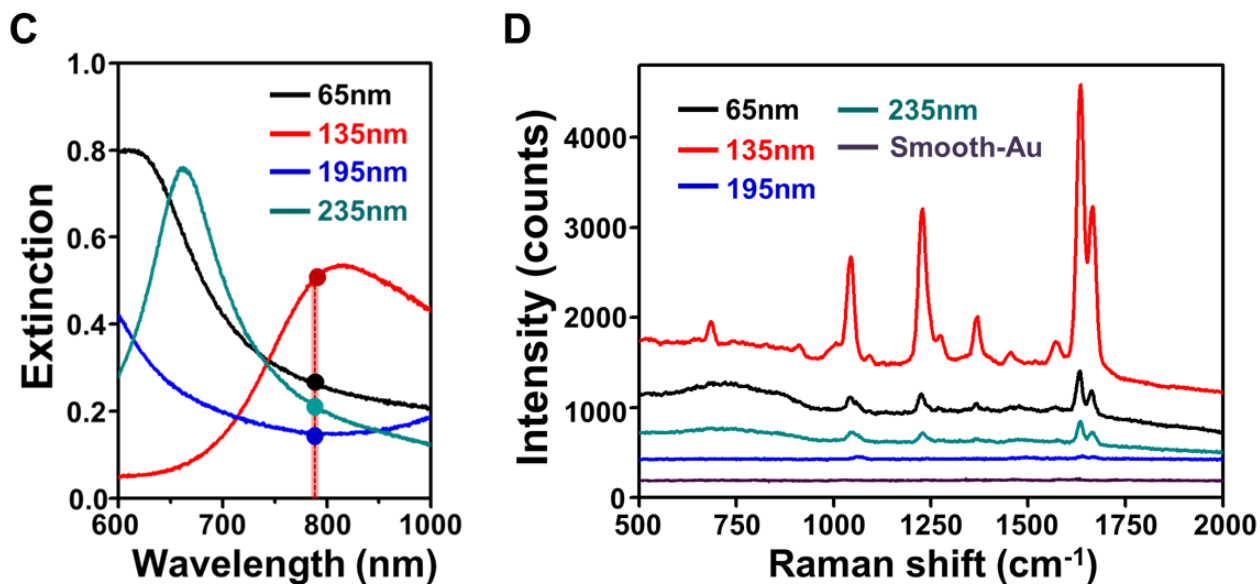


Figure 5.5. SERS measurement on the four different nanoflake samples. (A & B) high-resolution SEM images and expected hot-spot position. The morphology of nanoflake is expected to generate strong hot-spots uniformly over the gold surface. (C & D) The measured extinction shows 135, 65, 235 and 195nm sequence in extinction intensity at 785-nm wavelength, and 785-nm SERS measurement also shows the identical sequence of signal intensity. Conditions of SERS measurement were 1mW 785nm CW laser, 10 sec integration, and 1-fM 1,2-bis(4-pyridyl)ethylene MeOH solution.

## 5.4 Conclusion

In this study, we suggested an efficient way to design plasmonic substrates for sensitive molecular detection. The photonic crystal structure, anodized aluminum oxide can strongly modulate optical resonance, and then after combining with metallic layer, overall intensity of optical response can be strongly amplified. Compared to smooth surface, nano-crevice containing roughened surface can focus the overall optical response of the Au-AAO complex into nanoscale volumes, and generate strong hot-spots. By following this scheme, SERS measurement on gold nanoflake detected a single-molecule level in a conventional Raman setup while the sensitivities well followed the extinction extents among various AAO samples. We believe that this study shows interesting stories regarding frequency selectivity and detection sensitivity by minimizing other possible factors in molecular detection like atomic structural details.

## Reference

- [1] K. Kneipp, *et al.*, "Single molecule detection using surface-enhanced Raman scattering (SERS)," *Physical Review Letters*, vol. 78, pp. 1667-1670, Mar 3 1997.
- [2] S. M. Nie and S. R. Emery, "Probing single molecules and single nanoparticles by surface-enhanced Raman scattering," *Science*, vol. 275, pp. 1102-1106, Feb 21 1997.
- [3] R. P. Van Duyne, "Pushing the limits: Single molecule and single particle surface-enhanced Raman spectroscopy," *Abstracts of Papers of the American Chemical Society*, vol. 242, Aug 28 2011.
- [4] A. Otto, "Theory of first layer and single molecule surface enhanced Raman scattering (SERS)," *Physica Status Solidi a-Applied Research*, vol. 188, pp. 1455-1470, Dec 16 2001.
- [5] H. W. Liu, *et al.*, "Single molecule detection from a large-scale SERS-active Au(79)Ag(21) substrate," *Scientific Reports*, vol. 1, Oct 10 2011.
- [6] R. Gans, "The shape of ultra microscopic gold particles," *Annalen Der Physik*, vol. 37, pp. 881-900, Apr 1912.
- [7] M. Moskovits, "Surface-enhanced Raman spectroscopy: a brief perspective," *Surface-Enhanced Raman Scattering: Physics and Applications*, vol. 103, pp. 1-17, 2006.
- [8] R. M. Stockle, *et al.*, "Nanoscale chemical analysis by tip-enhanced Raman spectroscopy," *Chemical Physics Letters*, vol. 318, pp. 131-136, Feb 18 2000.
- [9] L. Y. Wu, *et al.*, "Optical Properties of the Crescent-Shaped Nanohole Antenna," *Nano Letters*, vol. 9, pp. 1956-1961, May 2009.
- [10] G. L. Liu and L. P. Lee, "Nanowell surface enhanced Raman scattering arrays fabricated by soft-lithography for label-free biomolecular detections in integrated microfluidics," *Applied Physics Letters*, vol. 87, Aug 15 2005.
- [11] M. I. Stockman, "Electromagnetic theory of SERS," *Surface-Enhanced Raman Scattering: Physics and Applications*, vol. 103, pp. 47-65, 2006.
- [12] V. Mizeikis, *et al.*, "Optical characteristics of two-dimensional photonic crystals in anodic aluminum oxide films," *Japanese Journal of Applied Physics Part 1-Regular Papers Short Notes & Review Papers*, vol. 43, pp. 3643-3647, Jun 2004.
- [13] I. Mikulskas, *et al.*, "Aluminum oxide photonic crystals grown by a new hybrid method," *Advanced Materials*, vol. 13, pp. 1574-+, Oct 16 2001.
- [14] G. D. Sulka, "Highly Ordered Anodic Porous Alumina Formation by Self-Organized Anodizing," in *Nanostructured Materials in Electrochemistry*, ed: Wiley-VCH Verlag GmbH & Co. KGaA, 2008, pp. 1-116.
- [15] T. Kumeria and D. Losic, "Reflective interferometric gas sensing using nanoporous anodic aluminium oxide (AAO)," *Physica Status Solidi-Rapid Research Letters*, vol. 5, pp. 406-408, Nov 2011.
- [16] D. Choi, *et al.*, "Self-Organized Hexagonal-Nanopore SERS Array," *Small*, vol. 6, pp. 1741-1744, Aug 16 2010.

- [17] H. Y. Liang, *et al.*, "Highly Surface-roughened "Flower-like" Silver Nanoparticles for Extremely Sensitive Substrates of Surface-enhanced Raman Scattering," *Advanced Materials*, vol. 21, pp. 4614-4618, Dec 4 2009.
- [18] Z. Q. Tian, *et al.*, "Surface-enhanced Raman scattering: From noble to transition metals and from rough surfaces to ordered nanostructures," *Journal of Physical Chemistry B*, vol. 106, pp. 9463-9483, Sep 19 2002.
- [19] S. Hayashi, "Sers on Random Rough Silver Surfaces - Evidence of Surface-Plasmon Excitation and the Enhancement Factor for Copper Phthalocyanine," *Surface Science*, vol. 158, pp. 229-237, 1985.
- [20] W. H. Yang, *et al.*, "A surface-enhanced hyper-Raman and surface-enhanced Raman scattering study of trans-1,2-bis(4-pyridyl)ethylene adsorbed onto silver film over nanosphere electrodes. Vibrational assignments: Experiment and theory," *Journal of Chemical Physics*, vol. 104, pp. 4313-4323, Mar 15 1996.

# Chapter 6

## Gold eu-Virus for Molecular Imaging

Understanding of biological systems is ultimately dependent on our ability of how to visualize biomolecular events with high spatial/temporal resolution in living cells. In this respect, optical antenna aided molecular spectroscopy has enormous potential for biomolecular imaging by minimizing intervention to biological events. However, practical targeting capability, nanoscale fabrication and single-molecule sensitivity need to be resolved to realize optimal optical antenna spectroscopy. A looking to nature suggests highly organized morphology of viral structure for an ideal optical antenna. Here, we demonstrate the feasibility of engineered plant viruses as novel optical antenna for fingerprint spectroscopy. Our experiments and simulations indicate that icosahedral viral architectures can increase sensitivity of plasmonic sensors up to  $10^6$  times, compared to smooth nanospheres. This study will expand the potential for engineering viruses as satellite nanoscopes capable of unprecedented spatiotemporal resolution for in-vivo targeting, imaging and drug delivery.

### 6.1. Introduction

Virus particles have highly ordered natural nanoarchitectures consisting of nucleic acid and a protective coat protein called a capsid. Even the simplest viruses have evolved the ability to enter cells directly or via various vectors, and to co-opt the host cellular processes needed to replicate their genomes and assemble viable progeny virions. During the last century, these processes have been intensively studied to understand virus structure and replication, and to control viral diseases of importance to human health and agriculture. More recently nanotechnology and biotechnology approaches have attempted to engineer viruses toward “*eu-virus*” [1] for diagnostic/therapeutic applications [2-6], nanomaterial synthesis [7, 8], protein recombination [9, 10], bio-energy applications [11, 12], and electronic components [13-15]. These new engineering approaches are designed to eliminate the viral disease-causing activities, while maintaining the inherent structure and cellular targeting capabilities for applications.

Especially, viral capsids have received particular attention for nanotechnology applications due to appealing features of self-assembly, regular icosahedral or helical geometry, a high degree of symmetry and polyvalency, and stability in harsh extracellular environments [16-19]. Moreover, the capsid morphological unit, or capsomer, has been chemically or genetically manipulated to incorporate external materials that may be useful

for diagnostic, imaging or targeting processes and that may have therapeutic function. Through identification and modification of capsomer peptide motifs, viral capsids have advanced their utility from protecting viral genome to resolving obstacles in development of ideal nanomaterials.

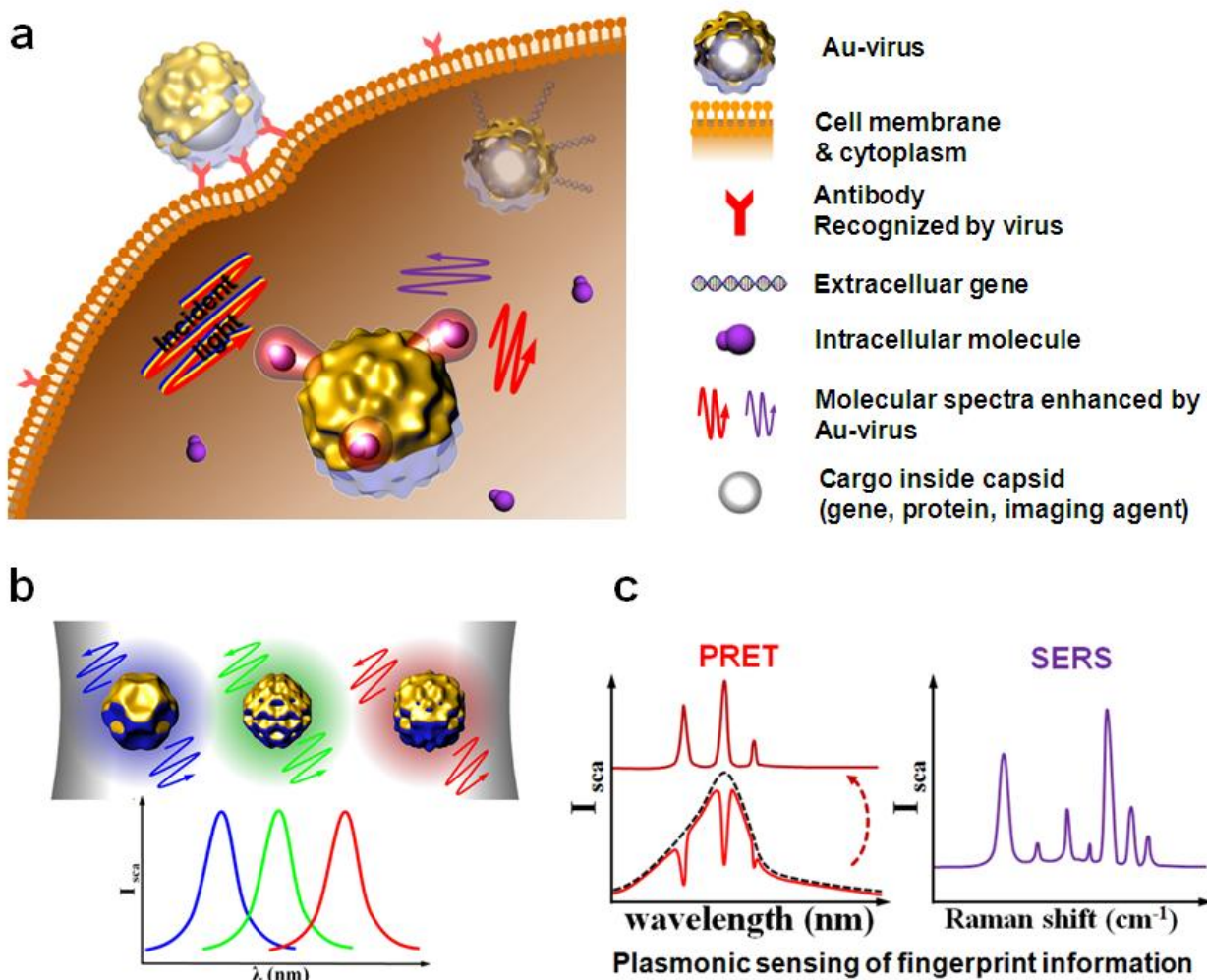


**Figure 6.1.** Schematic diagrams of *gold viruses* for molecular imaging. (A) Representative multifunctions of *gold eu-viruses* including targeting, delivery, imaging and sensing by sharing viral capsid with optical antenna. The thin gold layer on viral capsid works for optical sensing through molecular spectroscopic methods, and also enhances the other functions by carrying extracellular material including gene, protein, small molecules, fluorescence dyes and so on. (B) Plasmonic selectivity via various viral capsid morphologies. Icosahedral viruses have various 3-D protein structures, as well as diameters ranging from nanometers to micrometers, can be used to attain different plasmonic resonances with metal layer conjugation. (C) Plasmonic resonance energy transfer (PRET) and surface-enhanced Raman spectroscopy (SERS) as plasmonic sensor applications for molecular fingerprint spectroscopy. Plasmonic scattering spectrum of metal layers expresses molecular absorbance of nearby target molecules by PRET mechanism. Enhanced local electromagnetic field around the metal layer dramatically increases the molecular Raman scattering which is from molecular vibration.

Even with the simplicity of biochemical configuration, viral capsids provide high-regularity 3-dimensional morphology in a nanoscale which vastly exceeds current nanofabrication capabilities. Thus capsid morphology possibly suggests a solution to overcome practical issues of nanoscience requiring high-resolution geometry. Herein, we utilized the geometrical feature of viral capsid, especially to realize an ideal optical nanoantenna by using icosahedral plant viruses: belladonna mottle virus (BdMV), brome mosaic virus (BMV), cowpea mosaic virus (CPMV) and tomato bushy stunt virus (TBSV). The sub-nanometer resolution and 3-D detail [19, 20] on these nanometer-sized particles satisfy the required geometry in optical antenna applications. Moreover, each of the viruses replicates to high levels in plants and can easily be purified in gram amounts to near homogeneity, stored for several years without degradation or loss of biological activity, and manipulated genetically [21].

## 6.2. Viral Capsid as Plasmonic Nanoparticles

The advantages of using plant virus capsids as plasmonic nanoparticle include: 1) highly uniform-sized discrete nanoparticles, 2) a nanoscale 3-D morphology consisting of molecular-level protrusions and valleys, 3) a high degree of symmetry and polyvalency, 4) the structural resistivity to a big range of pH and temperature, and 5) mass production capabilities in plants under high levels of bio-safety. Moreover, genetically engineered or chemically modified viruses may also permit specific delivery into various classes of cells. Ideally, imprinting of a metal layer on a viral capsid surface can be motile optical antennae of sensing biomolecular information in a cellular level, together with capabilities of targeting, imaging and delivery [22-24] (Fig. 6.1A).

More specifically for the requirement of optical antennae, the morphological diversity of viral capsids available in nature can easily accommodate a wide range of plasmonic resonance (or *selectivity*) (Fig.6.1B). As discussed above and below, the nanoscale 3-D detail on capsid with conjugation of imprinted metal layer has the capability to more increase optical field intensity around discontinuous metal layer to improve detection (or *sensitivity*). Together with *selectivity* and *sensitivity*, gold *eu*-viruses are capable to fulfill plasmonic sensor applications such as surface-enhanced Raman spectroscopy (SERS) or plasmon resonance energy transfer (PRET), both of which encode molecular fingerprint information in a scattering spectrum (Fig. 6.1C).

## 6.3. Mathematical Model of Viral Capsid and Electromagnetic Simulation

A mathematical model expressing capsid structure, which provides fundamental understanding in viral image analysis, classification and morphological applications, can also benefit in designing of optical antennae for applications. Here, a morphological description of an intriguing capsid model (eq. 1) [25] was utilized to characterize optical properties of



*gold virus* through electromagnetic calculation. As an example, one set of variables ( $m$ ,  $p$ ,  $const$ ) in eq. 1 was chosen to express 3-D folded protrusion and valley on capsid, and gold layer with 5-nm thickness is assumed to normally deposited with a directionality (Fig. 6.2).

$$\left( \sum_{n=-m}^m e^{-(x+\tau y-n)^p} + e^{-(x-\tau y-n)^p} + e^{-\Sigma y+\tau z-n^p} + e^{-(y-\tau z-n)^p} + e^{-(z+\tau x-n)^p} e^{-(z-\tau x-n)^p} \right) - const = 0 \quad \text{eq. 1}$$

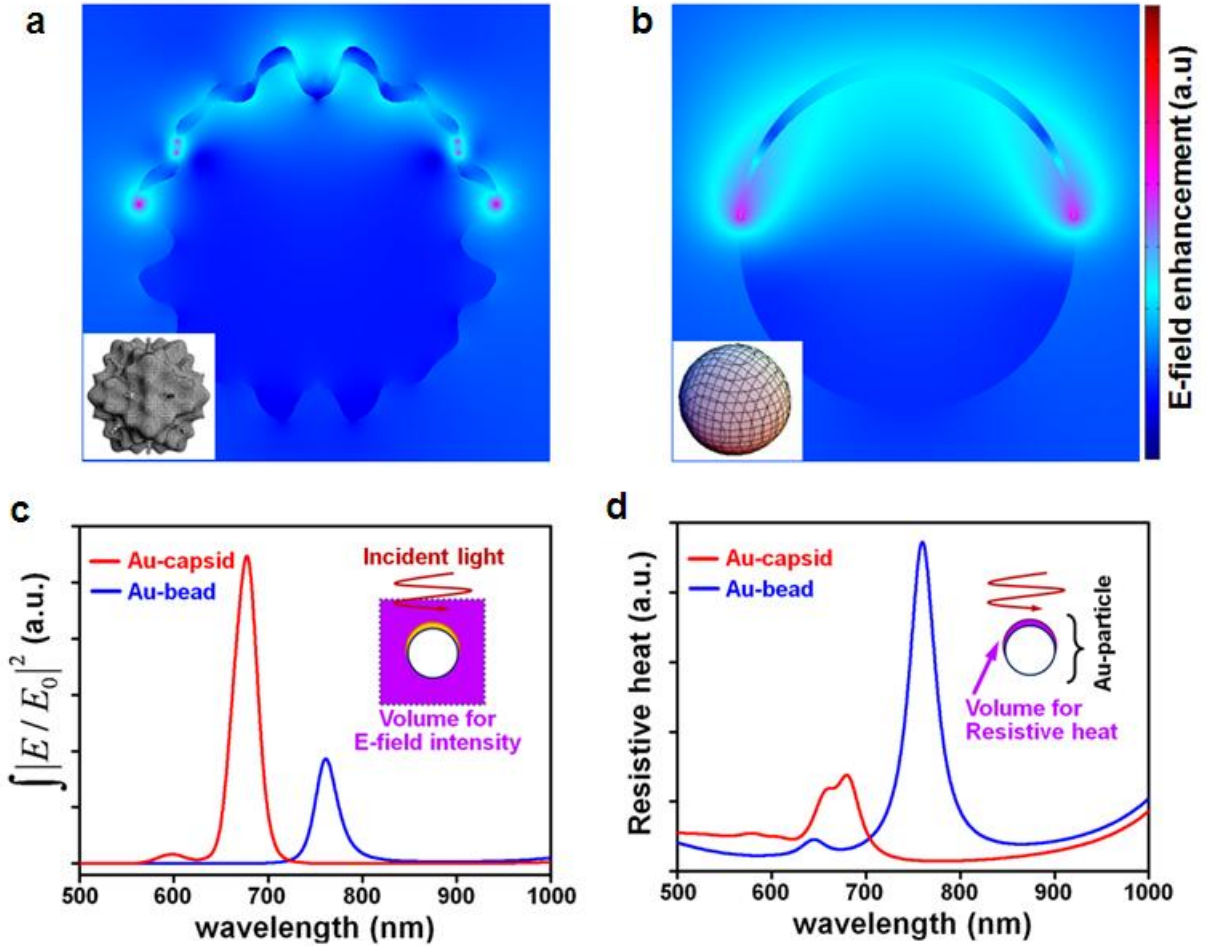


**Figure 6.2.** Electromagnetic simulations of *gold virus* with comparison to a gold conjugation on a similar sized nanosphere. To express an example of viral capsid, a representative equation was taken from the previous literature [25], and ( $m$ ,  $p$ ,  $const$ ) was set to (1, 4, 3.8). Both virus and bead template were scaled to fit to 30-nm diameter. Enhanced electric field is distributed in multiple spots around *gold virus*, but in a single spot around smooth nanosphere (A & B). Bigger surface-to-volume ratio together with multiple sharp tips induces bigger amount of



electromagnetic field scattering to media and less resistive heat inside the metal layer (C & D). These characteristics are beneficial for stable plasmonic optical sensor applications.

Simulation analysis on a mathematically modeled gold virus explicitly explains the benefits as an optical antenna on virus, compared to gold conjugation on a smooth nanosphere. As observed in Fig. 6.2A and B, protrusion and valley morphology of capsid can generate a-few-nanometer tip-to-tip distance between gold structures resulting in multiple hot-spot (or locally enhanced electric-fields) formation, while smooth surface of a nanosphere forms a single dome structure having a single edge. The light interaction with these nanoparticles can be more analytically compared regarding electromagnetic energy such as radiative and resistive energy (eq. 2) [26].

$$\begin{aligned} P_{\text{Total}} = P_{\text{radiative}} + P_{\text{resistive}} &= \int_V \mathbf{H} \cdot \frac{\partial \mathbf{B}}{\partial t} dV + \int_V \mathbf{E} \cdot \frac{\partial \mathbf{D}}{\partial t} dV \\ &= \oint_S (\mathbf{E} \times \mathbf{H}) \cdot \mathbf{n} dS + \int_V \mathbf{J} \cdot \mathbf{E} dV \quad \text{eq. 2} \end{aligned}$$

Here  $\mathbf{H}$  is magnetic field,  $\mathbf{B}$  is magnetic flux,  $\mathbf{E}$  is electric field,  $\mathbf{D}$  is electric displacement, and  $\mathbf{J}$  is current density. In contrary to gold conjugation on nanosphere, the *gold virus* generates more radiative energy to the volume surrounding the particle and less resistive thermal energy in the gold layer (Fig. 6.2C and D). Thus, *gold virus* can be considered being more useful for applications utilizing enhanced local optical field, including SERS and PRET. Also, less heat generation is beneficial for structural stability of nanoscale metal layer during light excitation on the optical antenna.

## 6.4. Demonstration of Gold Virus

To experimentally demonstrate *gold virus* efficiency, various thicknesses (2 to 10 nm) of gold were deposited by an e-beam evaporator on the highly purified plant viruses (BdMV, BMV and CPMV and TBSV) that had been adsorbed on glass slides as closely packed arrays. Then, the gold-conjugated viruses were lifted off the slide in water and mono-dispersed particles were reattached on another functionalized glass slide and the isolated *gold viruses* were characterized in more detail. Because the sequential engineering processes have a possibility to distort virus structure, the particles were compared by negative staining in a transmission electron microscope (TEM) before and after metal conjugation, to verify that the metal layer was firmly attached and that deposition had not altered the viral architecture. These TEM results indicated that the virus had maintained its original spherical structure and revealed the presence of electron-dense gold on each of the viruses examined (Fig. 6.3 D and E). Moreover, to assess whether deposition had destroyed the biological activity of the virus, infectivity assays were conducted by inoculating primary leaves of cowpea (*Vigna*

*unguiculata*) cv. Chinese x Iron plants before and after the engineering processes [27]. Both the wt and gold CPMV produced similar numbers of necrotic local lesions on the leaves. Hence the engineering process appears not to have a substantial effect on infectivity (Fig. 6.3C & F).

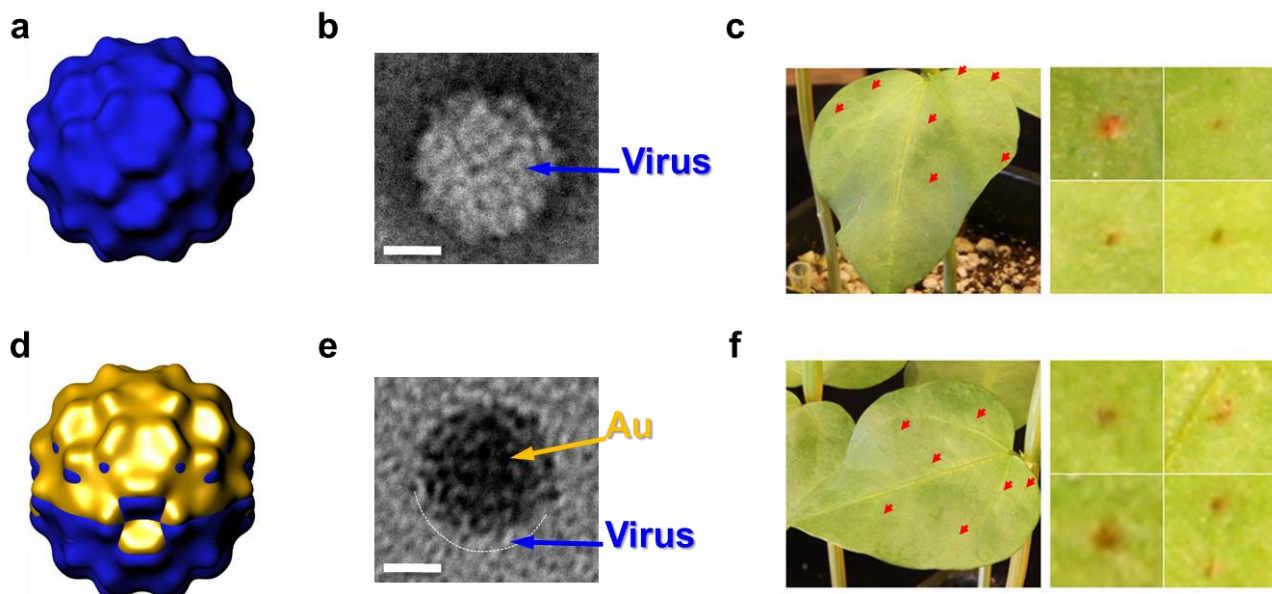
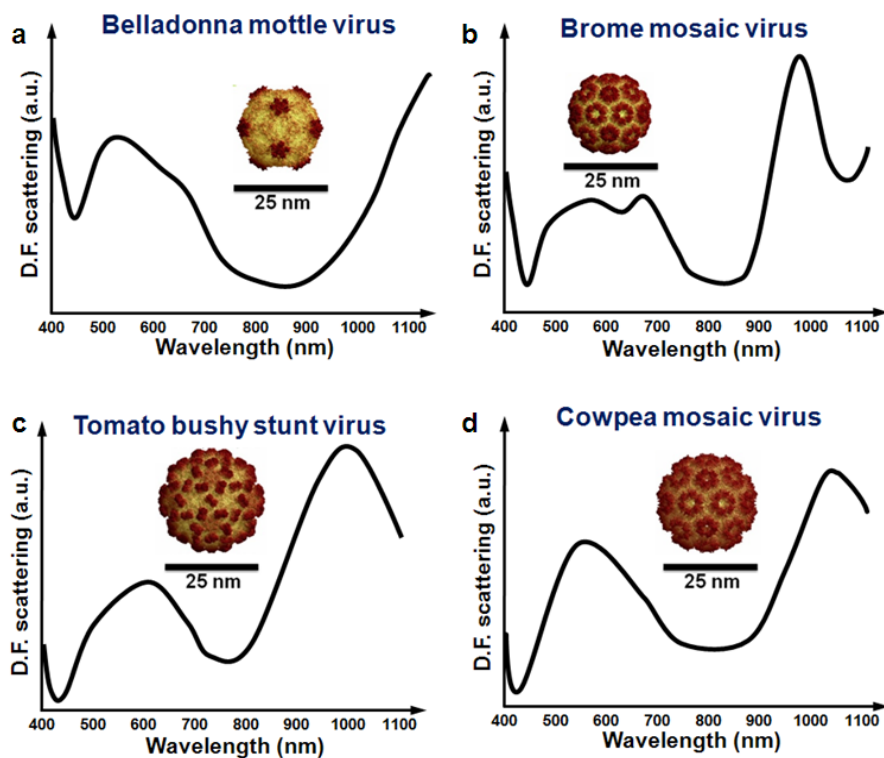


**Figure 6.3.** Gold viral structure and viral activity test. Schematic structure of original virus (A), and its conjugation with gold (D). TEM images were taken before (B) and after metal layer attachment (E). The scale bars in the TEM images are 10 nm. The infectivity of wt-CPMV (C) and gold-CPMV (F) was evaluated by a local lesion assay five days after mechanical inoculation of Cowpea (*Vigna unguiculata*) cv. Chinese x Iron plants. The red arrows indicate the local lesions, which are illustrated at higher resolution in the exploded panels to the right. Taken together, the original structure as well as inherent functions can still be maintained.

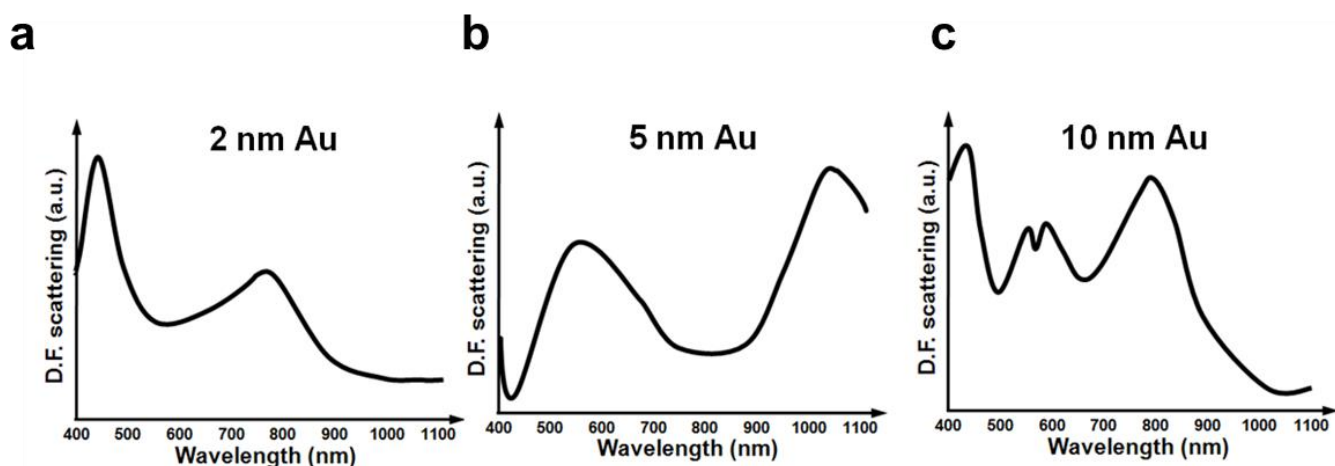
## 6.5. Far-field Characterization

A far-field optical spectrum, for characterizing plasmonic phenomena, was measured for each *gold virus* particle by a conventional dark-field method. In contrast to an identical thickness of gold conjugation on a smooth nanosphere, a multi-peak spectrum under dark-field scattering (Fig. 6.4) was clearly observed. Differences in diameter and variations in the topology of the viral capsids permitted spectral variation in the optical properties of the *gold viruses*. Overall, as the diameter increased, optical resonance was red-shifted, and the increased proximity of protruded capsomers resulted in clearer multiple resonances in the measured spectrum range. Also, changes of conjugated gold thickness can also tune the optical resonance (Fig. 6.5). As shown here, existence of various virus types and change of

metal thickness can provide a broad range of choice for the optical-antenna viruses to aim diverse optical resonances.



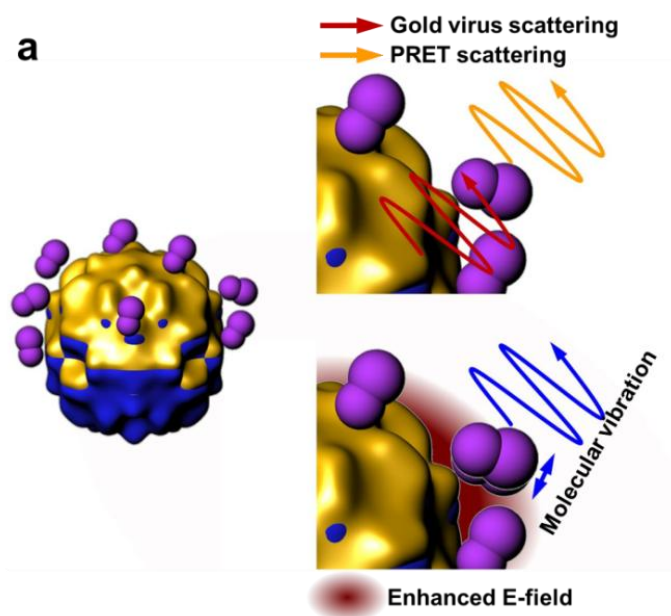
**Figure 6.4.** Characterization of optical properties of various *gold viruses*. The scattering spectra of 5-nm-gold viruses were measured in 400 to 1100 nm by conventional dark-field spectroscopy, (A) belladonna Mottle virus (BdMV) (B) brome mosaic virus (BMV), (C) tomato bush stunt virus (TBMV), and (D) cow pea mosaic virus (CPMV) were conjugated with gold at the same time by metal evaporation. Through further preparation, single nanoparticles were prepared on a transparent substrate (Supplementary Information). Different sizes and topologies of the viral capsids resulted in variations in the dark-field scattering spectrum.



**Figure 6.5.** Characterization of optical properties of various *gold viruses* by change the gold layer thickness. (A to C) The 2, 5, 10nm thickness of gold layer on CPMV virus shows a dramatic change of dark-field scattering.

## 6.6. Molecular Imaging via Gold Virus: PRET & SERS

Among plasmonic sensor applications, the two spectroscopy methods, SERS and PRET, are highlighted due to their fingerprint information delivery with a high sensitivity [28, 29]. Highly enhanced optical fields increase electron vibration and absorbance of molecules being in the enhanced optical field. Then, the enhanced optical field can be re-scattered to levels far superior to background noises to produce readable molecular fingerprints. This is the attribute and the fundamental mechanism of SERS and PRET *via* optical antennae. Additionally, non-invasive sensing, nanometer spatial resolution, and simple optical equipment increases the potential of these nanospectroscopies in biological applications. These plasmonic sensing capabilities can provide a new paradigm to multifunctional engineered viruses. Our demonstrations show that the 3-D folded capsid morphology generates a high sensitivity in such applications, supporting the potential of gold viruses as ‘*nanosatellites in a cellular galaxy*’ [30].



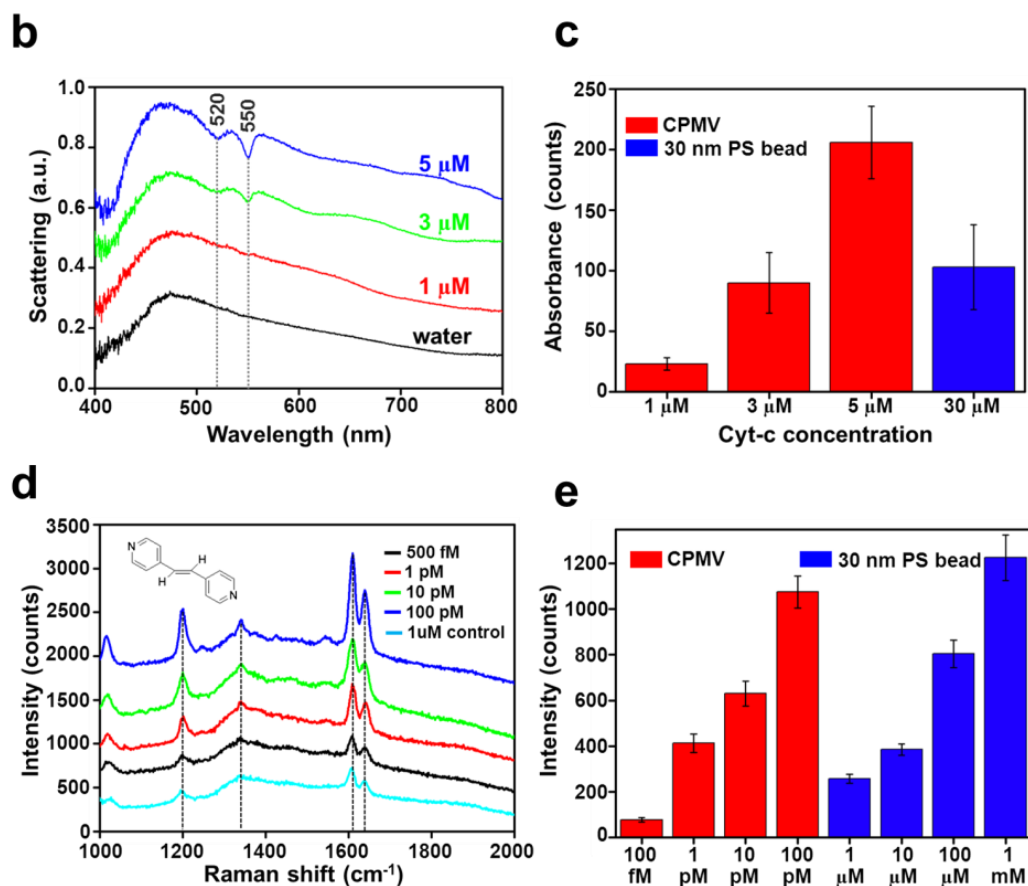


**Figure 6.6.** Plasmonic sensing *via* plasmon resonance energy transfer (PRET) and surface-enhanced Raman scattering (SERS) for molecular fingerprint information. (A) Schematic illustration of PRET and SERS. Regarding PRET, light scattering of the plasmonic particle is effectively re-absorbed by nearby target molecules, being reshaped with inversely indented absorption spectrum of the molecules. Comparison between before and after molecular presence around a nanoparticle provides the information of molecule's presence and its amount. Regarding SERS, locally-enhanced optical field increases molecular electron vibration, resulting in an increase in Raman scattering which provides molecular structure information. (B) Cytochrome-c PRET experiment results of 5-nm-gold CPMVs. Less than 3  $\mu\text{M}$  of cyt-c can be clearly imaged by individual gold CPMVs. This is shown as two dominant dips of 520 and 550 nm in the nanoparticle dark-field scattering that match with cyt-c absorption spectrum. (C) Comparisons of the *gold virus* PRET with a similar-sized gold-coated nanosphere PRET. (D) SERS spectra of BPE on gold CPMVs and gold-coated nanospheres with a 5-nm gold thickness. Gold CPMV yielded a set of clear fingerprint information at 1200, 1615 and 1635  $\text{cm}^{-1}$  Raman shifts at a picomole concentration of BPE, whereas gold-coated nanospheres resulted in a micromole detection. (E) Comparison of Raman scattering intensity in a peak of 1615  $\text{cm}^{-1}$ . The quantitative result shows 6 orders of magnitude greater sensitivity with gold virus.

PRET sensing, encoding molecular absorbance spectra into an optical antenna scattering, can be useful to map an intracellular distribution of biomolecules through absorption spectroscopy enabled by mono-dispersed optical antennae in a cell [31]. In our experiments, one derivative of *gold virus* was tested as an initial step toward *in-vivo* cellular imaging as suggested before [29, 31]. In brief, mono-dispersed gold viruses are fixed on a modified glass substrate. Then, a positively charged ligand (3-mercaptopropionic acid) were selectively attached on the gold layer to attract the target molecules (here, cytochrome c or cyt c). Various concentrations of reduced cyt c were detected by 5 nm-gold CPMV, and as a control experiment similar-sized smooth nanosphere (33 nm-diameter polystyrene bead) was tested in the same way. The results indicate that the *gold virus* is far more sensitive than the nanosphere with 10 fold higher magnitudes of absorbance encoding capability (Fig. 6.6B & C). The higher PRET efficiency attained by *gold viruses* can be explained by the multiple hot-spots on the CPMV surface, even after consideration of different surface areas of the gold layers on the polymer sphere (33 nm) and CPMV virus (31 nm) as a possibility of more molecules adsorption.

SERS, a highly enhanced nonlinear optical phenomenon, can attain higher sensitivities down to single-molecule detection [28]. Differently from PRET, the enhanced optical field around optical antennae directly increases molecular vibration modes and scatters the fingerprint information with a high amplification, which is SERS mechanism. Here, similarly packed CPMV particles and 33-nm nanosphere with 2-nm gold conjugation of having an optical resonance around 785-nm laser excitation were examined as a SERS substrate. By using a conventional target molecule (1,2-Bis(4-pyridyl)ethylene or BPE) for the purpose of enhancement factor comparison [32, 33], 2 nm-gold CPMV particles were clearly detected at sub-pico-mole concentrations of BPE, whereas the nanosphere substrate was detected only down to micro-mole concentrations. The comparison of detection limits denotes a  $10^6$  higher sensitivity of the 3D-folded viral capsid. This experiment supports that the virus morphology can provide enough sensitivity as single-particle-single-molecule SERS detection by combining with previously demonstrated optimization methods [34, 35]. Moreover, in the experiment Raman signals were stable with less than 10% deviation in time domain, even at the low concentrations of pico-moles. Blinking, commonly observed in previous literatures [28], was not observed in the gold virus SERS, which suggests the possibility of preconcentration around the atomic-scale surface morphology of viral capsid [36, 37].

## 6.7. Conclusion

In conclusion, we have proposed the usefulness of 3-dimensional viral capsids for optical antennae realization, and experimentally demonstrated the high sensitivity of these *gold viruses* for PRET and SERS spectroscopic imaging. Even though the optical-antenna-functional layer remained attached to the capsid surface, the gold virus maintained its inherent ability to infect host cells. Therefore, this study can pursuit be thought to extend current engineering virus applications, such as material container and drug delivery capabilities, and generate important new potential as sensitive probes (*nanosatellite*) in a live cell system (*cellular galaxy*) to image biological events at a molecular level. Additionally,

photothermal based drug activation will be also attainable through the plasmonic *eu-virus*; thus an ideal nanoparticle of active targeting, imaging, delivery and molecular sensing will be practically realized through the gold *eu-virus* researches.

## Reference

- [1] Prefix 'eu-' means 'well or good' from Latin (like 'eu-phonic', 'eu-rythmic', 'eu-tropic'). Here, "eu-virus" denotes beneficial virus by engineering harmful viruses.
- [2] J. D. Lewis, *et al.*, "Viral nanoparticles as tools for intravital vascular imaging," *Nature Medicine*, vol. 12, pp. 354-360, Mar 2006.
- [3] P. Singh, *et al.*, "Bio-distribution, toxicity and pathology of cowpea mosaic virus nanoparticles in vivo," *Journal of Controlled Release*, vol. 120, pp. 41-50, Jul 13 2007.
- [4] C. S. Rae, *et al.*, "Systemic trafficking of plant virus nanoparticles in mice via the oral route," *Virology*, vol. 343, pp. 224-235, Dec 20 2005.
- [5] Y. Ren, *et al.*, "Folic acid-conjugated protein cages of a plant virus: A novel delivery platform for doxorubicin," *Bioconjugate Chemistry*, vol. 18, pp. 836-843, May-Jun 2007.
- [6] W. B. Klimstra, *et al.*, "Targeting Sindbis virus-based vectors to Fc receptor-positive cell types," *Virology*, vol. 338, pp. 9-21, Jul 20 2005.
- [7] T. Douglas and M. Young, "Host-guest encapsulation of materials by assembled virus protein cages," *Nature*, vol. 393, pp. 152-155, May 14 1998.
- [8] M. Comellas-Aragones, *et al.*, "A virus-based single-enzyme nanoreactor," *Nature Nanotechnology*, vol. 2, pp. 635-639, Oct 2007.
- [9] M. C. Canizares, *et al.*, "Use of viral vectors for vaccine production in plants," *Immunology and Cell Biology*, vol. 83, pp. 263-270, Jun 2005.
- [10] H. B. Scholthof, *et al.*, "Plant virus gene vectors for transient expression of foreign proteins in plants," *Annual Review of Phytopathology*, vol. 34, pp. 299-323, 1996.
- [11] R. A. Miller, *et al.*, "Self-assembling light-harvesting systems from synthetically modified tobacco mosaic virus coat proteins," *Journal of the American Chemical Society*, vol. 129, pp. 3104-3109, Mar 21 2007.
- [12] M. Endo, *et al.*, "Porphyrin light-harvesting arrays constructed in the recombinant tobacco mosaic virus scaffold," *Chemistry-a European Journal*, vol. 13, pp. 8660-8666, 2007.
- [13] K. T. Nam, "Virus-enabled synthesis and assembly of nanowires for lithium ion battery electrodes (vol 312, pg 885, 2006)," *Science*, vol. 322, pp. 44-44, Oct 3 2008.
- [14] R. J. Tseng, *et al.*, "Digital memory device based on tobacco mosaic virus conjugated with nanoparticles," *Nat Nanotechnol*, vol. 1, pp. 72-7, Oct 2006.
- [15] E. Royston, *et al.*, "Self-assembly of virus-structured high surface area nanomaterials and their application as battery electrodes," *Langmuir*, vol. 24, pp. 906-912, Feb 5 2008.

- [16] R. Zandi, *et al.*, "Origin of icosahedral symmetry in viruses," *Proceedings of the National Academy of Sciences of the United States of America*, vol. 101, pp. 15556-15560, Nov 2 2004.
- [17] Q. Wang, *et al.*, "Natural supramolecular building blocks: Wild-type cowpea mosaic virus," *Chemistry & Biology*, vol. 9, pp. 805-811, Jul 2002.
- [18] M. Young, *et al.*, "Plant viruses as biotemplates for materials and their use in nanotechnology," *Annual Review of Phytopathology*, vol. 46, pp. 361-384, 2008.
- [19] T. S. Baker, *et al.*, "Adding the third dimension to virus life cycles: Three-dimensional reconstruction of icosahedral viruses from cryo-electron micrographs," *Microbiology and Molecular Biology Reviews*, vol. 63, pp. 862-+, Dec 1999.
- [20] M. G. Rossmann and J. E. Johnson, "Icosahedral Rna Virus Structure," *Annual Review of Biochemistry*, vol. 58, pp. 533-573, 1989.
- [21] J. Johnson, *et al.*, "Presentation of heterologous peptides on plant viruses: Genetics, structure, and function," *Annual Review of Phytopathology*, vol. 35, pp. 67-86, 1997.
- [22] M. J. Gonzalez, *et al.*, "Interaction of Cowpea Mosaic Virus (CPMV) Nanoparticles with Antigen Presenting Cells In Vitro and In Vivo," *Plos One*, vol. 4, pp. -, Nov 23 2009.
- [23] K. J. Koudelka, *et al.*, "Endothelial Targeting of Cowpea Mosaic Virus (CPMV) via Surface Vimentin," *Plos Pathogens*, vol. 5, pp. -, May 2009.
- [24] G. Destito, *et al.*, "Folic acid-mediated targeting of cowpea mosaic virus particles to tumor cells," *Nanomedicine-Nanotechnology Biology and Medicine*, vol. 3, pp. 349-349, Dec 2007.
- [25] S. Andersson, "The Structure of Virus Capsids," *Zeitschrift Fur Anorganische Und Allgemeine Chemie*, vol. 634, pp. 2161-2170, 2008.
- [26] J. D. Jackson, *Classical Electrodynamics*. New York: Wiley, 1999.
- [27] G. Bruening, *et al.*, "Evidence for participation of RNA 1-encoded elicitor in Cowpea mosaic virus-mediated concurrent protection," *Virology*, vol. 266, pp. 299-309, Jan 20 2000.
- [28] S. M. Nie and S. R. Emery, "Probing single molecules and single nanoparticles by surface-enhanced Raman scattering," *Science*, vol. 275, pp. 1102-1106, Feb 21 1997.
- [29] G. L. Liu, *et al.*, "Quantized plasmon quenching dips nanospectroscopy via plasmon resonance energy transfer," *Nature Methods*, vol. 4, pp. 1015-1017, Dec 2007.
- [30] L. P. Lee, "Satellite nanoscope and cellular BioASICs for quantitative biomedicine," in *Engineering in Medicine and Biology Society, 2009. EMBC 2009. Annual International Conference of the IEEE*, 2009, pp. 4582-4585.
- [31] Y. H. Choi, *et al.*, "Plasmon Resonance Energy Transfer (PRET)-based Molecular Imaging of Cytochrome c in Living Cells," *Nano Letters*, vol. 9, pp. 85-90, Jan 2009.



- [32] J. G. Fan and Y. P. Zhao, "Gold-Coated Nanorod Arrays as Highly Sensitive Substrates for Surface-Enhanced Raman Spectroscopy," *Langmuir*, vol. 24, pp. 14172-14175, Dec 16 2008.
- [33] R. P. Vanduyne, *et al.*, "Atomic-Force Microscopy and Surface-Enhanced Raman-Spectroscopy .1. Ag Island Films and Ag Film over Polymer Nanosphere Surfaces Supported on Glass," *Journal of Chemical Physics*, vol. 99, pp. 2101-2115, Aug 1 1993.
- [34] L. Y. Wu, *et al.*, "Bioinspired Nanocorals with Decoupled Cellular Targeting and Sensing Functionality," *Small*, vol. 6, pp. 503-507, Feb 22 2010.
- [35] W. E. Doering and S. M. Nie, "Spectroscopic tags using dye-embedded nanoparticles and surface-enhanced Raman scattering," *Analytical Chemistry*, vol. 75, pp. 6171-6176, Nov 15 2003.
- [36] S. R. Emory, *et al.*, "Re-examining the origins of spectral blinking in single-molecule and single-nanoparticle SERS," *Faraday Discussions*, vol. 132, pp. 249-259, 2006.
- [37] E. A. Albrecht, "'German-Americans' - Rippley,Lj," *German Quarterly*, vol. 50, pp. 384-384, 1977.

# Chapter 7

## Concluding Remarks

The extensive research into metallic nanostructures over the last couple decades deepened the understanding of plasmonic phenomena and utilized them to various applications in a broad range of research fields. And ‘Plasmonics’ is expected to continue to mature existing applications and find new applications due to newly found promising characteristics. Over the six main chapters, fundamentals of plasmonics were discussed in terms of molecular detection via plasmonics, which is considered as the most promising application. Distinguished from previous approaches, this thesis mainly consider physical fields formed around excited plasmonic structures by including optical field amplification, photothermal heat generation, electric and temperature field gradients, depolarization, and non-straight Poynting vector. It is true that the most important characteristic of plasmonics for molecular detection is to attain large optical cross-section and focus optical response to strong hot spots, but a set of strategies like metal choice and required geometry are already prevalent and relative easy approaches of using numerical (or sometimes analytical) methods are well-established and prevalent. However, the difference shown in the thesis should be further discusses for improved molecular detection as well as in-depth understanding of molecular signal near plasmonic structures.

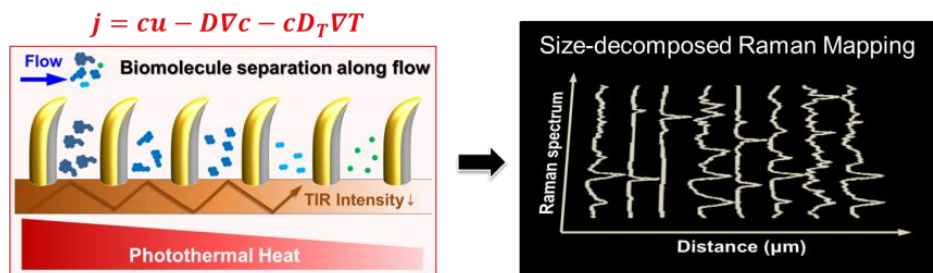
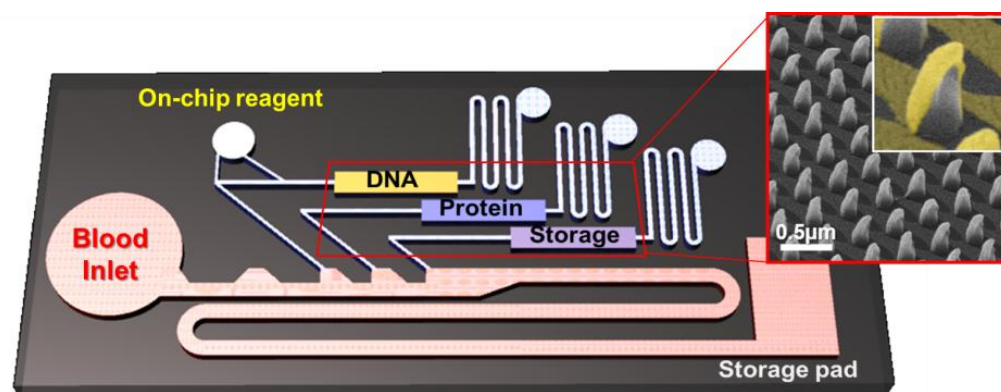


**Figure 7.1.** A plasmonic sensor built-in diagnosis chip. A plasmonic sensor array (i.e., eagle-beak nanoantenna) will enable precise detection of molecular fingerprints as well as function as biomolecular separator by using photothermal heat.

The main purpose of plasmonic-aided molecular detection can be various from improved sensitivity to applications to diverse levels of system. One of ultimate goals of my research is a diagnosis chip of precise molecular detection. Since central facilities like hospitals and research centers are not available for every situation and will be even until a far future, ‘point-of-care’ device will be an important portion as a health-care method. For improved biomolecular information, a plasmonic-aided sensing platform is suggested as shown in Fig. 7. 1. From sample preparation to analysis to storage for central facility, a single chip can function. Here, a plasmonic structure like eagle-beak will be useful to separate target molecules along size and preconcentrate by photothermal heat generation. Thus, scanning along a plasmonic sensor array will be able to discover various biomolecules with improved accuracy.

Also, since plasmonic-aided molecular detection is a non-invasive manner to a living cell, applying molecular detection methods to a living cell characterization is also expected. The critical lack of understanding in biological systems is quantitative information in a dynamic way, which is now suggested to be overcome by plasmonics. For better quantitative information and physiologically meaningful data from living cells, a single-cell culture platform will be combined with various plasmonic sensors like substrate and floating particles. Fig. 7.2 shows a proposed opto-fluidic platform to enhance our understanding of single-cell heterogeneity and dynamic factors such as cell-cell communications. The presented microfluidic platform is expected to mimic a tissue consisting of many different types of cells, and to control microenvironment by involving directional cell-cell communication along fluidic streamline and continuous refreshment of media.

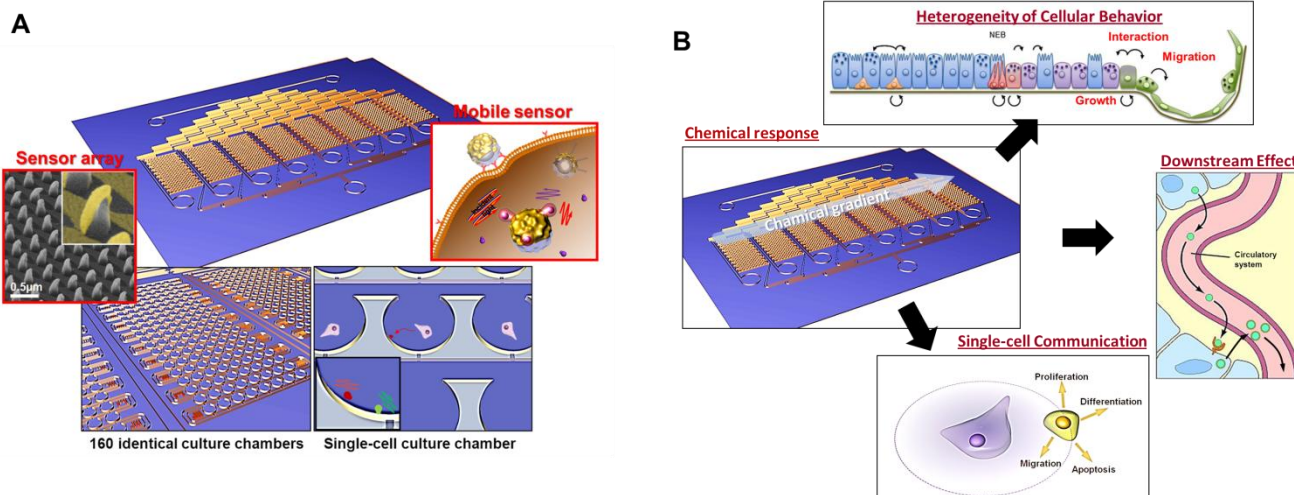


**Figure 7.2.** A microfluidic platform with plasmonic sensors will provide a precise characterization of cellular communication by detecting secretion molecules.

In conclusion, along with fundamental researches in plasmonics as shown in this thesis, characteristics not discovered yet will add up and mature potential of plasmonics. Especially, the plasmonic-aided molecular detection has proven its strength (e.g., single-molecule detection) and will be connected to a broad range of applications. The flexibilities in size, fabrication, and operation manner will have less limitation in applications and will bring improved understanding to various systems such as biological systems.

# Appendix

## A. Fabrication of Metallic Nanotstructures

### A.1. Eagle-beak Nanoantenna

Laser interference lithography was applied to fabricate nanopillar array on a quartz substrate. AZ3035 was used as photoresist. The pillar dimension was varied from 120 ~ 250 nm diameter and 400 ~ 550 nm height. Electron beam Evaporator (Edward EB3 E-Beam Evaporator) was used in the metal deposition onto laser interference pillars. First, 1 nm thickness titanium was deposited as an adhesion layer, and then 20 nm thickness gold was deposited. The thickness of deposited metal was controlled by crystal monitor built inside the evaporation chamber. The rate of gold deposition was manipulated by electron beam intensity. Slow deposition at the rate of 0.01 nm/sec or less took more than an hour to finish the target thickness, while the temperature of the chamber continued to increase and was saturated at 85 °C, which is higher than the melting point of photoresist. Also, the rotation of the sample holder of which the rate was 70 Hz enforced centrifugal force on each LIL pillar the samples. The combination of high temperature and centrifugal force resulted in the bent structure of eagle-beak. The curved tip of the eagle beak was created by the combination of two typical phenomena of evaporation deposition: bending photoresist pillars by localized heating and ‘edge-rounding’ S1. Heat from the e-beam melting process and evaporated hot metal particles made the polymer LIL pillars locally melt at the top. The centrifugal force of sample rotation bent the softened top part of pillars (Fig. A.1). Moreover, the typical phenomenon called ‘edge-rounding’, which usually happens in metal adhesion on oblique surfaces, made the gold layer sharper at the pillar surface to work as the EM-field focus point.

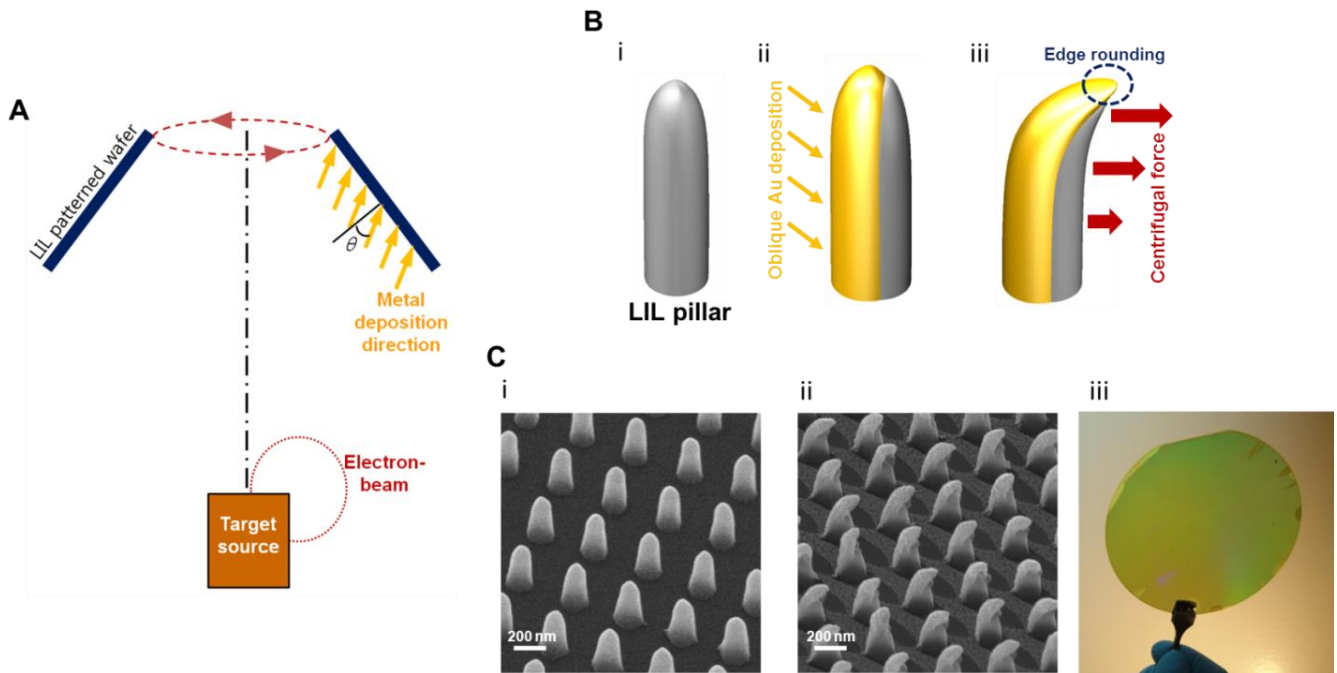


**Fig. A.1.** Metal deposition process in the eagle-beak fabrication. (A) Schematic diagram of evaporation deposition. By changing the angle of sample to the normal direction of deposition, oblique angle deposition can be applied. (B) Schematic diagram of bending and edge rounding of eagle-beak during the deposition. (C) Scanning electron micrographs of bare laser-interference pillars and eagle-beak structure after deposition, and a wafer-scale eagle-beak substrate.

## A.2. Gold Nanoflake

A pure aluminum sheet of 99.999% (2-mm thickness) was electropolished to remove surface irregularities. After washing the surface, electrochemical anodization was applied in 0.3M oxalic acid solution overnight. After this 1st anodization, aluminum oxide layer is removed to expose uniform dimple aluminum surface (mixture of 1.8 % chromic acid and 6 % phosphoric acid at 65 °C for 6 hrs). Then 2nd anodization is applied in the same condition as the 1st anodization with various times to control depth of aluminum oxide nanopore (about 100-nm depth per 1 min).

On top of AAO templates, 15-nm gold thin film was deposited by controlling temperature and deposit rate. Specifically, a process of 80°C chamber temperature, 0.01~0.05nm/sec deposit rate, 3 nm thickness was 5 times repeated with a cooling break to 30 °C. We assume that the repeats of hot and cool temperature cause a large amount of thin fragment growth with nanogaps.

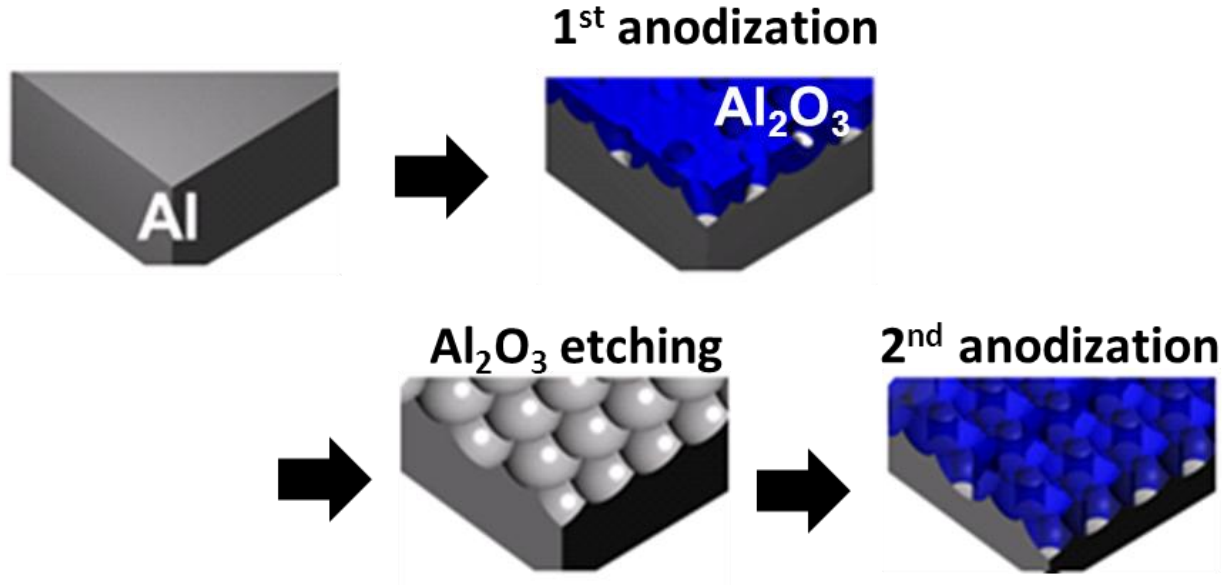


**Fig. A.2.** Process of anodized aluminum oxide. From a 2-mm thickness 99.999% aluminum plate, a series of two step anodization and etching process results in a hexagonally arrayed nanohole structure. The periodicity and depth of hole can be modulated by the condition of anodization.



### A.3. Gold Eu-virus

Plant leaves having viral infection symptom were harvested one or two weeks after mechanical inoculation. Then viruses were purified from the infected leaves by standard methods described by previous literature. Harvested viruses were stored at  $-20\text{ }^{\circ}\text{C}$  with addition of 5% ethylene glycol until the usage. Viruses can be stored for many years and remain infectious.

A conventional electron-beam evaporator (Edwards EB3 Electron Beam Evaporator) was used to deposit various thicknesses (2 to 10 nm) of gold on the top of drop-and-dry viruses on a clean glass slide. For control experiments, 33 nm-diameter polystyrene beads (Duke Scientific Corp.) were prepared in the same way and deposited in the same operation. To decrease the temperature during the deposit and to increase the deposit directionality, the evaporation started in a high vacuum ( $< 4 \times 10^{-6}$  torr) and the deposit rate was high ( $\sim 0.5$  nm/sec). After the deposit, the lift-off in water and reattachment on a thiol-functionalized glass by 3-mercaptopropyl-trimethoxy-silane (MTS) were followed for the optical characterization of isolated nanoparticles.

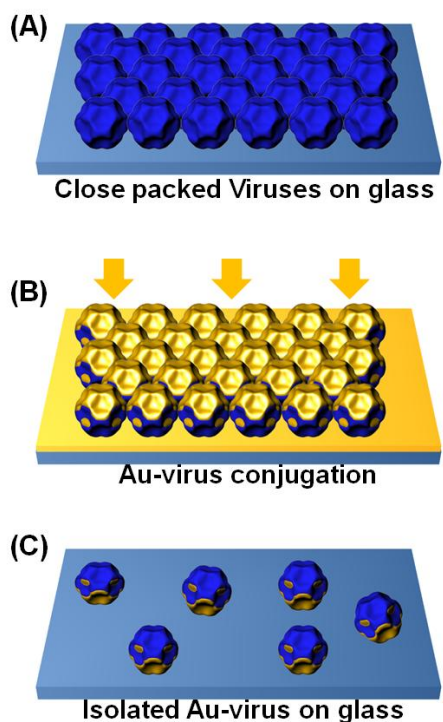


**Fig. A.3.** Au-viruses conjugation processes. (A) After packing viruses on a glass substrate through drop casting method, (B) thin gold layer was deposited on the top by using electron-beam evaporator. The samples in this step were characterized for optical properties and SERS measurement. (C) For single-particle based experiment including PRET characterization, Au-virus particles were monodispersed on a modified glass substrate having thiol exposure.



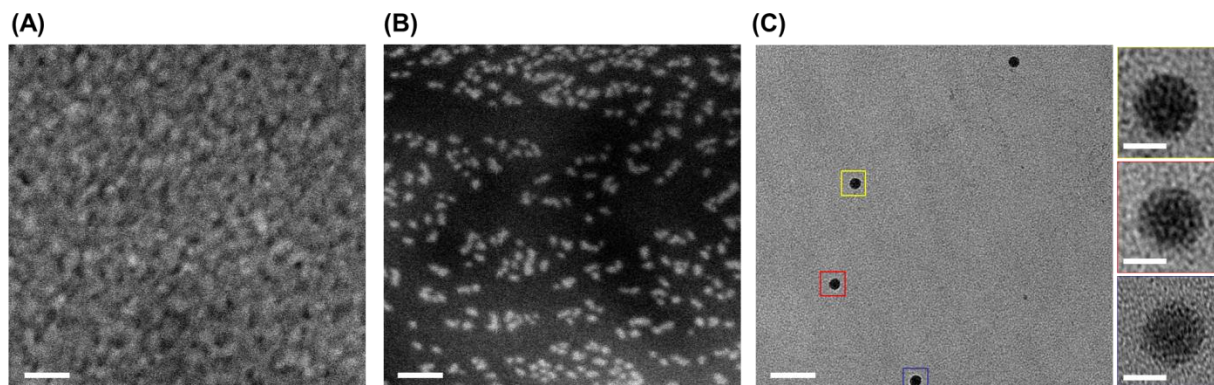


**Fig. A.4.** Electron microscope images of gold virus. (A) SEM image of gold deposited closed packed CPMV on a glass slide. (B) SEM image of monodispersed 5-nm gold CPMV on glass slide. (C) TEM image of 5-nm CPMV showing regular structures. All scale bars are 100 nm; Ones of close-up image in (C) are 20 nm.

## B. Raman Measurement

A Raman system was built to an inverted microscope (Axiovert200, Zeiss) with 785 nm diode laser (Power Technology, Inc.). The laser was shined through a dichroic filter and focused with 20x objective lens (NA 0.4). To avoid bubble generation in the laser-focused spot, the intensity of the laser was controlled by a neutralized filter positioned in front of the laser. Raman scattering from the sample was gathered by the same objective lens and analyzed by a spectrometer (Princeton Instruments Acton SP2300).

As a commonly available SERS molecules, BPE and BT were used to characterize functionalities of eagle-beak design as SERS substrate. BPE and BT were purchased in Sigma-Aldrich Co. (CAS number: 13362-78-2 and 108-98-5, respectively), and BPE was further purified by using a conventional re-crystallization process<sup>S2</sup>. For BT measurement, original BT solution was diluted to 5mM with ethanol (EtOH). Then 30min incubation and rigorous 5min rinsing with EtOH was applied to make a monolayer of BT on the eagle-beak gold layer S3. On the rotation stage, the dried eagle-beak sample was measured by the Raman system. Also three different sets of methanol-based BPE solutions were prepared from 1 mM to 1 fM by diluting solutions 1/10. When the BPE solution was measured by the Raman system, it was confined in a 1 cm<sup>2</sup>-sized polydimethylsiloxane (PDMS) well, a 0.25 mm-thickness glass cover slide on the top and a 1 mm-thickness microscope slide on the bottom. A piece of eagle-beak SERS substrate fractioned from the fabricated 4" original wafer was attached to the microscope slide in the middle of the PDMS well. Without incubation time, each SERS measurement was done from the lowest concentration. For Raman measurement of 0.5 M concentration, the same apparatus consisting of PDMS and two glass slides was used.

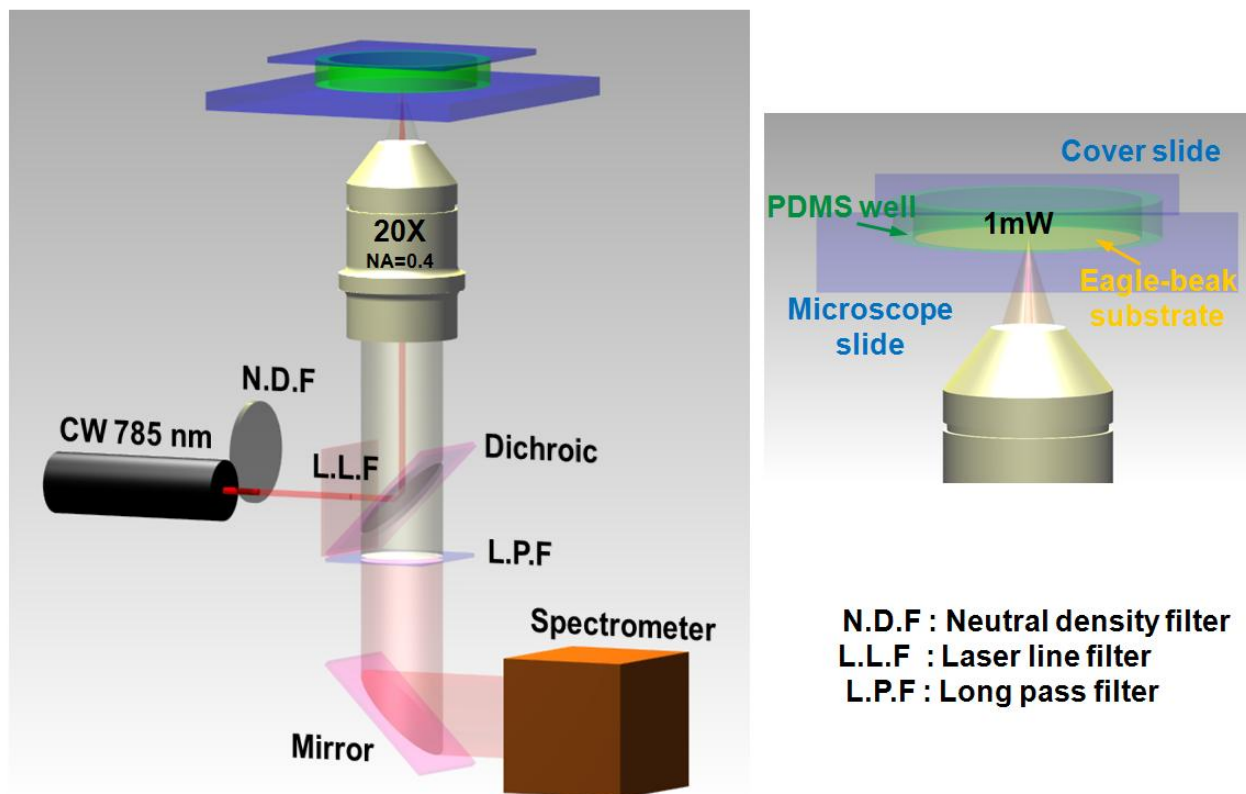


**Fig. B.1.** Schematic diagram of a setup of Raman spectroscopy built in an inverted microscope.

## C. Plasmon Resonance Energy Transfer (PRET) Experiment

Plasmonic particles (i.e. gold virus) were functionalized with 3-mercaptopropylcarboxylic acid (MPA) by incubation in 1 mM MPA isopropyl alcohol (IPA) for 24 h. Then the glass slides were thoroughly rinsed with IPA for 5 min. Reduced form of cytochrome c (Sigma, St. Louis, MO) which was sold in the oxidized form is attained by the addition of excess sodium dithionite ( $\text{Na}_2\text{S}_2\text{O}_4$ ) in deoxygenated PBS buffer solution as described in the previous literature. As increasing the concentration of cytochrome, dark-field spectra were kept measured and post-processed to decode the PRET quenching intensities.

## D. Numerical Simulation

**Electromagnetic (EM) field:** Most of plasmonic structures studied in this thesis were simulated as 3-dimensional structure by using a multiphysics software COMSOL (version

3.5). If not mentioned, 3-D scattering RF module was used. In case of nanorod and gold virus, a single structure was simulated by adding perfectly matched layer to set infinite boundary condition. In case of periodic structures like eagle-beak nanoantenna, gold flake on AAO and nanodisk array, proper periodicity was defined by using built-in boundary function. The dielectric properties of gold layer which is modified Drude Lorentz model was taken from the previous literature. The mesh was set to be as dense as 1 nm in gold material if the region is not much curved and a quarter of wavelength in dielectric.

Physical factor	Equation
Free convection with Buoyant force	$\rho \vec{u} \cdot \nabla \vec{u} = \nabla \cdot [-\rho \vec{I} + \eta(\nabla \vec{u} + (\nabla \vec{u})^T)] + \vec{F}$
Thermal Conduction	$\rho C_p \frac{\partial T}{\partial t} + \nabla \cdot (-k \nabla T) = Q - \rho C_p \vec{u} \cdot \nabla T$
Chemical diffusion Thermal diffusion Plasmonic trapping	$\frac{\partial c}{\partial t} + \nabla \cdot (-D \nabla c - c D_T \nabla T - c \mu F + c \vec{u}) = R$

**Table D.1.** Equations involved in molecular movement around eagle-beak. Photothermal heat induces buoyant force ( $\vec{F}$ ) in free convection, heat source ( $Q$ ) in thermal conduction and temperature gradient ( $\nabla T$ ) in the diffusion equation. Plasmonic trapping force which dominantly acts around the hot-spot can be expressed as  $F$  with multiplying mobility coefficient ( $\mu$ ) in the diffusion equation. Diffusion coefficient and thermal diffusion coefficient were taken from other references. Other physical factors were followed to general properties of glass, gold and methanol. In those equations,  $\rho$  is density of solution,  $\eta$  is dynaminc viscosity,  $C_p$  is heat capacity,  $k$  is thermal conductivity and  $R$  is reaction rate.

**Molecular movement:** To simulate molecular movement around the nanostructure, the multi-physical equations were included described in Table D.1 by using the software COMSOL. The photothermal heat was calculated separately from EM simulation since the time scale is definitely different between electromagnetics and others.

## E. High Sensitivity in SERS detection

The sensitivity of SERS is proportional to the number of molecules exposed to optically enhanced hot spots and electric field with a factor of four. In case of single-molecule level detection, we have to consider the number of molecule in a critical way since

the probability for target molecule to stay in the attoliter volume of hot spots. A strategy we utilized for sensitivity molecular detection in this thesis can be summarized as following:

$$EF \propto N_{molecule} \cdot |E|^4$$

$N_{molecule}$ : Number of Molecule in *hot-spot*,  $E$ : Electric-field



Electric field	Number of molecule in <i>hot-spot</i>	
	Preconcentration	High density of <i>hot-spot</i>
<b>-High sensitivity</b> : High number of EF  <b>-Geometry of nanoprobe</b> : Sharp tips or close tip-to-tip distance	<b>-Detection stability</b> : High detectability in low concentration  <b>-Thermal-based</b> : Geometry for focus of thermal pushing & localized vortex  <b>-Plasmonic-based</b> : high gradient of electric-field around hot-spot	<b>-Spatial detectability</b> : Large area of SERS spot  <b>-3-dimensional structures</b> : Vertically formed hot-spot to avoid unexpected plasmonic coupling

## F. Geometry Factor in Chapter 3

In the chapter 3, we introduce a geometry factor to simplify thermal profile around nanorod as spherical shape as shown in following equations.

$$T_r|_{r=r_0} = T_{inf} + \frac{Q}{4\pi k r_0}$$

$$\left. \frac{dT_r}{dr} \right|_{r=r_0} = f \cdot \left[ -\frac{Q}{4\pi k r_0^2} \right]$$

In the equations, the temperature does not require the factor correction due to a uniform temperature on high-conductivity. But the asymmetric shape of nanorod, resulting in different surface-to-media volume ratio along the surface of nanorod, generate uneven

thermal gradient on the surface, and therefore requires the geometry correction factor  $f$ . From the empirical comparison, the value was set as shown in Table E.1.

Heat amount	Nanorod Size	0.5	0.75	1	1.25	1.5
8.38175E-08	Simulation	1.27E+08	5.60E+07	3.15E+07	2.02E+07	1.40E+07
	Calculation	5.83E+07	2.59E+07	1.46E+07	9.33E+06	6.48E+06
	Deviation	53.93%	53.71%	53.75%	53.87%	53.81%
8.38175E-07	Simulation	1.24E+09	5.52E+08	3.12E+08	2.01E+08	1.39E+08
	Calculation	5.83E+08	2.59E+08	1.46E+08	9.33E+07	6.48E+07
	Deviation	52.89%	53.01%	53.23%	53.45%	53.48%
1.67635E-06	Simulation	2.42E+09	1.09E+09	6.16E+08	3.97E+08	2.76E+08
	Calculation	1.17E+09	5.18E+08	2.92E+08	1.87E+08	1.30E+08
	Deviation	51.88%	52.30%	52.68%	53.00%	53.11%
8.38175E-06	Simulation	1.11E+10	5.01E+09	2.88E+09	1.87E+09	1.31E+09
	Calculation	5.83E+09	2.59E+09	1.46E+09	9.33E+08	6.48E+08
	Deviation	47.31%	48.30%	49.30%	50.12%	50.60%
1.67635E-05	Simulation	2.24E+10	9.70E+09	5.51E+09	3.58E+09	2.52E+09
	Calculation	1.17E+10	5.18E+09	2.92E+09	1.87E+09	1.30E+09
	Deviation	47.81%	46.53%	47.08%	47.88%	48.46%
4.19088E-05	Simulation	6.45E+10	2.86E+10	1.45E+10	8.89E+09	6.08E+09
	Calculation	2.92E+10	1.30E+10	7.29E+09	4.67E+09	3.24E+09
	Deviation	54.81%	54.66%	49.58%	47.49%	46.72%

**Table F.1.** Thermal gradient ( $^{\circ}\text{C}/\text{m}$ ) comparison between multiphysics simulation and the presented equation. The average of deviations is about 50%.

## G. Optical cross-section of plasmonic nanostructure

As a representative example, we compare nanorod optical cross-sections under a resonant and non-resonant excitation. In case of resonant optical excitation, a large amount of Poynting vectors in space head toward the nanorod due to harmonic oscillation of free electron in metal, thus resulting in a larger optical cross-section than geometry cross-section. Whereas, nonresonant case shows that the optical cross-section is smaller than nanorod geometry section area.

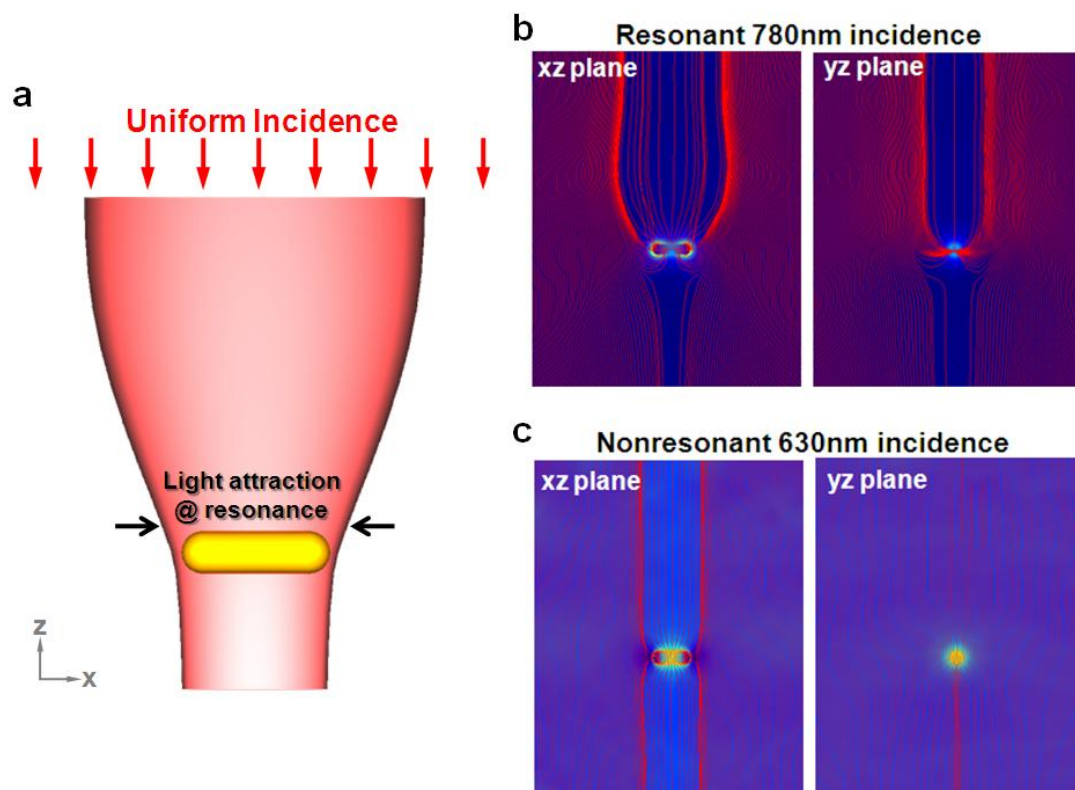


**Fig. G.1.** Optical cross-section comparison between the resonated and non-resonated nanorod.